Characterization of Multiple Moving Membrane Capacitive Micromachined Ultrasonic Transducer

by

Md. Iftekharul Islam

A Thesis submitted to the Faculty of Graduate Studies of

The University of Manitoba

in partial fulfilment of the requirements of the degree of

MASTER OF SCIENCE

Department of Electrical and Computer Engineering

University of Manitoba

Winnipeg

Copyright © 2019 by Md. Iftekharul Islam

Abstract

A newly developed multiple moving membrane capacitive micromachined ultrasonic transducer (M^3-CMUT) is fabricated and characterized in this thesis. Unlike the single vibrating membrane in the conventional capacitive micromachined ultrasonic transducer (CMUT), the novel design involves two deflectable membranes suspended over a fixed bottom electrode. In the presence of bias, both of the membranes deflect simultaneously, which results in a smaller cavity compared to a CMUT.

To understand the basics of a capacitive transducer, an equivalent mass-spring-capacitor model of CMUT was reported. The results of this analytical model were used to develop the finite element models (FEM) of CMUT and more complex M^3-CMUT in COMSOL Multiphysics software. The electromechanical analysis of these models was conducted to observe their operating conditions. Following the modeling and analysis, several single-cell, 1-D, and 2-D arrays of these devices were fabricated using PolyMUMPs technology, a sacrificial fabrication technique for the MEMS transducers.

The electrical and acoustic characterizations of the fabricated devices were performed to measure the actual transducer properties. The measured data and the model results were found to be in good agreement. It was observed from the electrical impedance measurements that a higher membrane deflection was achieved in the double membrane device. The reduction in the cavity of M^3-CMUT enhanced the sensitivity of the transducer. The acoustic characterization using a pitch-catch experimental setup demonstrated that the novel M^3-CMUT could be used as an ultrasonic transducer. The velocity and attenuation of the acoustic waves, when the transducer used as both the transmitter and the receiver, were found to be very close to the theoretical value.

Acknowledgements

I offer sincere gratitude to my advisor, Dr. Douglas Buchanan, for giving me the opportunity to do research in my area of interest. His valuable guidance, unwavering patience, and constant support have made it possible to complete my graduate study. I am grateful to my co-advisor, Dr. Arezoo Emadi, for her instantaneous response to all of my queries. Her advice and suggestion in all aspects of my research is a matter of tremendous assistance and endurance.

Special thanks go to Dr. Derek Oliver and Dr. Jason Morrison, for agreeing to be in the examining committee and reading my thesis. Their contribution to the betterment of the thesis is highly appreciated.

I acknowledge and thank Daryl Hamelin, Zoran Trajkoski, and Sinisa Janjic for their technical help and support. A wholehearted thank goes to graduate student advisor, Amy Dario, for her support from the beginning to the end of my academic journey at this university. I also acknowledge the support and feedback from my friends, Vaibhav Dubey, Mayank Thacker, Robin Raju, and Dliruba Zaman Jeba.

Thanks to CMC microsystems Canada for providing COMSOL Multiphysics simulation software. Special appreciation goes to MEMSCAP, Inc. fabrication facility.

I am indebted to my wife, Sanjida Jahan, for her incredible patience, love, and mental support through my ups and downs. I want to express my gratitude to my parents and elder brother for their unconditional love, care, and encouragement to dream big. Without the sacrifice of each and every member of my family, this achievement would not have been possible.

Finally, I am thankful to Almighty Allah for all of his blessings.

Dedication

To My Parents, Brother, and Beloved Wife

Table of Contents

Abstract ii

Acknowledgements iii

Dedication iv

Table of Contents v

List of Tables ix

List of Figures x

Chapter 1 Introduction 1

1.1 Background and Motivation 1

1.2 Thesis Outline 3

Chapter 2 Fundamentals of the CMUT & M^3-CMUT 5

2.1 Ultrasound Waves 5

2.1.1 Acoustic Impedance 5

2.1.2 Reflection and Transmission 6

2.1.3 Attenuation 7

2.2 Actuation of an Ultrasonic Transducer 8

2.3 Micromachined Ultrasonic Transducer 9

2.3.1 Piezoelectric Micromachined Ultrasonic Transducer 9

2.4 Capacitive Micromachined Ultrasonic Transducer 11

2.4.1 Multiple Moving membrane-CMUT (M^3-CMUT) 12

2.4.2 Geometry and Configuration of the CMUT 14

2.4.3 Fabrication of the CMUT 16

Chapter 3 Analytical Model of the CMUT 21

3.1 Mass-Spring-Capacitor Model 21

3.2 Static Analysis of the Analytical Model......25

3.2.1 Collapse Voltage 25

3.2.2 Spring Softening Effect......28

3.2.3 Resonant Frequency 31

3.3 Dynamic Analysis of the Analytical Model......33

3.3.1 Transformation Ratio 34

Chapter 4 Finite Element Model of the CMUT & M^3-CMUT 37

4.1 Design Consideration from the FEM 37

4.2 Static Analysis of the FEM 41

4.2.1 Stationary Study from COMSOL......41

4.2.1.1 Collapse Voltage Comparison 43

4.2.1.2 Membrane Displacement Comparison......43

4.2.2 Eigen Frequency Study from COMSOL......44

4.2.2.1 Resonant Frequency Comparison 44

4.2.2.2 Spring Softening Effect Comparison......46

4.3 Dynamic Analysis of the FEM......47

4.3.1 Frequency Domain Perturbation Study from COMSOL 47

4.3.2 Time Dependent Study from COMSOL......49

Chapter 5 Design and Fabrication of the CMUT & M^3-CMUT 51
5.1 Design Consideration 51
5.1.1 Chip Layout 53
5.2 Fabrication Method 55
5.2.1 PolyMUMPs Process 55
5.3 Fabrication Process Flow 58
Chapter 6 Electrical Characterization of the CMUT & M^3-CMUT 63
6.1 Electrical Characterization Apparatus 63
6.2 Collapse Voltage Measurement 65
6.3 Electrical Impedance Measurement 67
6.3.1 Resonant Frequency Comparison 70
6.3.2 Spring Softening Effect Comparison 71
6.3.3 Real Part Impedance Comparison 74
Chapter 7 Acoustic Characterization of the CMUT & M^3-CMUT 77
7.1 Pitch-Catch Apparatus 77
7.2 Acoustic Measurement 81
7.2.1 Wave Attenuation 81
7.2.1.1 Attenuation Coefficient 83
7.2.2 The Velocity of Acoustic Waves 85
7.3 DC Bias and Frequency Dependence of the Acoustic Waves 86
7.3.1 DC Bias Dependence of the Acoustic Waves 86

7.3.2 Frequency Dependence of the Acoustic Waves..88

Chapter 8 Conclusion..89

8.1 Summary 89

8.2 Future Work...91

References 92

List of Tables

Table 3.1. Parameters used for the theoretical calculation of the collapse voltage and the effective spring constant. 31

Table 4.1. Design parameters of the 3-D FEMs of CMUT and M^3-CMUT. 40

Table 4.2. Properties of the materials used in the 3-D FEMs of CMUT and M^3-CMUT.40

Table 4.3. First six eigenfrequencies of 65 μm radius CMUT and M^3-CMUT at 25 V DC bias. 45

Table 5.1. Dimensions of the CMUT and M^3-CMUT cell used in the L-Edit layout. 53

Table 5.2. Layer name, material, thickness, and lithography level name of the PolyMUMPs process [60]. 57

Table 5.3. Purpose of the lithography (mask) level [60]. 57

Table 6.1. Calculated, simulated, and measured resonant frequency comparison of the single-cell, 1-D and 2-D CMUT and M^3-CMUT devices at 25 V DC bias. 70

Table 6.2. Calculated and measured resonant frequency shift comparison for single-cell, 1-D, and 2-D devices. 73

Table 7.1. Parameters used for the theoretical value of attenuation coefficient [63]....84

List of Figures

Figure 2.1. Representation of acoustic impedance using Ohm's law……………………….6

Figure 2.2. Reflection and transmission of a planar wave. ……………………………………6

Figure 2.3. Cross-sectional schematic view of a basic PMUT cell……………………………9

Figure 2.4. PMUT operation in (a) transmitting and (b) receiving mode…………………10

Figure 2.5. (a) Cross-sectional schematic view of a basic CMUT cell and (b) equivalent parallel plate capacitor model of the CMUT……………………………………………………11

Figure 2.6. CMUT operation in (a) transmitting and (b) receiving mode. …………………12

Figure 2.8. M^3-CMUT operation in (a) transmitting and (b) receiving mode. ……………13

Figure 2.7. Cross-sectional schematic view of a basic M^3-CMUT cell. ……………………13

Figure 2.9. Various cell-geometry of CMUT: (a) Circular, (b) Axial, (c) Annular, and (d) Ring……………………………………………………………………………………………14

Figure 2.10. Different array configuration of CMUT: (a) 1-D, (b) 1.5-D, and (c) 2-D.…15

Figure 2.11. Types of 1-D CMUT array: (a) Linear, (b) Phased, and (c) Curvilinear. ….15

Figure 2.12. A typical surface micromachining process of capacitive transducer. ……16

Figure 2.13. Cavities with (a) slanted sidewalls during plasma etching and (b) vertical sidewalls with protective films during RIE etching……………………………………………18

Figure 2.14. A typical lift-off process of the top metal layer…………………………………19

Figure 3.1: First order mass-spring-capacitor model of CMUT. ……………………………22

Figure 3.2. Normalized electrostatic and spring restoring force as a function of the normalized membrane displacement. 26

Figure 3.3. The effective spring constant of a vibrating membrane as a function of applied bias for a given membrane (r = 65 μm radius) CMUT with a given thickness (h = 1.5 μm) and gap height (do = 0.75 μm)..30

Figure 3.4. The resonant frequency shift of a vibrating membrane as a function of applied bias for a given CMUT with a membrane, r = 65 μm, a thickness, h = 1.5 μm and a gap height, do = 0.75 μm. 32

Figure 3.5. Equivalent electrical circuit model of CMUT. 34

Figure 4.1. Effective Membrane diameter of (a) CMUT and (b) M^3-CMUT. 38

Figure 4.2. 2-D cross-sectional view of the FEMs of (a) CMUT and (b) M^3-CMUT........39

Figure 4.3. Static displacement of 65 μm radius (a) CMUT and (b) M^3-CMUT at a given DC bias (100 V) applied to the membrane and the grounded bottom electrode............42

Figure 4.4. Membrane displacement of 65 μm radius CMUT and M^3-CMUT at a given DC bias ranging from 0 V to 100 V..43

Figure 4.5. First six modes of vibration of 65 μm radius CMUT (a), (b), (c), (d), (e), and (f) and M^3-CMUT (g), (h), (i), (j), (k), and (l) at a given DC bias (25 V)..............................45

Figure 4.6. Frequency shift due to the spring softening effect of 65 μm radius CMUT and M^3-CMUT at a given DC bias ranging from 5 V to 50 V...47

Figure 4.7. Peak membrane displacement and resonant frequency dependence for a 65 μm radius CMUT and M^3-CMUT. The models were biased at 25 V DC superimposed with a 50 mV ac bias. 48

Figure 4.8. Driven response of the 65 μm radius membrane of CMUT, biased at 25 V DC superimposed by a 1 MHz, 50 mV ac bias. 49

Figure 4.9. Driven response of the 65 μm radius top membrane of M^3-CMUT, 25 V DC bias superimposed by a 1 MHz, 50 mV ac bias. 50

Figure 5.1. Top view of (a) M^3-CMUT and (b) CMUT cell and 3-D cross-sections of (c) M^3-CMUT and (d) CMUT cell..52

Figure 5.2. Full L-Edit layout of the chip extracted from the MEMS Pro software.......54

Figure 5.3. PolyMUMPs process (a) before and (b) after the sacrificial layer release [60]. 56

Figure 5.4. Cross-sectional view of the simplified fabrication process of CMUT; deposition and structuring of (a) Nitride, (b) Poly 0, (c) First Oxide, (d) Poly 1, (e) Second Oxide, (f) Poly 2, and (g) Metal layer. Layer heights and radii are not to scale. 59

Figure 5.5. Cross-sectional view of the fabrication process of M^3-CMUT; deposition and structuring of (a) Nitride, (b) Poly 0, (c) First Oxide, (d) Poly 1, (e) Second Oxide, (f) Poly 2, and (g) Metal layers. Layer heights and radii are not to scale. 60

Figure 5.6. Top view of a (a) non-bonded and a (b) bonded chip. The non-bonded chip was enlarged using a scope...62

Figure 6.2. Bonded chip in a 68 pin ceramic carrier placed in the test fixture. 64

Figure 6.1. The interior of the probe station, (b) the non-bonded chips and the tungsten probes, and (c) two probes contact the membrane and bottom plate connections. 64

Figure 6.3. Schematic diagram of the electrical measurement apparatus. 65

Figure 6.4. Collapse voltage measurement using a 2-D M^3-CMUT device..................66

Figure 6.5. (a) Real and (b) imaginary part impedance curve of the 65 μm radius 2-D CMUT and M3-CMUT device at 25 V DC bias superimposed by a 50 mV ac bias. 67

Figure 6.6. Equivalent (RLC) circuit model of the electrical measurement setup of the transducer. 68

Figure 6.7. Baseline subtracted real part impedance curve of 65 μm radius 2-D (a) CMUT and (b) M^3-CMUT device ranging from 0 V to 25 V DC bias superimposed by a 50 mV ac bias. 69

Figure 6.8. Frequency shift due to the spring softening effect of the single-cell CMUT and M^3-CMUT (65 μm radius) at a DC bias range of 16 V to 25 V. The DC bias was superimposed by a 50 mV ac bias. 72

Figure 6.9. Spring softening effect in (a) 1-D and (b) 2-D array devices of CMUT and M^3-CMUT (65 μm radius) ranging from 6 V to 25 V DC bias superimposed by a 50 mV ac bias. 73

Figure 6.10. Relative change in the real part impedance of 65 μm radius CMUT and M^3-CMUT at a DC bias range of 16 V to 25 V. The DC bias was superimposed by a 50 mV ac bias. 74

Figure 6.11. Relative change in the real part impedance of (a) 1-D and (b) 2-D array device of CMUT and M^3-CMUT (65 μm radius) from 6 V to 25 V DC bias superimposed by a 50 mV ac bias. 75

Figure 7.1. Experimental setup of the pitch-catch apparatus. 78

Figure 7.2. Schematic connection diagram of the CAP5 transducer in the (a) transmitting and the (b) receiving mode. 79

Figure 7.3. Schematic connection diagram of the CMUT and M^3-CMUT transducer in the (a) transmitting and the (b) receiving mode. 80

Figure 7.4. Attenuation of the transmitted signals from the CAP5 transducer in air medium; received by the (a) CMUT and (b) M^3-CMUT transducer at distances of ~1 cm and ~1.6 cm. 82

Figure 7.5. Attenuation coefficient measurement in air medium when the CMUT/M^3-CMUT was used as the (a) transmitter and the (b) receiver at a distance of ~1 cm from the CAP5 transducer. 83

Figure 7.6. Acoustic wave velocity measurement of the transmitted signals from the (a) CMUT and (b) M^3-CMUT; received by the CAP5 transducer at a distance of ~1 cm. 85

Figure 7.7. DC bias dependence of CMUTs and M^3-CMUTs at the (a) transmitter and the (b) receiver side at a distance of ~1 cm. 87

Figure 7.8. Frequency dependence of CMUTs and M^3-CMUTs at a distance of ~1 cm..88

Chapter 1 Introduction

1.1 Background and Motivation

Ultrasonic transducers convert electrical signals to ultrasound waves, and vice-versa. An ultrasonic transducer system is used to evaluate an object by interpreting the transmitted and reflected signals. The evaluation is usually performed by transmitting a pulse and receiving an echo, which reflects from the surface of the object. Firestone's patent relating to flaw detection in metals in 1942 [1] was the first modern pulse-echo technique, paving the way of detection and ranging using ultrasound. The ultrasonic transducer is generally used in imaging applications, most often in medical sectors [2]. Also, the distinctive characteristic of penetrating almost any object without causing much harm makes ultrasound a feasible candidate for non-destructive testing (NDT) [3].

The traditional ultrasonic transducers are mostly piezoelectric. In 1880, the Curie brothers, Jacques and Pierre, discovered the piezoelectricity on some crystals. They observed that the crystals go through physical expansion and compression and produce an electric voltage when pressure is applied [4]. Since then, various crystals, polymers, ceramics, and composites have been studied for efficient piezoelectric materials. Typical single crystals (e.g., quartz, tourmaline, Rochelle salt) were used in the 1930s and 1940s to form the piezoelectric transducers [5]. Compared to the single crystals, piezoelectric ceramics have exhibited improved piezoelectric effect. Barium titanate ($BaTiO_3$) was the first ceramic material used in an ultrasonic transducer in 1947 [6]. Another ceramic, lead zirconate titanate (PZT), was introduced in 1957, which offered better piezoelectric coupling and a broader range of operating temperature [6].

Piezoelectric materials for micromachined transducers have also been investigated. Developments have been made in piezoelectric micromachined ultrasonic transducers (PMUTs) by improving their bandwidth and coupling efficiency [7]. However, the effectiveness of piezo-based micromachined transducers has been compromised by several drawbacks such as the impedance mismatch with the surrounding mediums, bad noise performance, and membrane displacement limitation [8]. The impedance mismatch occurs due to the acoustic impedance difference of the mediums. For example, the typical acoustic impedance of piezoelectric material ($\sim 30 \times 10^6\ \mathrm{kg.m^{-2}.s^{-1}}$) is much higher than air ($\sim 400\ \mathrm{kg.m^{-2}.s^{-1}}$) and water ($\sim 1.483 \times 10^6\ \mathrm{kg.m^{-2}.s^{-1}}$) [9], [10].

The capacitive ultrasonic transducer has been considered as a potential candidate to replace the piezoelectric transducer. The first capacitive ultrasonic transducer was demonstrated in the air in 1954 [11] and in immersion in 1979 [12]. Micro-electro-mechanical system (MEMS)-based capacitive ultrasonic transducers were introduced in the late 1980s [13], [14]. With the progression of microfabrication techniques, an improved version of the capacitive transducer was developed by M. Haller and B.T. Khuri-Yakub in 1993 [8]. The new capacitive micromachined ultrasonic transducer (CMUT) displayed a broader bandwidth, a higher sensitivity, and a lower temperature dependency [15] than its piezo counterpart.

The recent CMUTs used in medical imaging and NDT applications have showed enhanced electro-acoustic coupling and imaging performances. Using a thin circular plate as a membrane, the CMUT produces a low mechanical impedance which reduces the impedance mismatch with the adjacent medium [16]. The vibrating membrane can be optimized to match the impedance of the propagating medium as well, thus improving imaging quality [17].

Efforts have been made to improve the capacitive performances of CMUT. These improvements include enhancements on the detection properties [18], electrical safety [19], and the effective capacitance of the transducers [20]. To improve the capacitive properties even further, T. A. Emadi and D. A. Buchanan patented a novel CMUT design based on two circular plates, both acting as a membrane [21]. The new design is termed as multiple moving membrane-CMUT or M^3-CMUT.

The motivation behind this thesis is to compare the electrical and acoustic properties of the new M^3-CMUT transducer with respect to a conventional CMUT. The process starts with describing the operation principles of these transducers using analytical and finite element models, which lead to their design and fabrication. The characterization is then followed with a demonstration of the actual properties of the fabricated transducers.

1.2 Thesis Outline

The thesis is organized in eight chapters as described below.

The background and motivation of the thesis are given in Chapter 1. The outline of the thesis is stated as well.

In Chapter 2, the basics of capacitive transducers are presented. This includes several common properties of the ultrasound wave, the simple structures, and the working principles of the ultrasonic transducers, such as PMUT, CMUT, and M^3-CMUT. A common geometry and its method of fabrication of capacitive transducers are also presented.

An analytical model of the CMUT is presented in chapter 3. The static and dynamic analyses of the model are carried out. The theoretical explanations of the

fundamental transducer properties, such as collapse voltage, spring softening effect, and resonant frequency, are given.

Finite Element Models (FEMs) of the CMUT and M^3-CMUT are described in Chapter 4. The static and dynamic simulations conducted in COMSOL Multiphysics software are described to provide comparisons between the CMUT and M^3-CMUT based on sensitivity, membrane displacement, and driving voltage.

The design parameters and physical layout of the chip are provided in Chapter 5. The PolyMUMPs process, used to fabricate the devices, is described step-by-step in this chapter.

In Chapter 6, the electrical characterization of the fabricated devices (single-cell, 1-D array, and 2-D array) is reported. The properties of electrical impedance are analyzed and compared between the two designs.

The acoustic characterization of the 2-D devices is described in Chapter 7. The transmit and receive capability of the transducers are investigated. An air-coupled 'Pitch-Catch' experimental setup that was built for the characterization is presented.

The thesis is concluded with a summary and a description of future work in Chapter 8.

Chapter 2 Fundamentals of the CMUT & M^3-CMUT

In this chapter, the fundamentals of CMUT and M^3-CMUT are presented, starting with some typical properties of an ultrasound wave. The basic structural and operational differences between various micromachined ultrasonic transducers are then described. Some relevant geometries and fabrication methods of the capacitive transducers are also introduced before going into the details of the modeling and fabrication of these MEMS transducers.

2.1 Ultrasound Waves

Ultrasound is an acoustic wave with frequencies higher than the audible limit of human hearing. The upper-frequency limit varies from person to person but is typically found to be around 20 kHz. As a type of wave, ultrasound follows the usual wave propagation equation which can be expressed by [22]

$$\lambda = {}^{v}/_{f} \qquad 2.1$$

where λ is the wavelength, f is the frequency, and v is the velocity of the acoustic wave in a specific medium.

Unlike electromagnetic waves, ultrasound cannot propagate without a physical medium. So, there exists a strong correlation between the wave properties (i.e., attenuation, reflection, transmission, the speed of propagation, etc.) and the features of the specific medium (i.e., acoustic impedance, density, elasticity, etc.).

2.1.1 Acoustic Impedance

The acoustic impedance can be defined by an analogy to the electrical impedance using Ohm's law, as shown in Figure 2.1, which is the ratio of pressure produced by an

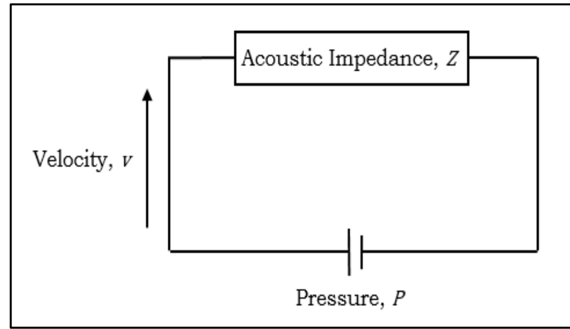

Figure 2.1. Representation of acoustic impedance using Ohm's law.

acoustic wave to the velocity of the wave in a medium [23]. For a planar wave, the acoustic impedance is therefore given by

$$Z = \frac{P}{v} \tag{2.2}$$

where P is the pressure and v is the velocity of the acoustic wave.

2.1.2 Reflection and Transmission

In Figure 2.2, a schematic diagram of an acoustic wave propagating from one medium (acoustic impedance of $Z1$) to another (acoustic impedance of $Z2$) is shown. For

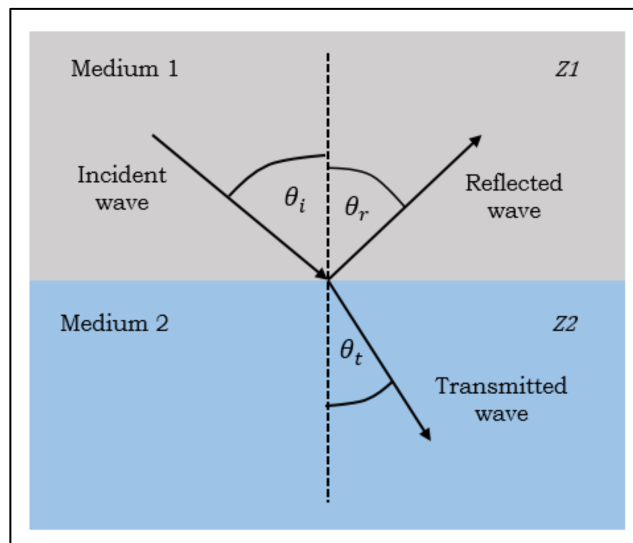

Figure 2.2. Reflection and transmission of a planar wave.

a planar wave, the relationship between the acoustic impedance of the two mediums and their angle of incidence and transmission can be given by the amplitudes of transmission coefficient (T) and reflection coefficient (R) as in Equations 2.3 and 2.4, respectively [23],

$$T = \frac{P_t}{P_i} = \left|\frac{2Z_2\cos\theta_i}{Z_2\cos\theta_i + Z_1\cos\theta_t}\right| \quad 2.3$$

$$R = \frac{P_r}{P_i} = \left|\frac{Z_2\cos\theta_i - Z_1\cos\theta_t}{Z_2\cos\theta_i + Z_1\cos\theta_t}\right| \quad 2.4$$

where P_i , P_r and P_t are the pressures generated by the incident, reflected and transmitted waves, respectively, and the angle of incidence is θ_i and transmission is θ_t.

For a wave perpendicular to the interface between the mediums ($\theta_i = \theta_t = 0$), Equations 2.3 and 2.4 become

$$T = \left|\frac{2Z_2}{Z_2 + Z_1}\right| \quad 2.5$$

$$R = \left|\frac{Z_2 - Z_1}{Z_2 + Z_1}\right| \quad 2.6$$

2.1.3 Attenuation

Attenuation is the reduction of signal amplitude, which exponentially decays as a function of the distance traveled. The decay is due to the absorption of wave energy by the travel medium. The decay of signal amplitude can be approximated by [24]

$$I = I_0 e^{-2\alpha x} \quad 2.7$$

where x is the propagation distance, I is the signal amplitude at distance x, I_0 is the signal amplitude at the reference point ($x = 0$), and α is the attenuation coefficient.

The attenuation coefficient (α) in a particular medium can be given by using Stoke's law such that [25]

$$\alpha = \frac{2\eta\omega^2}{3\rho v^3} \qquad 2.8$$

where η is the dynamic viscosity of the medium, $\omega = 2\pi f$ is the angular frequency, ρ is the density of the medium, and v is the velocity of the wave in the medium.

Typically the attenuation coefficient is expressed in Nepers per meter ($Np.m^{-1}$) or decibels per meter ($dB.m^{-1}$). The relationship between these units is given in Equations 2.9 and 2.10 below [24].

$$Np = \ln\frac{I_2}{I_1} = \frac{\log_{10}\left(\frac{I_2}{I_1}\right)}{\log_{10}(e)} = \frac{1}{20\log_{10}(e)} \times 20\log_{10}\left(\frac{I_2}{I_1}\right) = 0.115\ dB \qquad 2.9$$

$$1\ dB = 8.69\ Np \qquad 2.10$$

where I_1 and I_2 are the signal amplitudes at two different points.

2.2 Actuation of an Ultrasonic Transducer

Actuation of a microsystem involves the mechanism to produce ultrasound waves. Electrostatic, electromagnetic, piezoelectric, magnetostriction, and thermal are some of the actuation techniques of ultrasonic transducers [26]. Electrostatic actuation is defined as the generation of the electrical force of attraction or repulsion induced by an electric field. Electromagnetic actuation refers to the production of Lorentz force and torque using a magnetic field from an electrical input (current). The piezoelectric effect is the generation of electrical voltage in response to the deformation of piezoelectric material (i.e., quartz). The reverse is also valid; that is, the material deforms with the

application of an electrical voltage. Magnetostriction is a property of ferromagnetic materials (e.g., cobalt, iron, ferric oxide, etc.) where they change physical form in the presence of a magnetic field. Thermal actuation depends on the thermal expansion (change of shape, area, and volume in response to a change in temperature) of two materials that are bonded together. Among these techniques, electromagnetic, magnetostriction and thermal are extensively used in macroscale sensors and devices whereas piezoelectric and electrostatic are more common in miniaturized microscale MEMS applications.

2.3 Micromachined Ultrasonic Transducer

With the advancement of silicon micromachining technology, new possibilities have emerged in the form of micromachined ultrasonic transducer (MUT) technology. For example, a vibrating membrane is coupled with a layer of piezoelectric material for the fabrication of a PMUT. On the other hand, in the case of CMUT, the membrane is coupled with a fixed layer with an air gap in between whereas the aforementioned M^3-CMUT design has multiple vibrating membranes.

2.3.1 Piezoelectric Micromachined Ultrasonic Transducer

A piezoelectric transducer usually consists of three layers: an impedance matching layer in the front, a piezoelectric material layer in the middle, and a backing

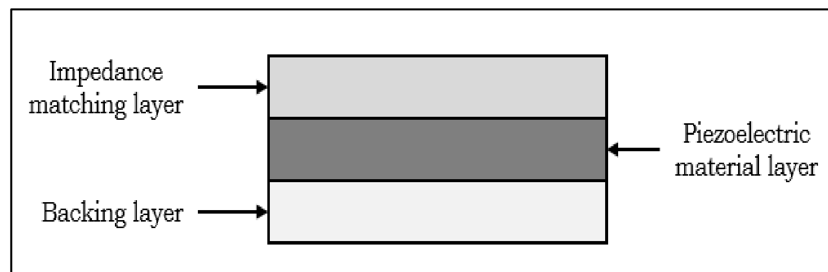

Figure 2.3. Cross-sectional schematic view of a basic PMUT cell.

layer in the back [27], as demonstrated in Figure 2.3. The impedance matching layer is used to maximize the efficiency of energy transfer into and out of the piezoelectric layer. This layer is required to reduce the impedance mismatch between the piezoelectric element and the outside medium. The function of the backing layer is to absorb energy directed to the back of the piezoelectric layer. A suitable material with proper acoustic impedance and attenuation coefficient (as mentioned in Sections 2.1.1 and 2.1.3) is used in this regard.

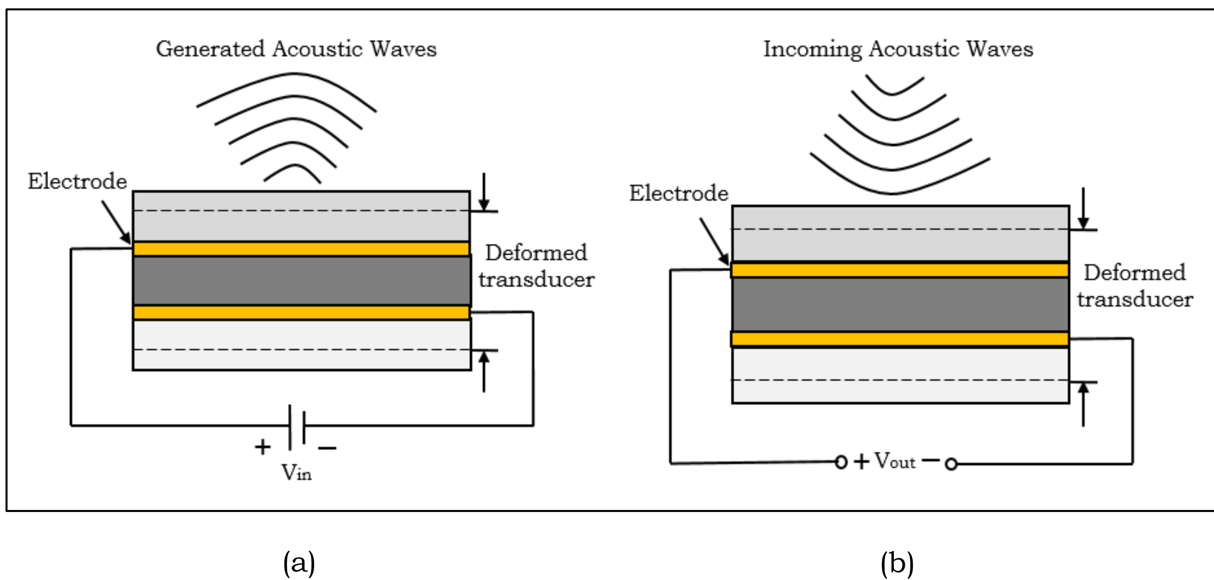

(a) (b)

Figure 2.4. PMUT operation in (a) transmitting and (b) receiving mode.

The basic operation of PMUT is based on the applied voltage-deformation duality [27], which is shown in Figure 2.4. In the transmitting mode, a voltage is applied across the piezoelectric layer, which causes the layer to deform and move back and forth. The stress that induced due to this movement generates acoustic waves into the neighboring medium, as shown in Figure 2.4 (a). For an incoming acoustic wave, a change in pressure occurs that induces a deformation of the piezo layer. The deformation generates a voltage across the piezoelectric layer. This is the receiving mode of the transducer, which is presented in Figure 2.4 (b).

2.4 Capacitive Micromachined Ultrasonic Transducer

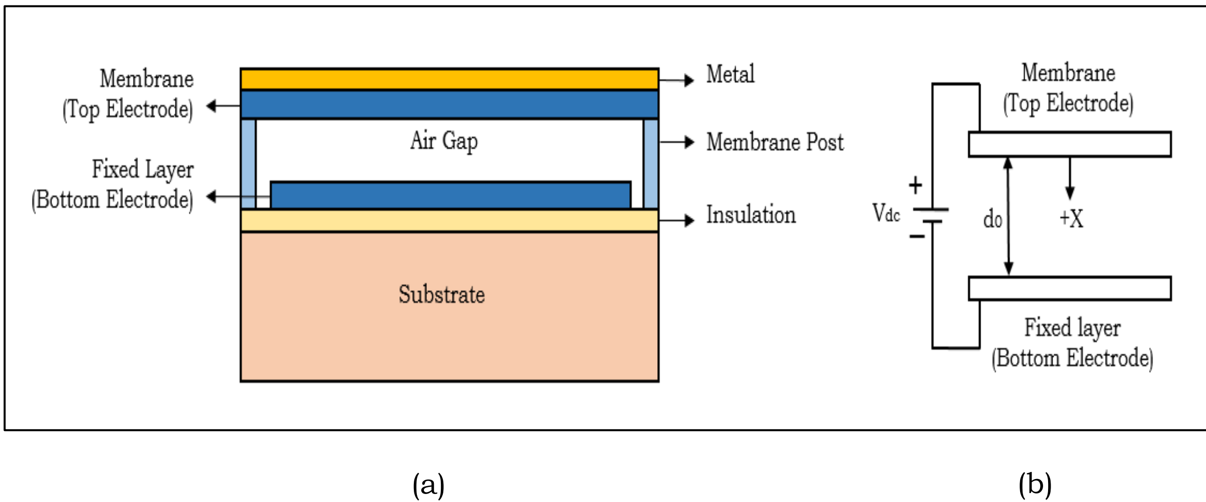

(a) (b)

Figure 2.5. (a) Cross-sectional schematic view of a basic CMUT cell and (b) equivalent parallel plate capacitor model of the CMUT.

A typical capacitive transducer consists of a thin membrane suspended over a thin fixed layer with an air gap in between. A cross-sectional schematic view of a CMUT cell is shown in Figure 2.5 (a). The structure can be viewed as a simple parallel plate capacitor [9] where the metalized membrane is the top electrode, and another conductive layer is the fixed bottom electrode as presented in Figure 2.5 (b). The outer edge of the membrane is connected with the fixed layer by one or more pillars (membrane post) depending upon the design configuration. An insulation layer is used to avoid shorting the top structure from the substrate.

The operating principle of a CMUT is based on the generation of an electrostatic force between the membrane (top electrode) and the fixed layer (bottom electrode). When a bias (ac and/or DC) is applied between the electrodes, an electrostatic force is generated between them. The force attracts the electrodes toward each other. However, since the bottom electrode is fixed, only the suspended membrane is displaced, causing a reduction of the air gap.

A DC bias is applied for the membrane displacement, and an additional ac bias is superimposed with the DC bias for the membrane vibration. Thus the membrane generates acoustic waves into the surrounding medium. This operation is the transmitting mode of the transducer, which is depicted in Figure 2.6 (a). In the receiving mode, a DC bias is applied to the membrane. The membrane experiences further mechanical displacement in the presence of incoming acoustic waves. The displacement enforces a capacitance change between the electrodes, which results in an ac signal. A high impedance amplifier circuit is used for the detection of the signal, as displayed in Figure 2.6 (b).

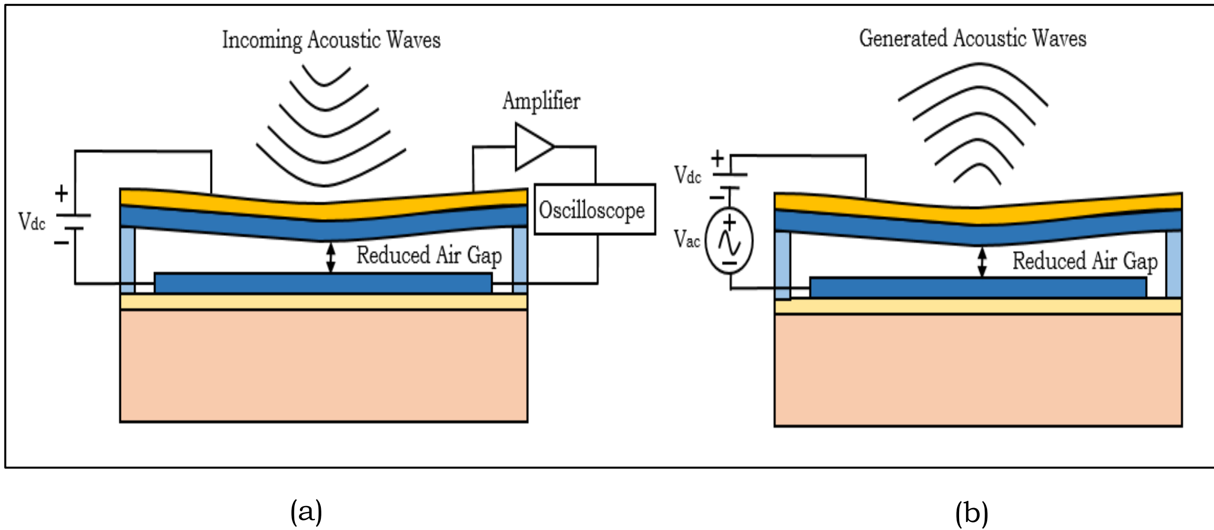

(a) (b)

Figure 2.6. CMUT operation in (a) transmitting and (b) receiving mode.

2.4.1 Multiple Moving membrane-CMUT (M^3-CMUT)

An M^3-CMUT cell has a similar structure to that of a conventional CMUT [28]. The fundamental structural difference is that M^3-CMUT has introduced an additional deflectable membrane in between the top membrane and the bottom electrode, as shown in Figure 2.7. In this device, the middle membrane acts as a moveable electrode along with the top membrane.

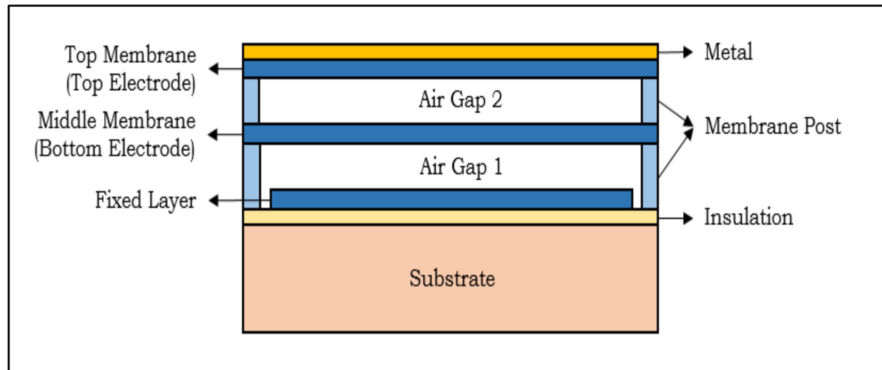

Figure 2.8. Cross-sectional schematic view of a basic M3-CMUT cell.

A schematic representation (similar to Figure 2.6 for the CMUT) of the transmission and reception of an M3-CMUT are illustrated in Figures 2.8 (a) and 2.8 (b), respectively. Since the M3-CMUT has two deflectable membranes, both will experience a displacement towards each other in the presence of bias [28].

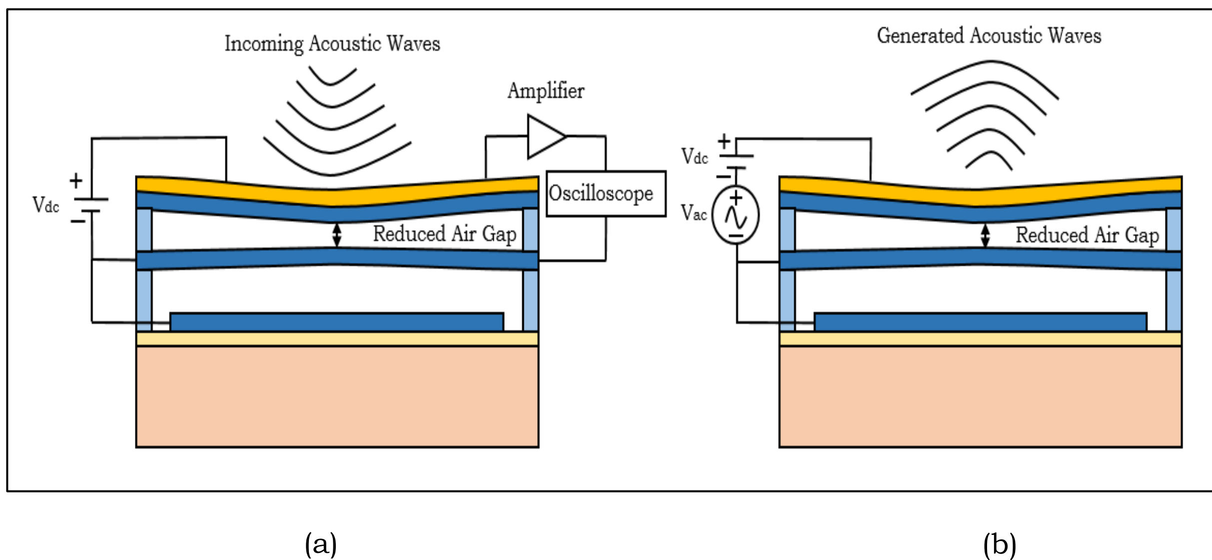

(a) (b)

Figure 2.7. M3-CMUT operation in (a) transmitting and (b) receiving mode.

2.4.2 Geometry and Configuration of the CMUT

The capacitive transducers can be divided into two main categories: single-element (single-cell) transducer and an array of transducers. Single-element transducers are mainly used in A-scan (amplitude scan) to detect echo sources along the center of the transducer [29]. They are mounted on 1-D and 2-D scanning stations to get their respective 1-D and 2-D images.

Single-element transducers can be made in many different geometries, including circular [30], rectangular [31], axial [32], annular [33], and ring [34] transducers. Some of these structures [35] are shown in Figure 2.9. The circular transducer is a superior design to that of the rectangular transducer because it offers a greater deflection and a lower induced stress in the membrane [36]. The axial and ring array transducers are generally used in catheter-based intravascular imaging since they allow a guidewire to pass through the center of the transducer [37]. Unlike the circular transducer, an annular transducer is capable of focusing along the depth direction [33].

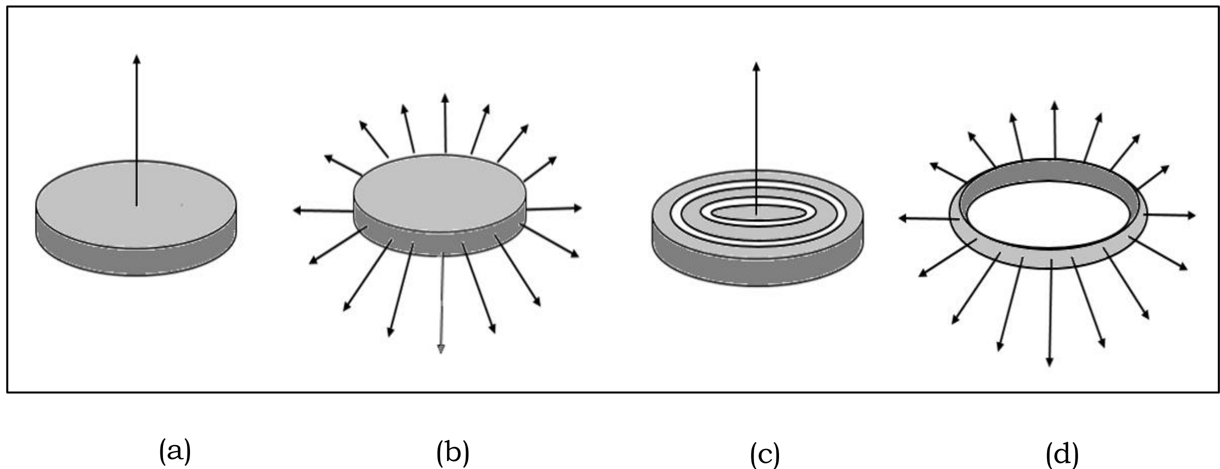

(a) (b) (c) (d)

Figure 2.9. Various cell-geometry of CMUT: (a) Circular, (b) Axial, (c) Annular, and (d) Ring.

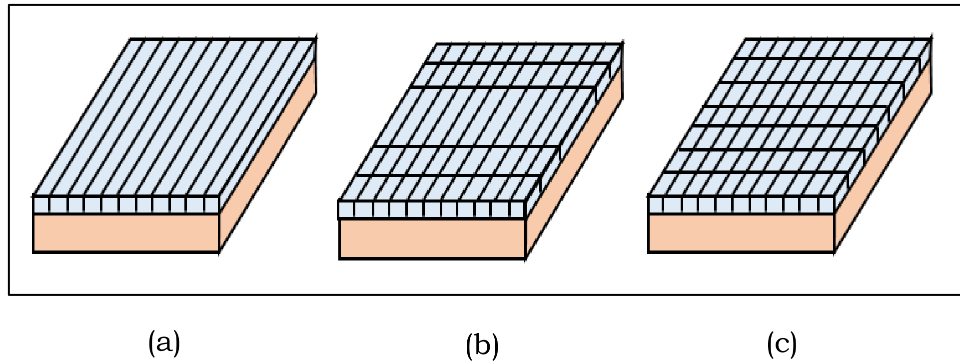

Figure 2.10. Different array configuration of CMUT: (a) 1-D, (b) 1.5-D, and (c) 2-D.

Single cells may be connected in different configurations [38] (see Figure 2.10) to form the 1-D, 1.5-D, and 2-D array transducers. Some common types of 1-D array transducer are linear arrays, phased arrays, and curvilinear arrays [35] shown in Figure 2.11. Linear array transducers have a field of view of constant width, as illustrated in Figure 2.11 (a), which is useful for imaging organs near the skin [39]. In contrast, with controlled steering of the field of view, as shown in Figure 2.11 (b), phased array transducers are ideal for cardiovascular imaging [40]. Curvilinear arrays are preferred for musculoskeletal imaging [41] because of their concave-shaped field of view, which is visible in Figure 2.11 (c).

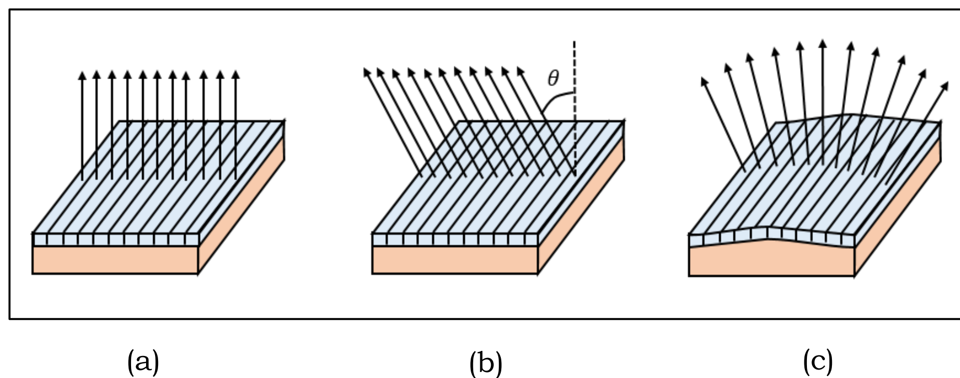

Figure 2.11. Types of 1-D CMUT array: (a) Linear, (b) Phased, and (c) Curvilinear.

In the 1.5-D array configuration, as depicted in Figure 2.10 (b), the transducer elements are divided into five sub-elements, which enables variable focusing [38]. On

the other hand, depending on the activation mechanism of the elements, a 2-D array (Figure 2.10 (c)) transducer can come into different forms including a sparse array [42] where a precise number of elements are periodically activated, a fully-addressed array [43] and a row-column addressed array [44].

2.4.3 Fabrication of the CMUT

Two of the most widely used techniques for the fabrication of capacitive transducers involve surface micromachining and wafer bonding. In a surface

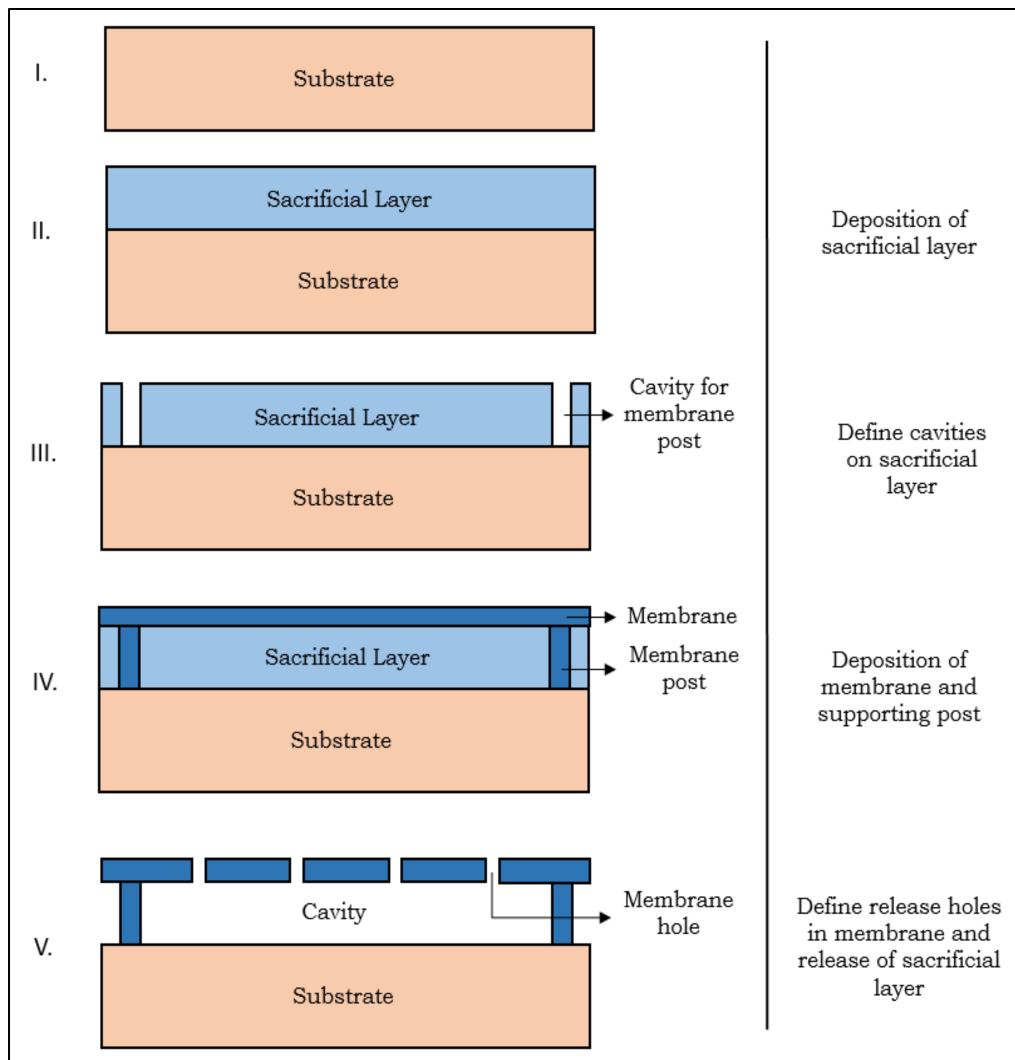

Figure 2.12. A typical surface micromachining process of capacitive transducer.

micromachining technique [8], [45], [28], a microstructure is built by adding material layers on top of the substrate. As shown in Figure 2.12, a typical process involves a structural layer (membrane) being deposited over a sacrificial layer. The sacrificial layer is used to create a cavity for the suspending membrane. The layer is later "released" (or removed) through the "holes" created in the membrane. Polycrystalline silicon (polysilicon) is a conventional membrane material. A sacrificial layer is usually made of phosphosilicate glass (50 - 70% of SiO_2), commonly known as PSG. Low-pressure chemical vapor deposition (LPCVD) is a conventional deposition technique of these material layers where an elevated temperature is used in a low-stressed pressure (i.e., 1 Torr) environment. In contrast to surface micromachining, the wafer bonding process, which was first reported by Huang et al. in 2003 [46], involves the bonding of two wafers to create a sealed cavity in between. Typically, single-crystal silicon (Si) [47] and silicon carbide (SiC) [48] are used as the bulk wafers.

Etching is the primary technology for patterning (releasing/structuring) material layers which involves exposure of the layer to an etchant. Different etchants are used for different materials. There are two major types of etchants: wet (liquid) and dry (plasma). Wet etchants may be acidic agents, such as hydrofluoric acid (HF), nitric acid (HNO_3), acetic acid (CH_3COOH), etc., or alkaline chemicals, such as potassium hydroxide (KOH), tetramethylammonium hydroxide (TMAH), etc. [49]. Stiction is a mechanical limitation associated with these wet etchants [50]. If a wet etchant is used for the release of a sacrificial layer, then the surface tension of the liquid may bring the membrane closer to the substrate and hold them together which is referred to as stiction. Care must be taken to limit stiction by removing the wet etchants properly after a sacrificial etch process.

Dry etchants are typically a plasma (an ionized gas carrying a large number of free electrons and positively charged ions) of materials such as chlorine (Cl_2), dichlorodifluoromethane (CCl_2F_2), carbon tetrachloride (CCl_4), boron trichloride (BCl_3), etc. [49]. The plasma gases have better etch rates than the liquid etchants, but they fail to create cavities with vertical sidewalls, as shown in Figure 2.13 (a). This is because the upper side of a layer is exposed to the etchants for more time. Reactive ion etching (RIE) can be used to overcome this problem, which produces protective thin films on the sidewalls (see Figure 2.13 (b)). These thin films are removed after the etching process. The RIE is typically employed to dig out sharp cavities in which the support of the structural layer is formed.

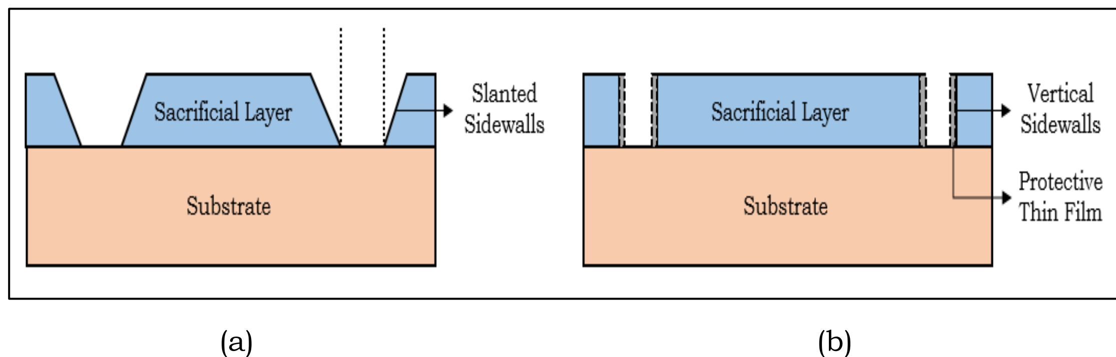

(a) (b)

Figure 2.13. Cavities with (a) slanted sidewalls during plasma etching and (b) vertical sidewalls with protective films during RIE etching.

As opposed to the subtractive etching technique stated above, lift-off is an additive patterning technique, which is often used to create metallic interconnections [49]. For a better electrical conductivity, a metal layer is added on the top of a membrane. The lift-off process is used to pattern such metal layers, as shown in Figure 2.14. In this technique, the sacrificial and masking layers are added (step II) to the

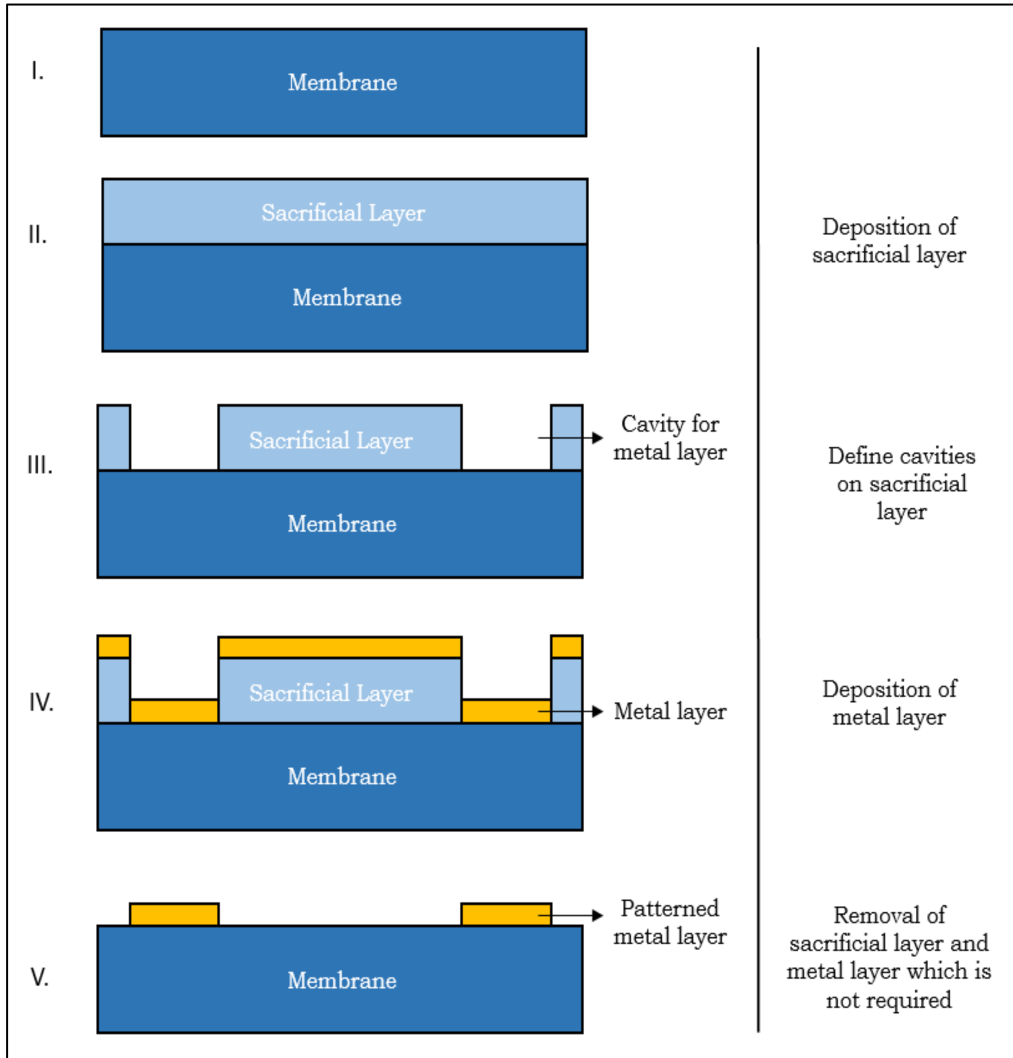

Figure 2.14. A typical lift-off process of the top metal layer.

surface of the membrane to be patterned (step III). The layers are then etched to define the cavities. The metal layer is then deposited on top of the patterned sacrificial layer (step IV). Finally, the sacrificial layer is removed to complete the structure (step V).

A masking layer is a protective layer, which is used to pattern a material layer. A photoresist, which is a light-sensitive organic material, is generally used as the protective mask. The method of patterning a material using photoresist is called photolithography, which involves exposing the resist layer to light through a patterned

mask. Photoresists can be either positive or negative. Positive photoresists become soluble after the exposure of light, whereas negative photoresists become insoluble. Thus one can produce positive and negative images of a given material. However, these resist masks may degrade rapidly with the use of a plasma etching, which is a more dynamic process and not very selective normally. A more durable mask, known as a "hard mask", can be used instead to make the etching process more selective [49]. Phosphosilicate glass (PSG) and silicon nitride (Si_3N_4) are the common hard mask materials.

Chapter 3 Analytical Model of the CMUT

To understand the working principle of a capacitive transducer, the physical and electronic properties of a single membrane CMUT has been investigated. An analytical model of CMUT describing various operating conditions of a capacitive transducer is presented in this chapter.

3.1 Mass-Spring-Capacitor Model

As discussed in Section 2.4, the membrane and electrode formation in a CMUT can be simplified as a parallel plate capacitor (see Figure 2.5 (b)) with an air gap between the two plates. The top plate is usually the movable membrane, whereas the bottom plate is the fixed electrode. With a bias voltage applied across the gap, an electrostatic force is induced, causing the top plate to move towards the fixed electrode. A restoring force, related to the membrane stiffness, resists the movement of the plate. This effect of an applied bias on the movable plate can be described by a lumped electro-mechanical model consisting of a mass m, a linear spring k, and a parallel plate capacitor C.

A schematic diagram of a mass-spring-capacitor model [9] is shown in Figure 3.1. In accordance with the "small deflection plate" theory [51], it is assumed that a linear relationship exists between the spring restoring force of the movable plate and its displacement. It is also considered that the membrane has a smoothly varying, continuous surface so that the displacement is uniform over the entire membrane. Moreover, the electrical fringing field and membrane curvatures are neglected since the diameters of plates are often much larger than the gap between them or the membrane displacement. For simplicity, it is assumed that CMUT is operating in a vacuum such that there is no loading effect due to the compression of the medium between the plates.

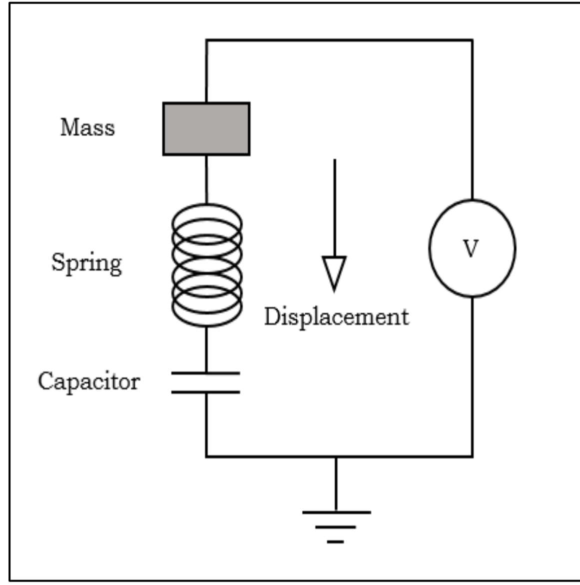

Figure 3.1: First order mass-spring-capacitor model of CMUT.

When a voltage is applied to the top plate with the bottom plate grounded, an electrostatic force is generated, which causes the top plate to move towards the fixed bottom plate. Once the top plate moves from its initial position, a mechanical restoring force (in the opposite direction) results from the elasticity or stiffness (Young's modulus) of the moving plate. The resultant electrostatic force, $F_{Electrostatic}$ and spring restoring force, F_{Spring} combines to yield a net force F_{Mass} on the plates which can be expressed by [9]

$$F_{Mass} = F_{Spring} + F_{Electrostatic} \qquad 3.11$$

The electrostatic force can be expressed as the derivative of the potential energy of the capacitor with respect to the position of the mass due to the displacement of the top plate [52],

$$F_{Electrostatic} = -\frac{d}{dx}\left(\frac{1}{2}CV^2\right) \qquad 3.12$$

where C is the capacitance between the parallel plates, V is the potential bias across the plates, and x is the displacement of the top plate under bias.

The capacitance of a parallel plate capacitor is given by,

$$C = \frac{\varepsilon A}{d} = \frac{\varepsilon A}{d_0 - x} \qquad 3.13$$

where ε is the dielectric permittivity of the material between the plates, A is the plate area, d is the gap between the plates, and d_0 is the initial gap between plates.

The dielectric permittivity of the material between the plates is given by,

$$\varepsilon = \varepsilon_0 \varepsilon_r \qquad 3.14$$

where ε_0 is the dielectric permittivity of free space and ε_r is the relative permittivity of the dielectric material.

For vacuum, $\varepsilon_r = 1$, Equation 3.4 can be reduced using $\varepsilon = \varepsilon_0$. The total capacitance from Equation 3.3 can now be expressed as

$$C = \frac{\varepsilon_0 A}{d_0 - x} \qquad 3.15$$

Substituting Equation 3.5 into Equation 3.2 yields,

$$F_{Electrostatic} = -\frac{1}{2} V^2 \left[\frac{d}{dx} \left(\frac{\varepsilon_0 A}{d_0 - x} \right) \right] = \frac{\varepsilon_0 A V^2}{2(d_0 - x)^2} \qquad 3.16$$

The mechanical spring force can be expressed using Hooke's law [53], which states that the spring force is linearly proportional to the displacement x as

$$F_{Spring} = -kx \qquad 3.17$$

where k is the spring constant (derived in Section 3.2.2) of the plate.

The gravitational mass force can be expressed using Newton's second law of motion given by

$$F_{mass} = m \frac{d^2x}{dt^2} \quad 3.18$$

where m is the mass of the plate and $a = \frac{d^2x}{dt^2}$ is the acceleration of the plate.

Substituting the expressions of F_{Mass} (3.8), F_{Spring} (3.7) and $F_{Electrostatic}$ (3.6) into Equation 3.1 yields a second-order differential equation of net force acting on the system given by

$$m \frac{d^2x(t)}{dt^2} - \frac{\varepsilon_0 AV(t)^2}{2(d_0 - x)^2} + kx(t) = 0 \quad 3.19$$

where the applied bias voltage is time-varying, $V(t) = V_{DC} + V_{ac}sin(\omega t)$, with V_{DC} as the DC voltage and V_{ac} as the time-varying ac voltage, to provide a time-dependent behavior of the system.

The mass-spring-capacitor model given by Equation 3.9 above is used to describe the static and the dynamic operation of CMUT in the following sections.

3.2 Static Analysis of the Analytical Model

The time-independent static analysis can give insight to several of the design structuring parameters that include the collapse voltage, the spring softening effect, and the resonant frequency of the CMUT device. The applied bias should be less than the "collapse voltage" to avoid damaging the device. The "spring softening effect" is derived from the shift in the resonant frequency as a function of the applied DC bias.

3.2.1 Collapse Voltage

As mentioned in the previous section, in the presence of applied bias, a mechanical restoring force opposes the electrostatic force generated between the membrane and the bottom electrode. When an applied DC bias is increased, the electrostatic force is increased. However, as the DC bias is increased, the electrostatic force exceeds the mechanical restoring force, causing the membrane to collapse onto the bottom electrode, which is discussed in detail below. This bias at which this happens is called the "collapse voltage". While it is necessary to operate the CMUT at a bias less than the collapse voltage, to avoid the membrane collapse, the most substantial deflection can often be achieved operating as close as possible to that voltage [54].

The collapse voltage can be calculated when there is a force balance ($F_{Mass} = 0$) in the electro-mechanical system [9] such that the electrostatic force is equal and opposite to the spring force as given by:

$$F_{Electrostatic} = -F_{Spring} \qquad 3.20$$

For a DC bias, $V(t) = V_{DC}$, the membrane displacement may be calculated substituting Equations 3.6 and 3.7 into Equation 3.10, which becomes:

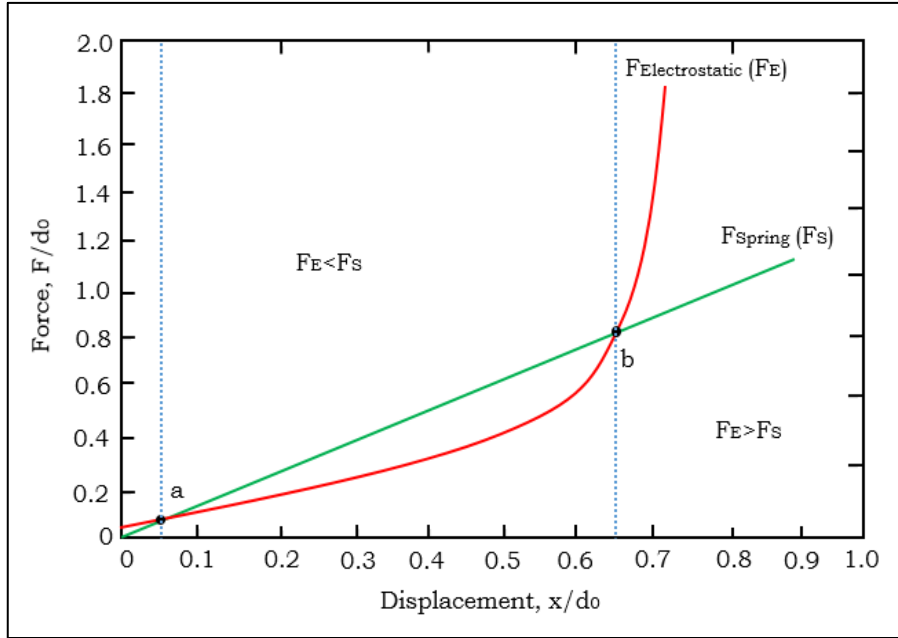

Figure 3.2. Normalized electrostatic and spring restoring force as a function of the normalized membrane displacement.

$$\frac{\varepsilon_0 A V^2}{2(d_0 - x)^2} - kx = 0 \qquad 3.21$$

The solution to the equation above (3.11) may be found using a graphical method [52] presented in Figure 3.2. The normalized value of $F_{Electrostatic}$ and F_{Spring} forces are shown as a function of normalized displacement in the figure. The force balance occurs at points 'a' and 'b', which represents the two solutions of Equation 3.11. Even though equilibrium exists at these operating points, point 'b' is found to be unstable where a further displacement of the membrane causes the electrostatic force to become greater than the spring force. This would result in the membrane to collapse onto the bottom electrode. However, at any point between 'a' and 'b', a small membrane displacement results in the spring restoring force greater than the electrostatic force. This causes the top plate to move back until it reaches the stable point 'a'. Therefore, it can be said that

for reliable operation, the rate of the increasing spring restoring force should be greater than the rate of increasing electrostatic force.

The maximum displacement for the stable condition ‘a’ can be obtained by differentiating Equation 3.11 with respect to the displacement such that [52]

$$\frac{d\left(\frac{\varepsilon_0 A V^2}{2(d_0 - x)^2} - kx\right)}{dx} < 0 \qquad 3.22$$

Equation 3.12 may be reduced to

$$\frac{\varepsilon_0 A V^2}{(d_0 - x)^3} < k \qquad 3.23$$

Substituting the value of spring constant, k from Equation 3.11 into above equation (3.13) yields

$$x < \frac{d_0}{3} \qquad 3.24$$

Hence as shown in Equation 3.14, for stable operation, the maximum membrane displacement can only be one-third of the initial gap height.

By substituting Equation 3.14 into Equation 3.11, the collapse voltage can be given by

$$V_{Collapse} = \sqrt{\frac{8k{d_0}^3}{27\varepsilon_0 A}} \qquad 3.25$$

For an increasing DC bias, the overall spring constant will be decreased due to the spring softening effect [9], described in detail in the next section. Therefore while the

collapse voltage from Equation 3.15, the spring softening effect (see Equation 3.26) has also to be considered.

3.2.2 Spring Softening Effect

An increment in the DC bias brings the membrane closure to the bottom electrode and increases the electrostatic force. This force modifies the effective spring constant of the membrane referred to as the "spring softening effect". Using a Taylor expansion of Equation 3.6 at $x = x_0$ provides a basis for this effect [9].

$$F_{Electrostatic} = \frac{\varepsilon_0 A V^2}{2(d_0 - x_0)^2}\left[1 + 2\left(\frac{x - x_0}{d_0 - x_0}\right) + \cdots\right] \qquad 3.26$$

Discarding negligible terms and at resting position ($x_0 = 0$) of the membrane, Equation 3.16 becomes

$$F_{Electrostatic} = \frac{\varepsilon_0 A V^2}{2{d_0}^2} + \frac{\varepsilon_0 A V^2}{{d_0}^3} x \qquad 3.27$$

Substituting Equation 3.17 into Equation 3.9 produces

$$m\,\frac{d^2x}{dt^2} + \left(k - \frac{\varepsilon_0 A V^2}{{d_0}^3}\right)x - \frac{\varepsilon_0 A V^2}{2{d_0}^2} = 0 \qquad 3.28$$

$$m\,\frac{d^2x}{dt^2} + K_{soft}x - \frac{\varepsilon_0 A V^2}{2{d_0}^2} = 0 \qquad 3.29$$

where K_{soft} is the effective spring constant and is given by

$$K_{soft} = k - \frac{\varepsilon_0 A V^2}{{d_0}^3} \qquad 3.30$$

It can be seen from Equation 3.20 that with an increased bias, the spring softening term will reduce the overall spring constant. Thus the membrane becomes less stiff, which

changes its vibration frequency. The effect of the spring softening effect on the resonant frequency is discussed later in Section 3.2.3.

The displacement, x of a membrane clamped at a radial distance, r can be given by [55]

$$x = \frac{3(1-\nu^2)p}{16Eh^3}(R^2 - r^2)^2 \tag{3.31}$$

where ν is the Poisson's ratio of the material of the membrane, E is the Young's modulus of the material of the membrane, R is the membrane radius, h is the membrane thickness, and P is the uniformly distributed pressure due to an applied bias. For a clamped membrane maximum displacement, x_{max} occurs at the center of the membrane where $r = 0$ and is:

$$x_{max} = \frac{3(1-\nu^2)p}{16Eh^3}R^4 \tag{3.32}$$

The force resulting from the pressure (p) is equal and in the opposite direction to the spring force (F_{spring}) and can be written as:

$$p = \frac{F}{A} = \frac{-F_{spring}}{\pi R^2} \tag{3.33}$$

Substituting Equation 3.23 into Equation 3.22 and then rearranging, the spring force can be given by,

$$F_{spring} = -\frac{16\pi Eh^3}{3(1-\nu^2)R^2}x_{max} \tag{3.34}$$

Using Equation 3.7 ($F_{Spring} = -kx$) and Equation 3.24, the spring constant may be given as

$$k = \frac{16\pi E h^3}{3(1 - \nu^2)R^2} \qquad 3.35$$

The collapse voltage of a particular device can be calculated by substituting k (Equation 3.25) into Equation 3.15.

Substituting Equation 3.25 into Equation 3.20, the effective spring constant, including the spring softening effect, becomes

$$K_{soft} = \frac{16\pi E h^3}{3(1 - \nu^2)R^2} - \frac{\varepsilon_0 A V^2}{{d_0}^3} \qquad 3.36$$

For a polysilicon membrane, the collapse voltage for a 65 µm radius device can be calculated as 48.9 V (Equations 3.26 and 3.15). The bias dependence of the effective spring constant derived in the Equation (3.26) above is also shown in Figure 3.3. The parameters used to calculate both the collapse voltage and the effective spring constant are tabulated in Table 3.1.

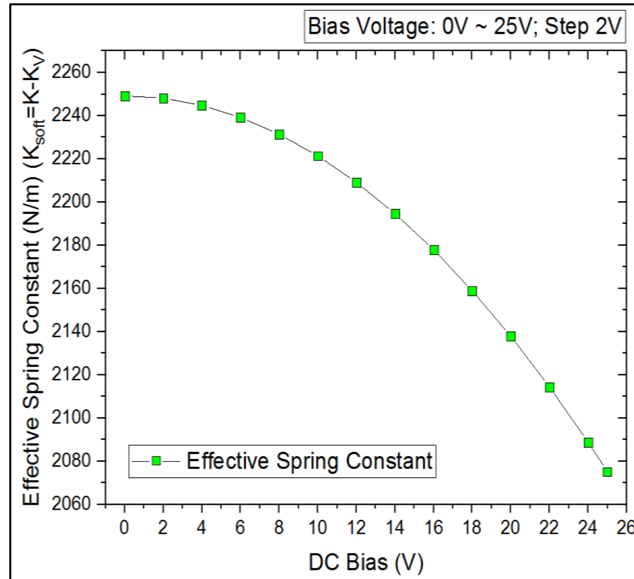

Figure 3.3. The effective spring constant of a vibrating membrane as a function of applied bias for a given membrane (r = 65 µm radius) CMUT with a given thickness (h = 1.5 µm) and gap height (d_o = 0.75 µm).

Table 3.1. Parameters used for the theoretical calculation of the collapse voltage and the effective spring constant.

Parameter	Symbol	Value	Unit
Young's modulus	E	160	GPa
Poisson's ratio	ν	0.22	NA
Density	ρ	2320	$\mathrm{kg.m^{-3}}$
Permittivity of free space	ε_0	8.854×10^{-12}	$\mathrm{F.m^{-1}}$
Membrane thickness	h	1.5	μm
Membrane radius	R	65	μm
Initial gap height (air gap)	d_0	0.75	μm
Bias voltage	V	0~25	V

3.2.3 Resonant Frequency

The circular frequency or natural angular frequency, ω of a vibrating plate can be given by [36]

$$\omega = \sqrt{\frac{k}{M}} \quad 3.37$$

such that

$$f_r = \frac{1}{2\pi}\sqrt{\frac{k}{M}} \quad 3.38$$

where f_r is the resonant frequency of the vibrating membrane, and M is the effective mass of the membrane. The effective mass of the membrane can be given by [36]

$$M = 2\sqrt{2}\frac{\rho h A}{(\lambda_a)_{mn}} \quad 3.39$$

where ρ is the density of the material of the membrane, and $(\lambda_a)_{mn}$ is the constant corresponding to the vibrational modes of the circular membrane where m and n denote nodal diameter and circular node respectively. For the fundamental mode ($m = 0$ and $n = 1$), the value of the constant is $(\lambda_a)_{01} = 3.196$ [56].

Substituting the effective spring constant (Equation 3.26) and membrane effective mass (Equation 3.29) into Equation 3.28 above, the resonant frequency can be given by

$$f_r = \frac{1}{2\pi}\sqrt{\frac{(\lambda_a)_{01}}{2\sqrt{2}\rho h A}\left[\frac{16\pi E h^3}{3(1-\nu^2)R^2} - \frac{\varepsilon_0 A V^2}{{d_0}^3}\right]} \qquad 3.40$$

Using Equation 3.30, the spring softening effect for a 65 μm radius device is shown in Figure 3.4. The parameters used to calculate the resonant frequency at different biases are given in Table 3.1. For example, the resonant frequency at 25 V bias is just slightly greater than 1.13 MHz.

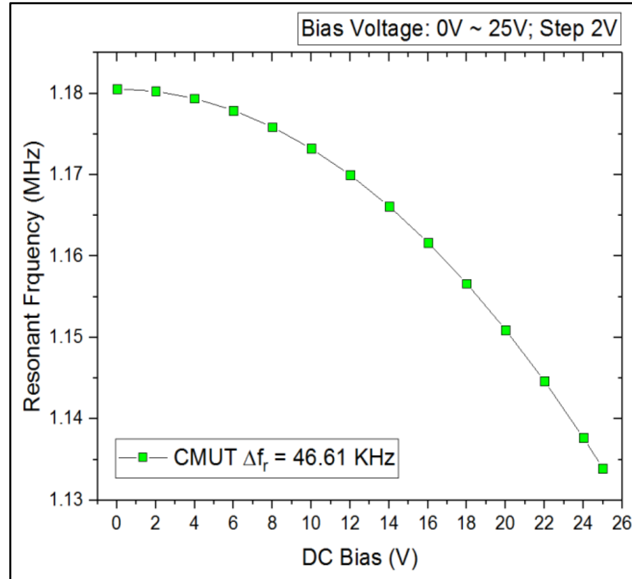

Figure 3.4. The resonant frequency shift of a vibrating membrane as a function of applied bias for a given CMUT with a membrane, $r = 65$ μm, a thickness, $h = 1.5$ μm and a gap height, $d_o = 0.75$ μm.

It can be seen from Equation 3.30 and Figure 3.4 that there is a decrease in the resonant frequency with increasing DC bias. It can be deduced from the same equation that by optimizing membrane radius, membrane thickness, and gap height between the membrane and the electrode, a suitable resonant frequency can be achieved for a particular DC bias.

3.3 Dynamic Analysis of the Analytical Model

As discussed in Section 2.4, in transmission mode, a CMUT requires a DC bias for the optimum membrane displacement and an ac bias to create the membrane vibration for generating the acoustic waves. Therefore a dynamic analysis, where an ac bias is superimposed with DC bias such as, $V(t) = V_{DC} + V_{ac} sin(\omega t)$, is required to model the transmission mode behavior of CMUT.

With the time-varying bias, Equation 3.6 becomes

$$F_{Electrostatic} = \frac{\varepsilon_0 A}{2(d_0 - x)^2}\left[\left({V_{DC}}^2 + \frac{1}{2}{V_{ac}}^2\right) + 2V_{DC}V_{ac}\sin(\omega t) - \frac{1}{2}{V_{ac}}^2\cos(2\omega t)\right] \quad 3.41$$

When a CMUT is operating at its primary resonant frequency, the cosine term of Equation (3.31) is small enough to neglect, which yields

$$F_{Electrostatic} = \frac{\varepsilon_0 A}{2(d_0 - x)^2}\left[\left({V_{DC}}^2 + \frac{1}{2}{V_{ac}}^2\right) + 2V_{DC}V_{ac}\sin(\omega t)\right] \quad 3.42$$

If $V_{DC} \gg V_{ac}$, then Equation 3.32 becomes

$$F_{Electrostatic} = \frac{\varepsilon_0 A}{2(d_0 - x)^2}\left({V_{DC}}^2 + 2V_{DC}V_{ac}\right) \quad 3.43$$

which when expanded becomes

$$F_{Electrostatic} = \frac{\varepsilon_0 A}{2(d_0 - x)^2} {V_{DC}}^2 + \frac{\varepsilon_0 A}{2(d_0 - x)^2} V_{DC} V_{ac} \qquad 3.44$$

The first term in Equation 3.34 corresponds to the reduction of the gap height while the second term to the production of the acoustic waves.

3.3.1 Transformation Ratio

The energy conversion in transmitting and receiving mode of a CMUT can be determined by using an equivalent circuit [9], as shown in Figure 3.5. The system is an electrical circuit comprised of a transformer with a "transformation ratio" denoted as "n". The transformation ratio is determined by the conversion of a mechanical quantity to an electrical quantity (or vice-versa).

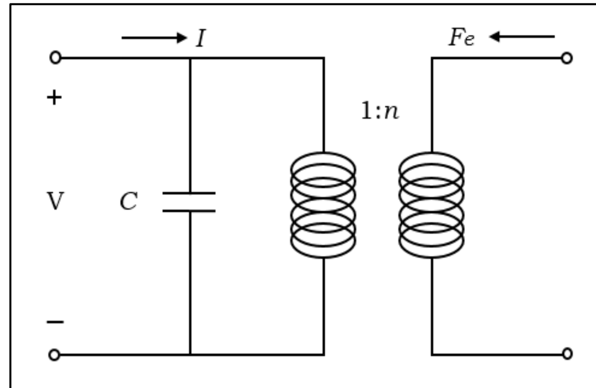

Figure 3.5. Equivalent electrical circuit model of CMUT.

The capacitance of the above circuit can be found by taking into account all the capacitances associated with the top membrane and the gap between it and the fixed electrode. Using the simple capacitance expression (see Equation 3.3) the series capacitance of the membrane and the gap can be calculated as below.

$$C = \frac{\varepsilon_0 \varepsilon_m A}{\varepsilon_0 h + \varepsilon_m (d_0 - x)} \qquad 3.45$$

where ε_m is the relative permittivity of the membrane and h is the thickness of the membrane and d_0 is the initial gap height.

With the applied bias $V(t) = V_{DC} + V_{ac}sin(\omega t)$, where $V_{DC} \gg V_{AC}$, the electrostatic force from Equation 3.2 (Section 3.1) becomes

$$F_{Electrostatic} = -\frac{1}{2}V^2\left[\frac{d}{dx}\left(\frac{\varepsilon_0\varepsilon_m A}{\varepsilon_0 h + \varepsilon_m(d_0 - x)}\right)\right] = \frac{\varepsilon_0\varepsilon_m A {V_{DC}}^2}{2\left(\varepsilon_0 h + \varepsilon_m(d_0 - x)\right)^2} \qquad 3.46$$

The current, charging the capacitor, can be given by [9]

$$I = \frac{d}{dt}Q = \frac{d}{dt}C(t)V(t) = C(t)\frac{d}{dt}V(t) + V(t)\frac{d}{dt}C(t) \qquad 3.47$$

$$I = C(t)\frac{d}{dt}V_{ac}sin(\omega t) + V_{DC}\frac{d}{dt}C(t) \qquad 3.48$$

where Q is the charge density in the capacitor.

For a small signal ac voltage ($V_{DC} \gg V_{ac}$), the capacitance of the circuit may be written as $C(t) = C_{DC} + C_{ac}sin(\omega t)$. Furthermore, the displacement of the membrane is minimal compared to the gap height (i.e., $C_{DC} \gg C_{ac}$). Therefore, using this approximation, Equation 3.38 becomes

$$I = C_{DC}\frac{d}{dt}V_{ac}(t) + V_{DC}\frac{d}{dt}C_{ac}(t) \qquad 3.49$$

Differentiating Equation 3.35 with respect to time, yields,

$$\frac{d}{dt}C(t) = -\left[\frac{\varepsilon_0{\varepsilon_m}^2 A}{\left(\varepsilon_0 h + \varepsilon_m(d_0 - x)\right)^2}\right]\frac{d}{dt}x(t) \qquad 3.50$$

where $\frac{d}{dt}x(t) = v$ is the instantaneous velocity of the membrane at the center (r = 0).

Substituting Equation 3.40 into Equation 3.39, the current (I) becomes

$$I = C_{DC}\frac{d}{dt}V_{ac} - V_{DC}\left[\frac{\varepsilon_0 {\varepsilon_m}^2 A}{\left(\varepsilon_0 h + \varepsilon_m (d_0 - x)\right)^2}\right] v \tag{3.51}$$

Equation (3.41) can be therefore used to describe the transformation of the membrane velocity (a mechanical quantity), into an electrical current. The transformation ratio for a CMUT-like device when receiving an acoustic signal can be defined by [9]

$$n = \frac{I}{v} = \left[\frac{\varepsilon_0 {\varepsilon_m}^2 A}{\left(\varepsilon_0 h + \varepsilon_m (d_0 - x)\right)^2}\right] V_{DC} \tag{3.52}$$

The transformation ratio in Equation 3.42 demonstrates that

$$n \propto V_{DC} \tag{3.53}$$

or

$$n \propto \frac{1}{(d_0 - x)^2} \tag{3.54}$$

The transformation ratio is determined by the energy conversion of the input acoustic power and the electrical current that it generates in the transducer. Equations 3.43 and 3.44 show that the transformation ratio can be specified using the bias voltage and the effective gap height. Therefore, these parameters have a significant effect on the transducer's power transmission and reception sensitivity.

Chapter 4 Finite Element Model of the CMUT & M^3-CMUT

Finite element modeling (FEM) has been used to investigate the preliminary transducer characteristics. For a better understanding and reliability, the FEMs for both CMUT and M3-CMUT devices were designed and assessed and are presented in this chapter. These FEM models were derived from the analytical model provided in the previous chapter.

4.1 Design Consideration from the FEM

The software program, COMSOL Multiphysics (version 5.3) [57], is a finite element simulation software that was used to model [28] the CMUT and M^3-CMUT transducers. Based on the application areas of a model, COMSOL Multiphysics provides various physics-based studies, such as electrical, mechanical, fluid, chemical, etc. For the FEM simulations of the CMUT and M^3-CMUT devices, the “Electromechanics (emi)” physics from the “Structural Mechanics” module was used. The module allows the analysis of mechanical structures that are subjected to change in the presence of a static or dynamic load.

There are several design simplifications [28] for the 3-D FEMs of CMUT and M^3-CMUT. The edge curvatures and etching holes of different structural layers were ignored for the simplification of geometry in finite element analyses. All layers were considered to be flat at the beginning of the simulation. Moreover, the insulation (nitride) and substrate layers were ignored to reduce the computation time for simulation. The diameter of the membranes was extended only to the clamped edge of the membrane post (i.e., anchors/beams), as shown in Figure 4.1.

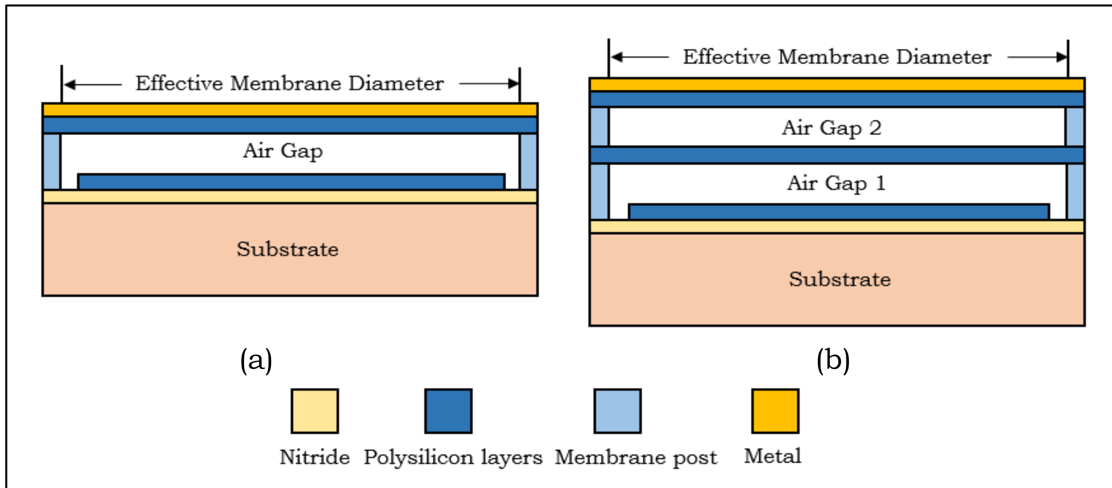

Figure 4.1. Effective Membrane diameter of (a) CMUT and (b) M^3-CMUT.

The FEM model of a circular CMUT includes a membrane suspended over a bottom electrode separated from the bottom contact by a cavity (air gap). On top of the membrane, a metal layer was added for the contact of electric potential. The materials of the membrane and metal layers were chosen as polysilicon and gold (Au), respectively. The bottom electrode consists of two poly layers deposited onto each other. Both the CMUT and M^3-CMUT incorporated two poly layers in their fabrication and is discussed in detail in Chapter 5. The effective radii of the material layers used in this modeling are shown in Figure 4.1. The top membrane was allowed to vibrate and biased, while the bottom electrode was fixed and grounded.

In the model used for the M^3-CMUT, a second air gap was introduced in between the two poly layers. The new membrane was formed in the middle of the original CMUT gap, as was described in Section 2.4.1. The radii and the other structural layers thicknesses remained the same as in the CMUT design. The middle membrane was allowed to vibrate along with the top membrane. The bottom layer was fixed. Both the middle membrane and the fixed bottom layer were grounded in this model.

The 2-D cross-sectional view of the respective finite element models are shown in Figure 4.2. The design parameters used in the 3-D FEMs of CMUT and M^3-CMUT are listed in Table 4.1. Here, the thicknesses of the layers were chosen based on the design rules specified in the PolyMUMPs (i.e., the method used for fabricating the devices) process of MEMSCAP, Inc. and the effective radii were selected according to the intended design of the devices. The properties of the materials used in these models are presented in Table 4.2.

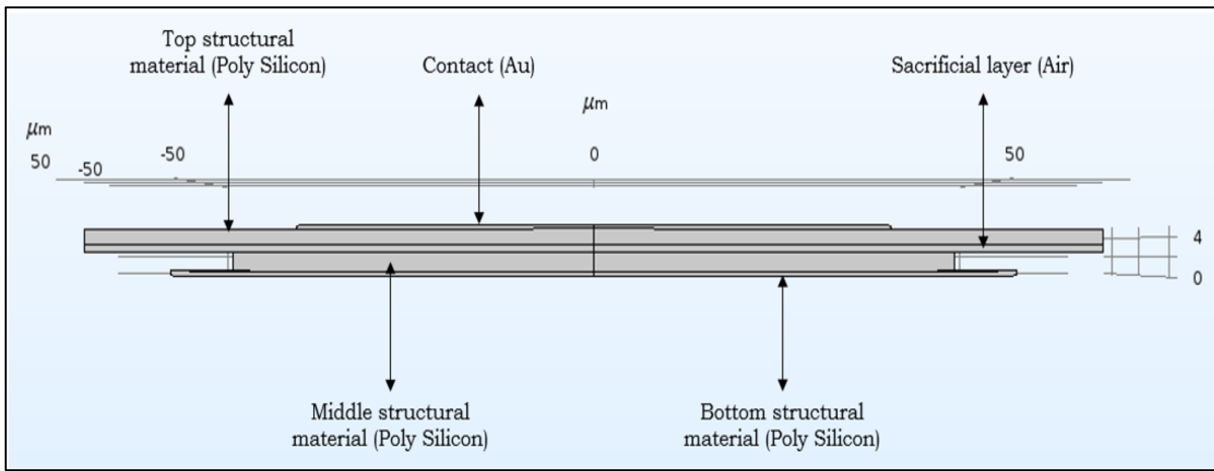

(a)

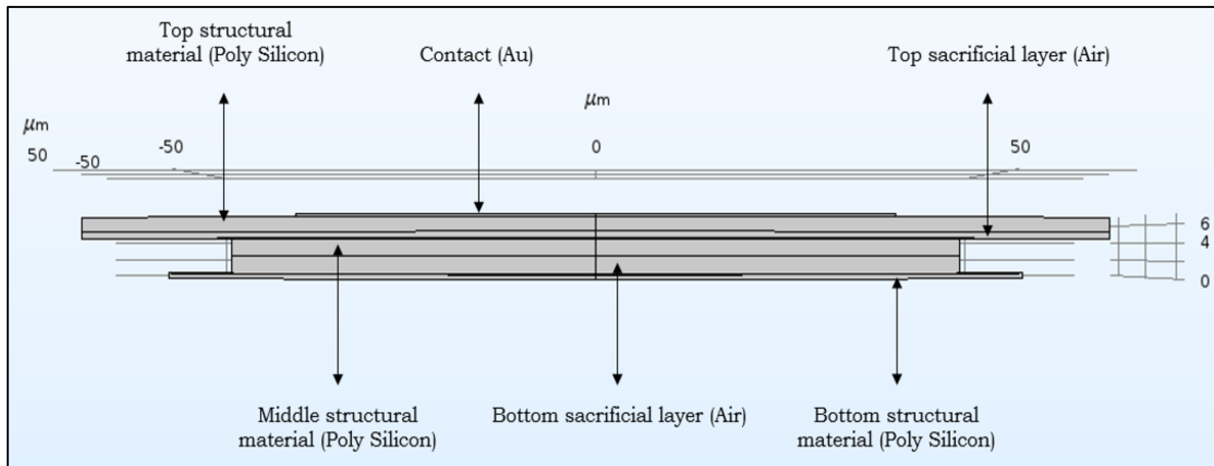

(b)

Figure 4.2. 2-D cross-sectional view of the FEMs of (a) CMUT and (b) M^3-CMUT.

Table 4.1. Design parameters of the 3-D FEMs of CMUT and M^3-CMUT.

Parameter	**Value (μm)**	
	CMUT	**M^3-CMUT**
Metal (Au) thickness	0.46	0.46
Metal (Au) radius	38	38
Top polysilicon layer thickness	1.6	1.6
Top polysilicon layer radius	65	65
Air gap (cavity) thickness	0.75	0.75
Air gap (cavity) radius	65	65
Middle polysilicon layer thickness (suspended layer for M^3-CMUT)	2	2
Middle polysilicon layer radius (suspended layer for M^3-CMUT)	46	42
Bottom polysilicon layer thickness	0.5	0.5
Bottom polysilicon layer radius	54	54
Bottom air gap thickness	NA	2
Bottom air gap radius	NA	42

Table 4.2. Properties of the materials used in the 3-D FEMs of CMUT and M^3-CMUT.

Part A: Common material properties		
Property	**Value**	**Unit**
Permittivity of free space	8.854×10^{-12}	$\mathrm{F.m^{-1}}$
Temperature	20	℃

Part B: Individual material properties				
Property	**Value**			
	Gold (Au)	**Polysilicon**	**Air**	**Unit**
Density	19300	2320	1.23	$\mathrm{kg.m^{-3}}$
Young's modulus	70	160	NA	GPa
Poisson's ratio	0.44	0.22	NA	NA
Relative permittivity	6.9	4.5	1	NA

4.2 Static Analysis of the FEM

The relationship between the force due to the applied bias and the displacement in a FEM can be obtained from the static analysis. For the static comparison between the CMUT and M^3-CMUT, COMSOL module's "Electromechanics (emi)" physics including the "Stationary" study and "Eigen Frequency" study, were carried out.

4.2.1 Stationary Study from COMSOL

For the stationary simulation, a DC bias was applied to the top polysilicon layer (membrane) of CMUT and M^3-CMUT. The middle and bottom polysilicon layers (bottom electrode) were grounded. Due to the applied bias, the membrane experienced a displacement towards the bottom electrode. The displacement was at a maximum at the center of the clamped membrane (Figure 4.3 (a)). In the case of the M3-CMUT, the middle membrane (middle structural material) was allowed to vibrate as well. With the applied bias, it experienced a displacement moving it towards the top membrane (Figure 4.3 (b)).

The applied DC bias was chosen as 100 V for the stationary simulation, the displacement profiles of which are shown in Figure 4.3. These profiles were enlarged for better viewing. According to process parameters, as shown in Table 4.1, the initial cavity of the structures was 750 nm (without any displacement of the membrane). As shown in Figure 4.3 (a), the membrane displacement (at 100 V) for the CMUT was found to be 108 nm, which means the effective gap height was reduced to 642 nm. For the M^3-CMUT, the top membrane displacement was 129 nm, and the middle membrane displacement was 28 nm towards each other, as illustrated in Figure 4.3 (b). The total displacement in M^3-CMUT was found to be 157 nm, which reduced the cavity to 593 nm; 49 nm less than the conventional CMUT.

As stated earlier, one of the goals of this thesis was to demonstrate that the new M3-CMUT design, for a given applied bias, had a lower effective cavity height. From the stationary (DC) simulations, it was shown that the M3-CMUT has a greater membrane deflection than the CMUT, which leads to a lower effective cavity height.

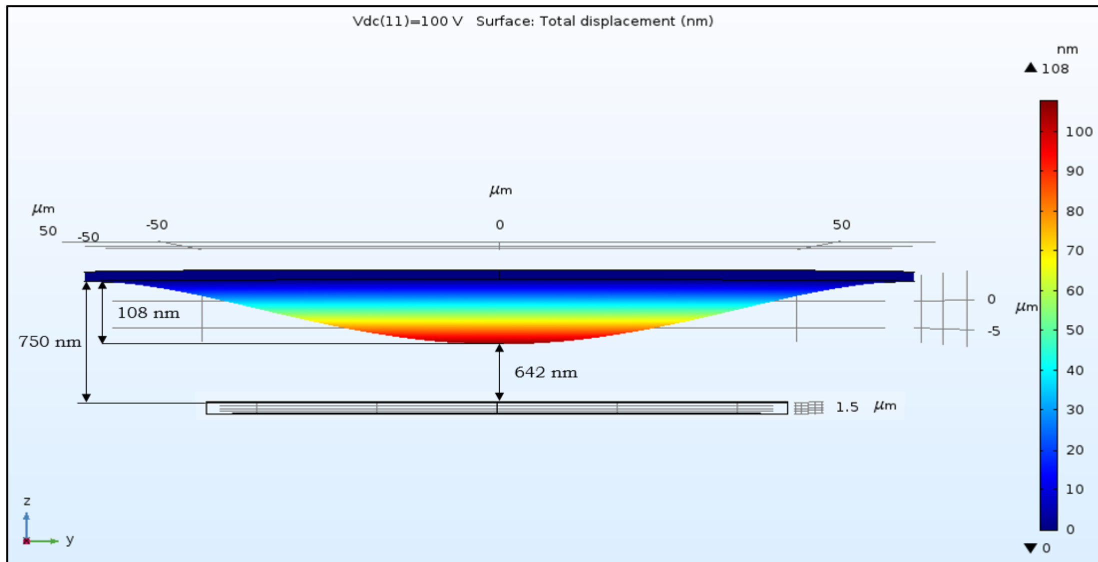

(a)

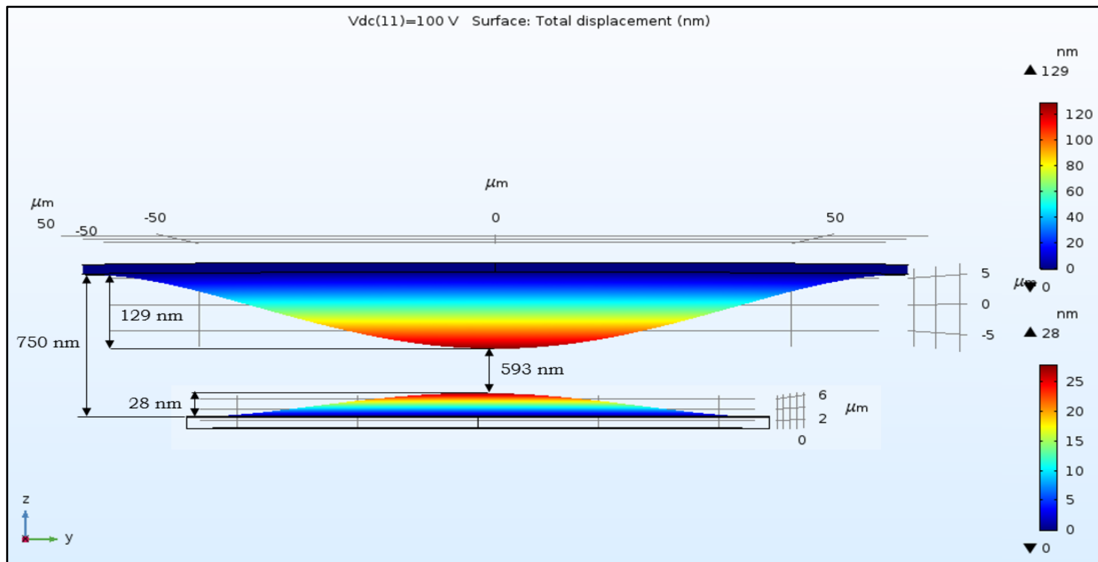

(b)

Figure 4.3. Static displacement of 65 μm radius (a) CMUT and (b) M3-CMUT at a given DC bias (100 V) applied to the membrane and the grounded bottom electrode.

4.2.1.1 Collapse Voltage Comparison

As discussed in Section 3.2.1, the collapse voltage can be found when the membrane reaches one-third of the cavity of the device. From the stationary study, a DC voltage can be recorded when a membrane moved to this maximum allowed displacement.

Since the cavity of the CMUT and M^3-CMUT model was 750 nm (see Table 4.1), the maximum displacement allowed for their membrane would be 250 nm. The voltages required to get this deflection for CMUT and M^3-CMUT were simulated to be 148 V and 117 V, respectively. This demonstrates that, for a given displacement, the M^3-CMUT can be operated at a lower voltage than the CMUT before going into the collapse region.

4.2.1.2 Membrane Displacement Comparison

A range of DC biases was applied to investigate the membrane displacement of CMUT and M^3-CMUT. The membrane displacement, as a function of bias, is shown in

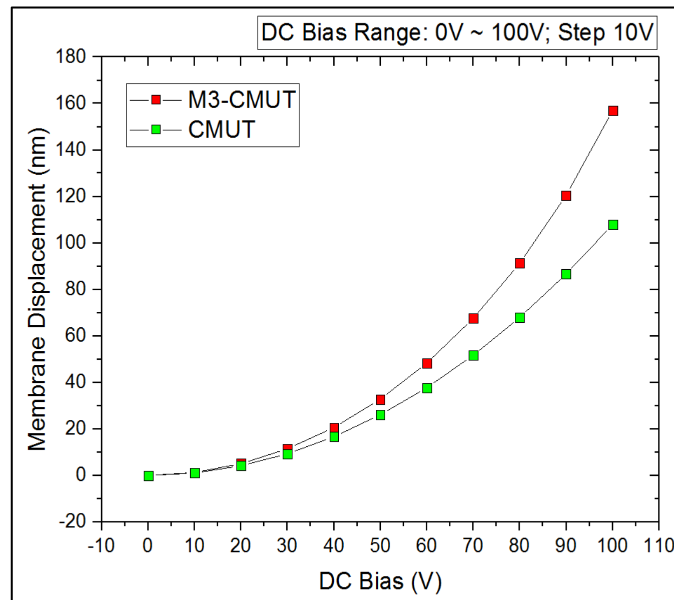

Figure 4.4. Membrane displacement of 65 μm radius CMUT and M^3-CMUT at a given DC bias ranging from 0 V to 100 V.

Figure 4.4. It can be observed that with for a given DC bias, the M^3-CMUT model presented more membrane displacement than the CMUT model. It is known that the electrostatic force increases with increased bias, which results in increased membrane deflection. However, M^3-CMUT produced greater membrane deflection with the help of its second vibrating membrane. This means that a specific displacement can be achieved at a lower voltage in M^3-CMUT. Therefore, the required driving voltage is lower in M^3-CMUT relative to the CMUT [58], which is demonstrated later in the characterizations of these devices.

4.2.2 Eigen Frequency Study from COMSOL

In the "Eigen Frequency" simulation, a FEM model can be set to vibrate at an "eigenfrequency" which bends the membrane into a corresponding mode of vibration, called "eigenmode", of that frequency. The resonant frequency and the spring softening effect of the model can be obtained from this simulation.

4.2.2.1 Resonant Frequency Comparison

Electromechanical Eigen frequency simulation was performed to investigate the mode of vibration of the FEM structures. For example, a 25 V DC bias (i.e., the same voltage used for the analytical resonant frequency calculation in Section 3.2.3) was applied for the analysis. The first six modes of vibration of CMUT are shown in Figures 4.5 (a), 4.5 (b), 4.5 (c), 4.5 (d), 4.5 (e) and 4.5 (f). The modes of vibration for the M^3-CMUT are illustrated in Figures 4.5 (g), 4.5 (h), 4.5 (i), 4.5 (j), 4.5 (k), and 4.5 (l).

It can be observed that the 1st eigenmode of both designs provided circularly symmetrical vibrations with the maximum displacement occurring at the center of the membrane. The rest of the modes demonstrated non-uniform displacement profiles.

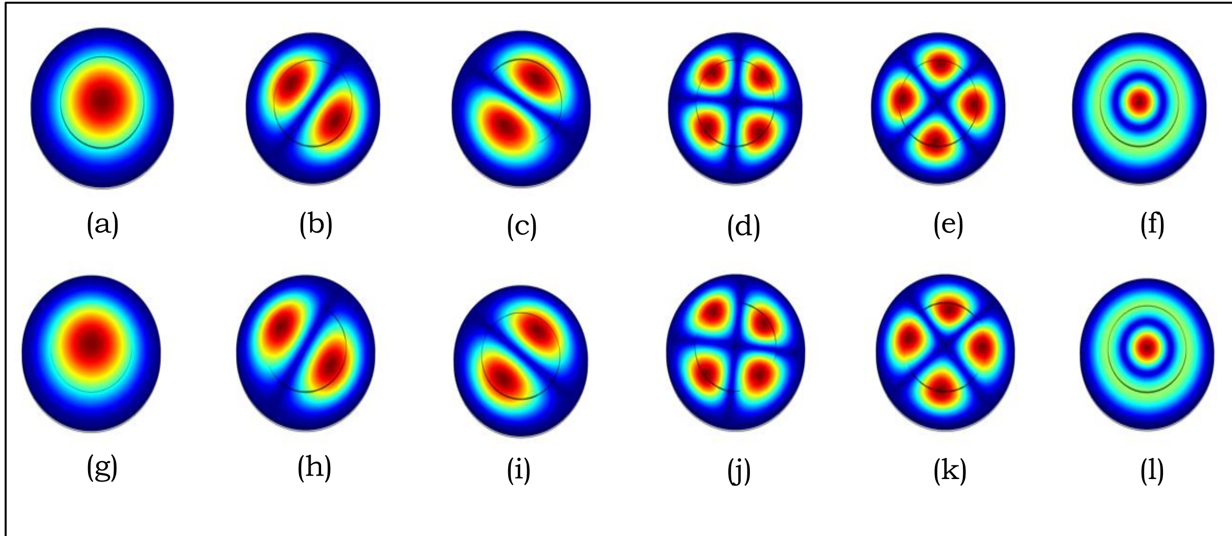

Figure 4.5. First six modes of vibration of 65 µm radius CMUT (a), (b), (c), (d), (e), and (f) and M3-CMUT (g), (h), (i), (j), (k), and (l) at a given DC bias (25 V).

These displacement profiles depend on the number of nodal diameter (m) and circular node (n) of a mode. The first six eigenfrequencies of CMUT and M3-CMUT (with the device properties mentioned in Table 4.1 and 4.2) obtained from the Eigen frequency simulation along with their number of nodal diameter and circular node are presented in Table 4.3.

Table 4.3. First six eigenfrequencies of 65 µm radius CMUT and M3-CMUT at 25 V DC bias.

Eigenmode	**Nodal Diameter (m)**	**Circular Node (n)**	**Eigenfrequency (MHz)**	
			CMUT	**M3-CMUT**
1	0	1	0.968	0.964
2	1	1	2.192	2.190
3	1	1	2.192	2.190
4	2	1	3.820	3.787
5	2	1	3.820	3.787
6	0	2	4.491	3.820

The 1st eigenfrequency of a structure is considered to be the fundamental resonant frequency. From Table 4.3, the resonant frequency of 65 μm radius CMUT and M^3-CMUT devices were found to be very close to each other; 0.968 MHz and 0.964 MHz, respectively.

It can be observed from Equation 3.28 (Section 3.2.3) that the resonant frequency is proportional to the effective spring constant of a device. For a particular bias, this effective spring constant reduces with the decreasing effective cavity of that device (Equation 3.20). In section 4.2.1, it was shown that the effective cavity (for a given bias) was lower in the M^3-CMUT than in that of the CMUT. Therefore, according to Equation 3.30, the resonant frequency of M^3-CMUT is less, which agrees with the fundamental mode values presented in Table 4.3. The resonant frequency of M^3-CMUT was found to be 3.24 kHz lower than the CMUT.

4.2.2.2 Spring Softening Effect Comparison

A range of DC bias was applied to investigate the spring softening effect in the FEMs of CMUT and M^3-CMUT, which are shown in Figure 4.6. As discussed in Section 3.2.2, an increasing bias causes a shift (lowering) in the resonant frequency of the vibrating membrane. This suggests that the membrane becomes less stiff and therefore vibrates more.

It was observed that both CMUT and M^3-CMUT experienced the frequency shift with the increasing bias, but M^3-CMUT (~20.3 kHz) provided a more significant shift ($\Delta f = f_{V=50\,V} - f_{V=5\,V}$) with respect to CMUT (~6.3 kHz). This greater resonance shift of M^3-CMUT suggests that it has a smaller effective cavity height than the CMUT.

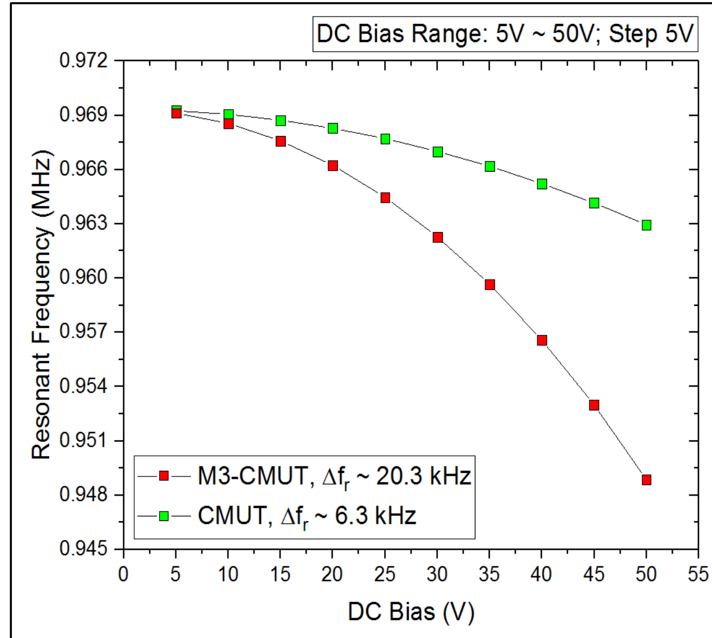

Figure 4.6. Frequency shift due to the spring softening effect of 65 μm radius CMUT and M^3-CMUT at a given DC bias ranging from 5 V to 50 V.

4.3 Dynamic Analysis of the FEM

The devices behavior over a sweeping parameter can be obtained from the dynamic analysis. An ac bias was superimposed with a DC bias for the dynamic operation of the same geometry stated in the static FEM model. Electromechanical "Frequency Domain Perturbation" study and "Time Dependent" study were used to observe the variant behavior of the systems.

4.3.1 Frequency Domain Perturbation Study from COMSOL

Frequency domain perturbation study was performed to find out the membrane displacement as a function of frequency. A parametric sweep over a chosen range of frequency is shown in Figure 4.7. The frequency range for CMUT and M^3-CMUT was selected from 0.96 to 0.972 MHz. This range was based on the transducer's resonant frequency from the previously discussed Eigen frequency study (Section 4.2.2). The step

size for the simulation was 100 kHz for both transducers. Along with the 25 V DC bias (as used in the resonant frequency comparison in Section 4.2.2.1), a 50 mV ac bias was applied to the membrane to create the oscillations required for the frequency domain analysis.

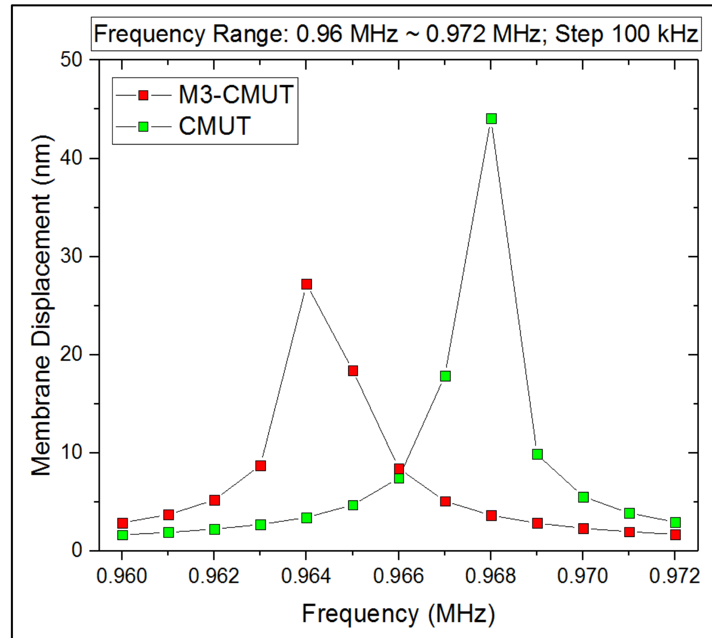

Figure 4.7. Peak membrane displacement and resonant frequency dependence for a 65 µm radius CMUT and M³-CMUT. The models were biased at 25 V DC superimposed with a 50 mV ac bias.

It can be seen from Figure 4.7 that the peak displacement was found at 0.968 MHz for the CMUT model. This value agrees very well with the resonant frequency obtained from the Eigen frequency study. Likewise, the highest displacement was found at 0.964 MHz for the M³-CMUT also agreeing well with its 1st Eigen frequency value presented in Table 4.3.

According to the discussion in Eigen frequency simulation in Section 4.2.2.1, a lower resonant frequency occurs due to a lower effective cavity. From the frequency domain study, it was found that the resonant frequency of M³-CMUT was lower than

that of the CMUT. This suggests that the effective gap height is less in M³-CMUT relative to the CMUT.

4.3.2 Time Dependent Study from COMSOL

Time dependent study was performed to observe the response of the membrane over time. The same DC (25 V) and ac (50 mV) bias as the frequency domain study were used for the time dependent study. The simulation frequency of 1 MHz was chosen close to the resonant frequency of CMUT (0.968 MHz) and M³-CMUT (0.964 MHz). The displacement of the CMUT membrane as a function of time is shown in Figure 4.8. The time was swept from 0 μs to 10 μs with a step size of 0.1 μs.

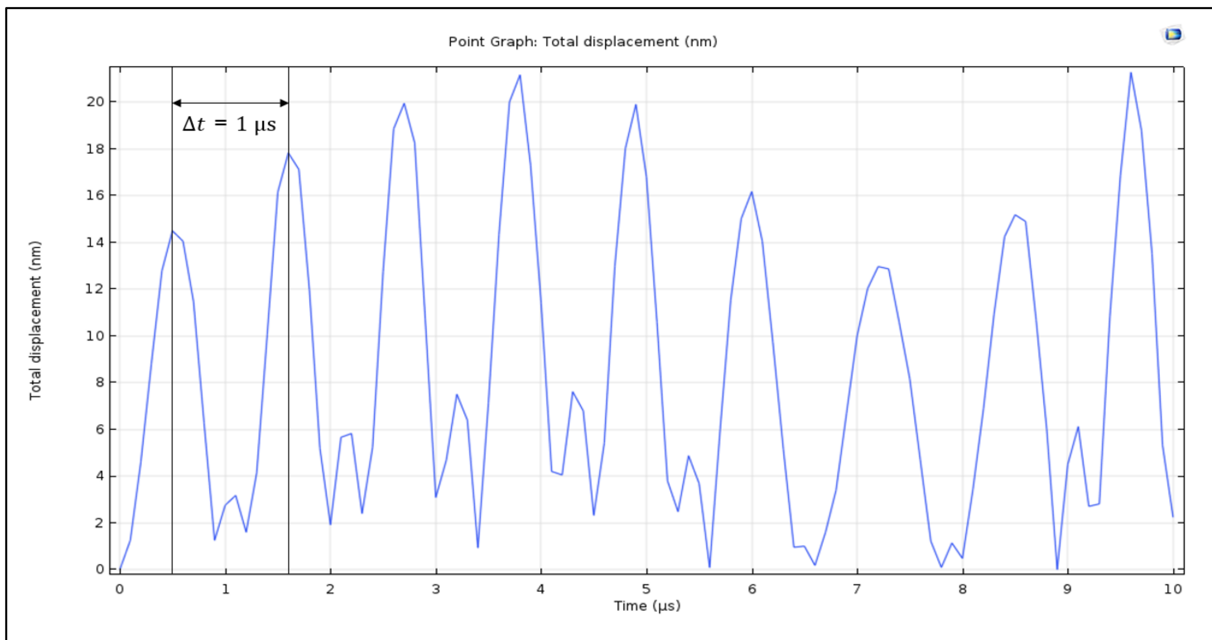

Figure 4.8. Driven response of the 65 μm radius membrane of CMUT, biased at 25 V DC superimposed by a 1 MHz, 50 mV ac bias.

As shown in the figure, the time interval (Δt) between the two consecutive peaks of membrane displacement was found as ~1 μs. The average of nine (9) consecutive peaks can be calculated as ~1 μs (± 0.01 μs). This average value corresponds to a

frequency $\left(f = {}^{1}/_{\Delta t}\right)$ of ~1 MHz ($\pm$ 0.01 MHz). The smaller peaks at the bottom of the graph are due to the displacement of the vibrating membrane from its initial position (V_{DC} = 0 V) to the upward direction (opposite of the bottom electrode).

The M3-CMUT has multiple membrane deflection. The displacement of the top vibrating membrane over time is illustrated in Figure 4.9. The average time period for the M3-CMUT device was found around 1.1 μs ($\pm$ 0.01 μs), which gives the frequency value of ~0.91 MHz ($\pm$ 0.01 MHz).

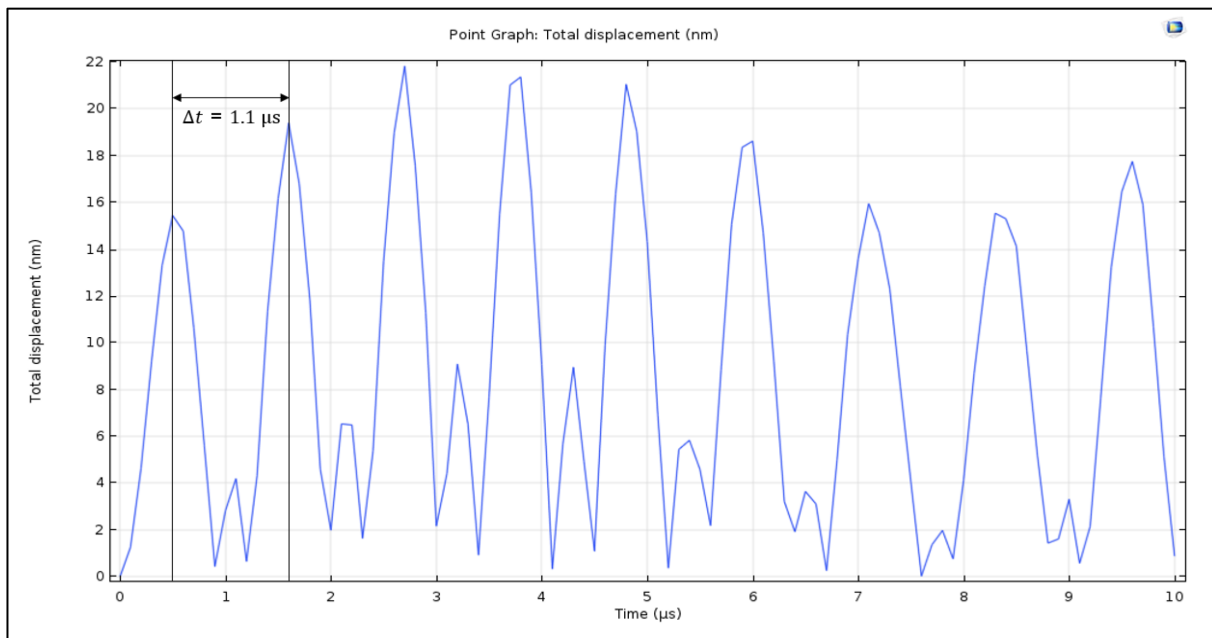

Figure 4.9. Driven response of the 65 μm radius top membrane of M3-CMUT, 25 V DC bias superimposed by a 1 MHz, 50 mV ac bias.

The result of time dependent study echoes the findings of other frequency analysis (i.e., Eigen frequency and frequency domain perturbation) stated above. The lower frequency value in M3-CMUT indicates a smaller cavity with respect to a similar membrane-sized CMUT.

Chapter 5 Design and Fabrication of the CMUT & M^3-CMUT

Based on the simulations performed using the FEM software COMSOL Multiphysics (as discussed in Chapter 4), single-cell CMUT and M^3-CMUT devices, as well as some 1-D and 2-D arrays of these devices, were designed and fabricated. The transducers were initially designed by Dr. Arezoo Emadi. There are a number of devices with variable dimensions in her design. However, the thesis is based on a particular 65 μm radius device since its 2-D arrays were used for the air-coupled measurements (as will be described in Chapter 7). The design consideration and fabrication process of this specific design are discussed in this chapter.

5.1 Design Consideration

The physical layouts of various CMUT and M^3-CMUT devices [28] were drawn using L-Edit, a CAD tool from MEMS Pro [59]. L-Edit is a layout editor which is used to draw the 2-D geometry of a MEMS structure. The material and masking layers of the structure are represented by various colors in the editor. A 3-D representation can also be generated from the 2-D structure.

The L-Edit layouts of the single-cell M^3-CMUT and CMUT devices are shown in Figures 5.1 (a) and 5.1 (b), respectively. The 3-D cross-sections of the M^3-CMUT and CMUT devices are also shown in Figures 5.1 (c) and 5.1 (d), respectively. To produce an individual device, an M^3-CMUT/CMUT cell was connected to metal contact on the top membrane and ground connection at the bottom electrode. The cells were replicated and connected in the same manner to make the corresponding 1-D and 2-D arrays.

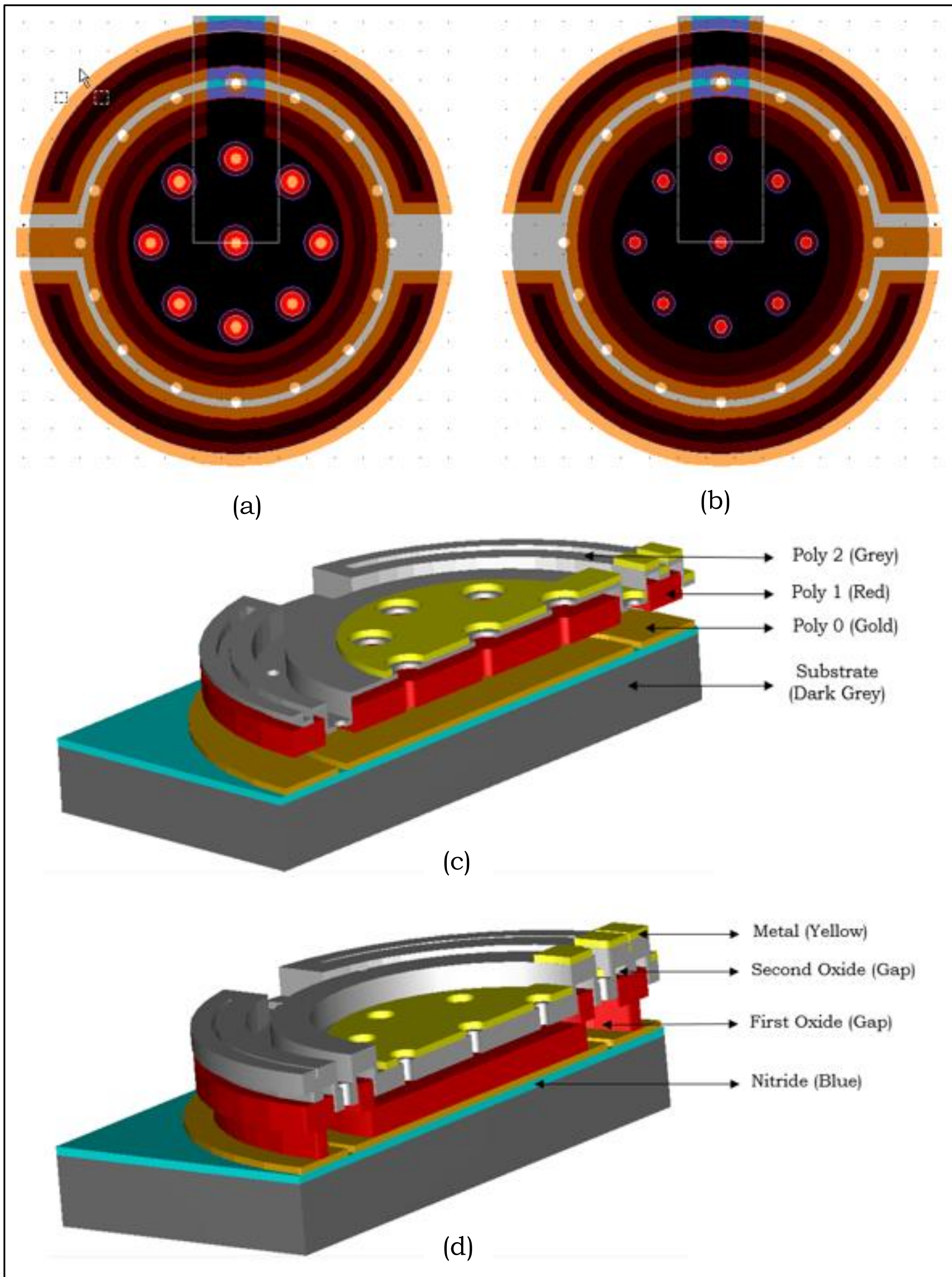

Figure 5.1. Top view of (a) M^3-CMUT and (b) CMUT cell and 3-D cross-sections of (c) M^3-CMUT and (d) CMUT cell.

The dimensions of the CMUT and M3-CMUT layouts are given in Table 5.1. The layers used in the L-Edit represent the material layers, masking layers, and etch (release) holes of the PolyMUMPS process [60]. The process is discussed in detail in Section 5.3. The two radii (i.e., 57/77 for Poly0) as listed in the table below defines a ring-shaped structure with an inner (57 μm) and an outer (77 μm) radius.

Table 5.1. Dimensions of the CMUT and M3-CMUT cell used in the L-Edit layout.

L-Edit Layer	**Radius (μm)**			
	CMUT		**M3-CMUT**	
	Inner	**Outer**	**Inner**	**Outer**
Poly0	54	57/77	54	57/77
Anchor1	46	65/69	42/46	65/69
Poly1	50	61/73	50	61/73
Poly1-Poly2 Via	65/69		65/69	
Poly2	73		73	
Metal	38		38	
HoleMetal (release hole for Metal)	6		6	
Hole2 (release hole for Poly2)	4		4	
Hole1 (release hole for Poly1)	2		2	

5.1.1 Chip Layout

Several single-cell, 1-D and 2-D array devices were assembled to produce a 4.75 mm × 4.75 mm chip layout. The complete design of the chip is shown in Figure 5.2. There are seven single-cell devices and one small array-type devices at the top of the chip. The 1st device in the top left corner is a single-cell device of M3-CMUT. The next

single-cell device contains a CMUT cell. The effective radii of these devices are 65 µm. The single-cell M3-CMUT devices, the 3rd to the 7th devices from the top-left, have different dimensions than that mentioned in Table 5.1 and thus were characterized in this work. The two M3-CMUT cells in the top right corner, sharing a contact pad, were also not a part of the work presented in this thesis.

In the middle of the chip, two 2-D array ($22 \times 14 = 308$) devices are located. The same M3-CMUT and CMUT cells from the first two single-cell devices were replicated

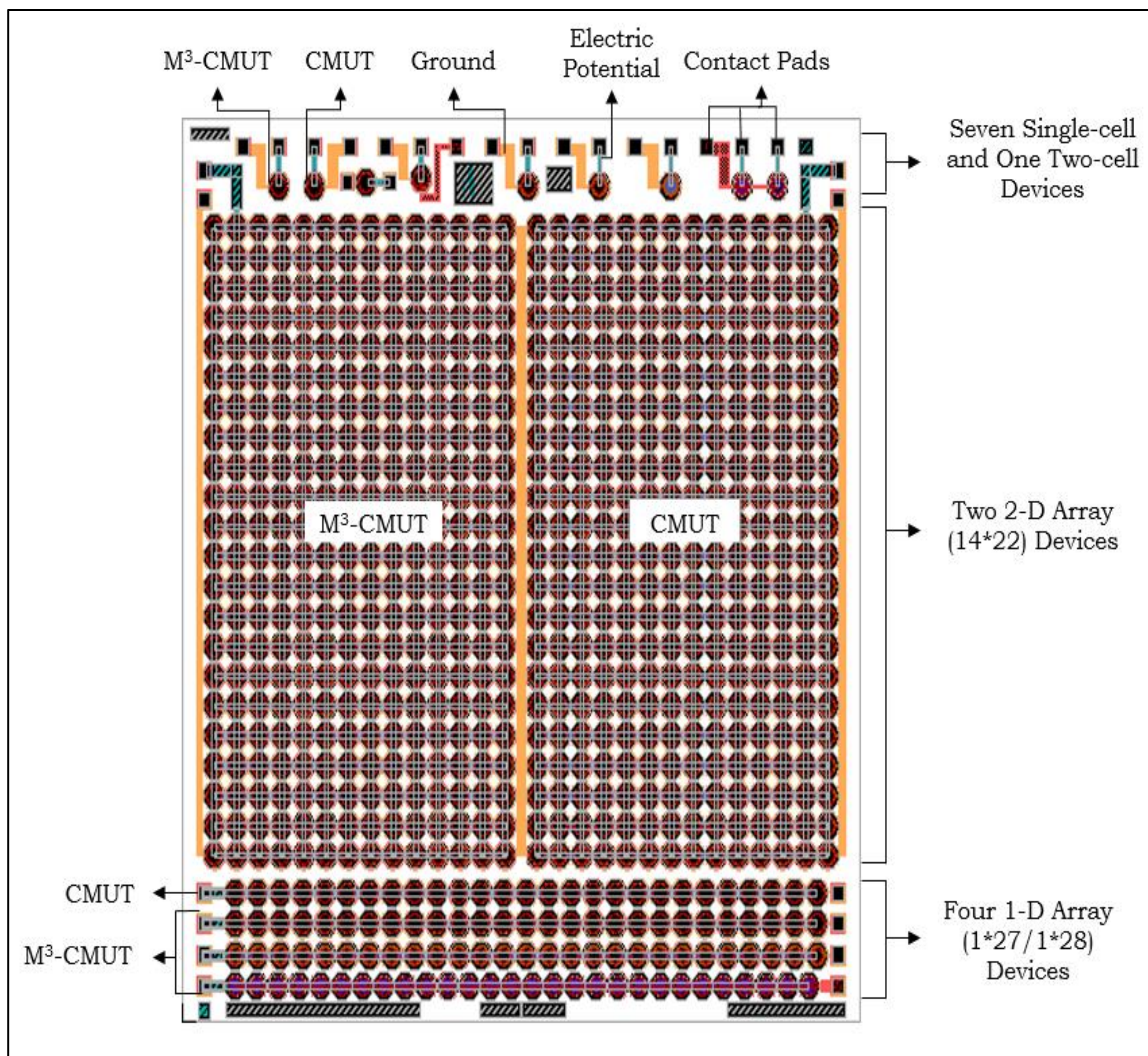

Figure 5.2. Full L-Edit layout of the chip extracted from the MEMS Pro software.

and connected to make the left and the right 2-D array, respectively. These 2-D arrays of 308 devices were connected in parallel via 22 rows and 14 columns.

The 1-D array devices are found in the bottom of the chip. The first array was made of CMUT cells, while the next three arrays were of M^3-CMUT cells of three different dimensions. Twenty-seven (27) individual cells were connected in parallel to make the first three arrays, whereas the last array contained 28 cells. The cells of the 1st and the 2nd array are the same as the single-cell CMUT and M^3-CMUT stated above. The 3rd and the 4th M^3-CMUT array cells are of different sizes and hence were not used in this work.

After finalizing the design, the chip layout was submitted to MEMSCAP, Inc. through CMC Microsystems for fabrication. There are several possible file formats for submitting a design. However, MEMSCAP prefers the Gerber Data Stream Information Interchange (GDSII) format. The chip layout was extracted from L-Edit as a GDSII file, which included the details of the material layers and the 2-D geometries of the CMUT and M^3-CMUT design.

5.2 Fabrication Method

MEMSCAP provided the fabrication of the CMUT and M^3-CMUT design using a Multi-User MEMS Process (MUMPs) called PolyMUMPs. Multi-User MEMS Process (MUMPs) is a well-established, commercial, multi wafer project program from MEMSCAP to manufacture the MEMS design.

5.2.1 PolyMUMPs Process

PolyMUMPs is a seven-layer surface micromachining process consisting of three structural layers of polysilicon, two sacrificial layers of oxide, one insulation layer of nitride and one contact layer of metal [60], as shown in Figure 5.3 (a). Each layer has a

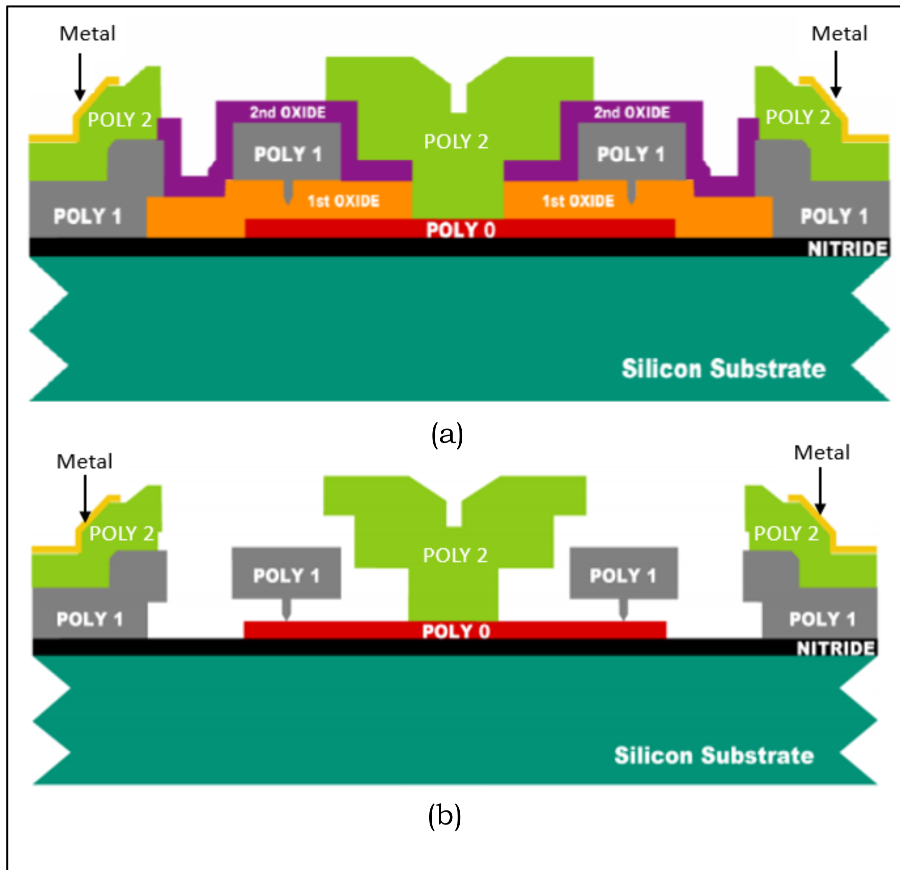

Figure 5.3. PolyMUMPs process (a) before and (b) after the sacrificial layer release [60].

respective lithography (masking) level for patterning the layer. After the depositions and etchings of all the layers, the process ends with the releasing of the sacrificial layer(s) to allow the movement of the relevant parts. There are some release holes created in the structural layers for the release of sacrificial layers. An example of the PolyMUMPs process after the release is shown in Figure 5.3 (b). The details of all of the layering steps can be found in the PolyMUMPs design handbook [60]. The layer names, materials, thicknesses, and lithography (masking) level names used in the PolyMUMPs design of CMUT and M^3-CMUT are presented in Table 5.2. The purpose of each of the lithography levels is given in Table 5.3.

Table 5.2. Layer name, material, thickness, and lithography level name of the PolyMUMPs process [60].

Material Layer	**Material**	**Thickness (μm)**	**Lithography Level**
Substrate	Silicon	-	-
Nitride	Silicon Nitride	0.6 ± 0.07	-
Poly 0	Polysilicon	0.5 ± 0.03	POLY0
First Oxide	Phosphosilicate glass	2 ± 0.25	ANCHOR1
Poly 1	Polysilicon	2 ± 0.15	POLY1 (HOLE1)
Second Oxide	Phosphosilicate glass	0.75 ± 0.08	POLY1_POLY2_VIA
Poly 2	Polysilicon	1.5 ± 0.1	POLY2 (HOLE2)
Metal	Gold	0.52 ± 0.06	METAL (HOLEM)

Table 5.3. Purpose of the lithography (mask) level [60].

Lithography Level	**Purpose**
POLY0	Patterning ground plane
ANCHOR1	Opening holes for Poly 1 to Nitride or Poly 0 connection
POLY1	Patterning Poly 1
POLY1_POLY2_VIA	Opening holes for Poly 1 to Poly 2 connection
POLY2	Patterning Poly 2
METAL	Patterning Metal
HOLE1	Providing release holes for POLY1
HOLE2	Providing release holes for POLY2
HOLEM	Providing release holes for METAL

5.3 Fabrication Process Flow

The fabrication began with a wafer of n-type silicon (100) that had a diameter of 150 mm and a resistivity of 1-2 $\Omega \cdot cm$ [60]. The first step of the process was to highly doped (phosphorus) the silicon wafer. A layer of phosphosilicate glass (PSG) was used as the dopant source. The PSG layer was deposited and then baked at 1000 ℃ in a diffusion furnace. During the bake, the phosphorus from the PSG layer diffused into the silicon, after which the residual PSG layer was removed. This highly doped wafer gives the flexibility for using the wafer itself as a bottom contact. However, in these CMUT and M^3-CMUT designs, substrate contact was not used. A polysilicon layer (Poly 0) was used as the bottom contact for all of the devices studied in this work. A 600 nm thick silicon nitride (Si_3N_4) layer (see Figure 5.4 (a) and Figure 5.5 (a)) was deposited onto the silicon surface using a low-stress low-pressure chemical vapor deposition (LPCVD). This Si_3N_4 layer provides isolation from the substrate.

The first structural layer was a 500 nm thick polysilicon film (Poly 0). It was deposited using the LPCVD process described above, as shown in Figures 5.4 (b) and 5.5 (b) for the CMUT and M^3-CMUT devices, respectively. The Poly 0 film was then patterned using standard photolithography techniques and etched in a reactive ion etch (RIE) system. A second 2.0 μm PSG layer, known as the 'First Oxide', was then deposited by LPCVD to form the first sacrificial layer. This PSG layer was annealed at 1050 ℃ for 1 hour in Argon (Ar). It was then lithographically patterned and etched using RIE to form the Anchor 1 holes for the supporting beams of the second polysilicon film. The first oxide layer was then etched into two different patterns for the CMUT and M^3-CMUT designs. For the CMUT, the patterning shown in Figure 5.4 (c) was done in such a way that the second polysilicon (i.e., Poly 1) layer could be deposited directly on top of the

Poly 0 film. In this way, both the Poly 0 and Poly 1 films could be shorted and used as the fixed bottom electrode. The same sacrificial layer was etched to form the cavity for the middle membrane (i.e., Poly 1) of M^3-CMUT, as shown in Figure 5.5 (c).

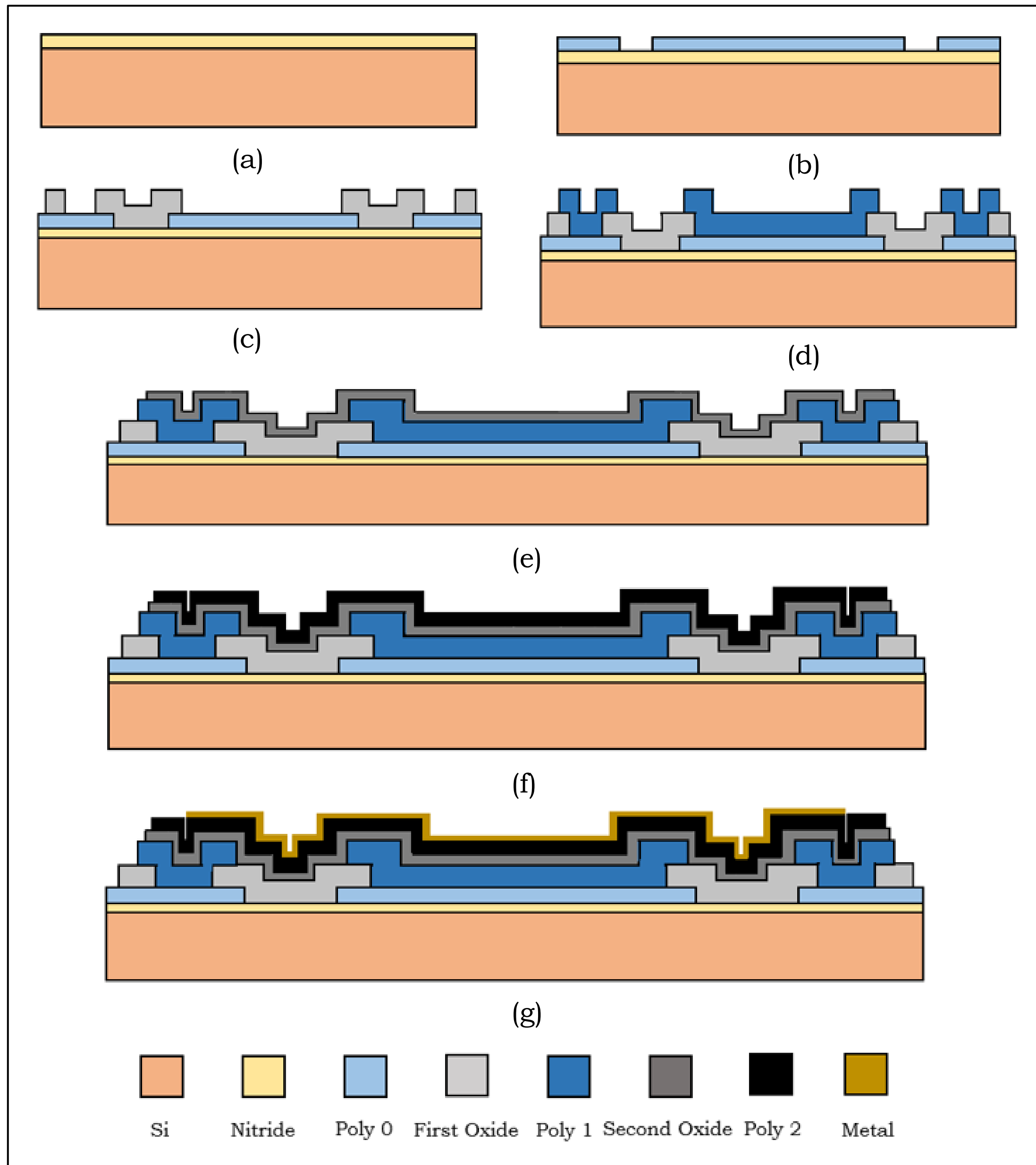

Figure 5.4. Cross-sectional view of the simplified fabrication process of CMUT; deposition and structuring of (a) Nitride, (b) Poly 0, (c) First Oxide, (d) Poly 1, (e) Second Oxide, (f) Poly 2, and (g) Metal layer. Layer heights and radii are not to scale.

The second polysilicon layer (Poly1) was 2.0 µm thick and deposited using the same LPCVD process as that used for the Poly 0 layer. The deposition and patterning of the Poly 1 layer for the CMUT and M3-CMUT devices are shown in Figures 5.4 (d) and

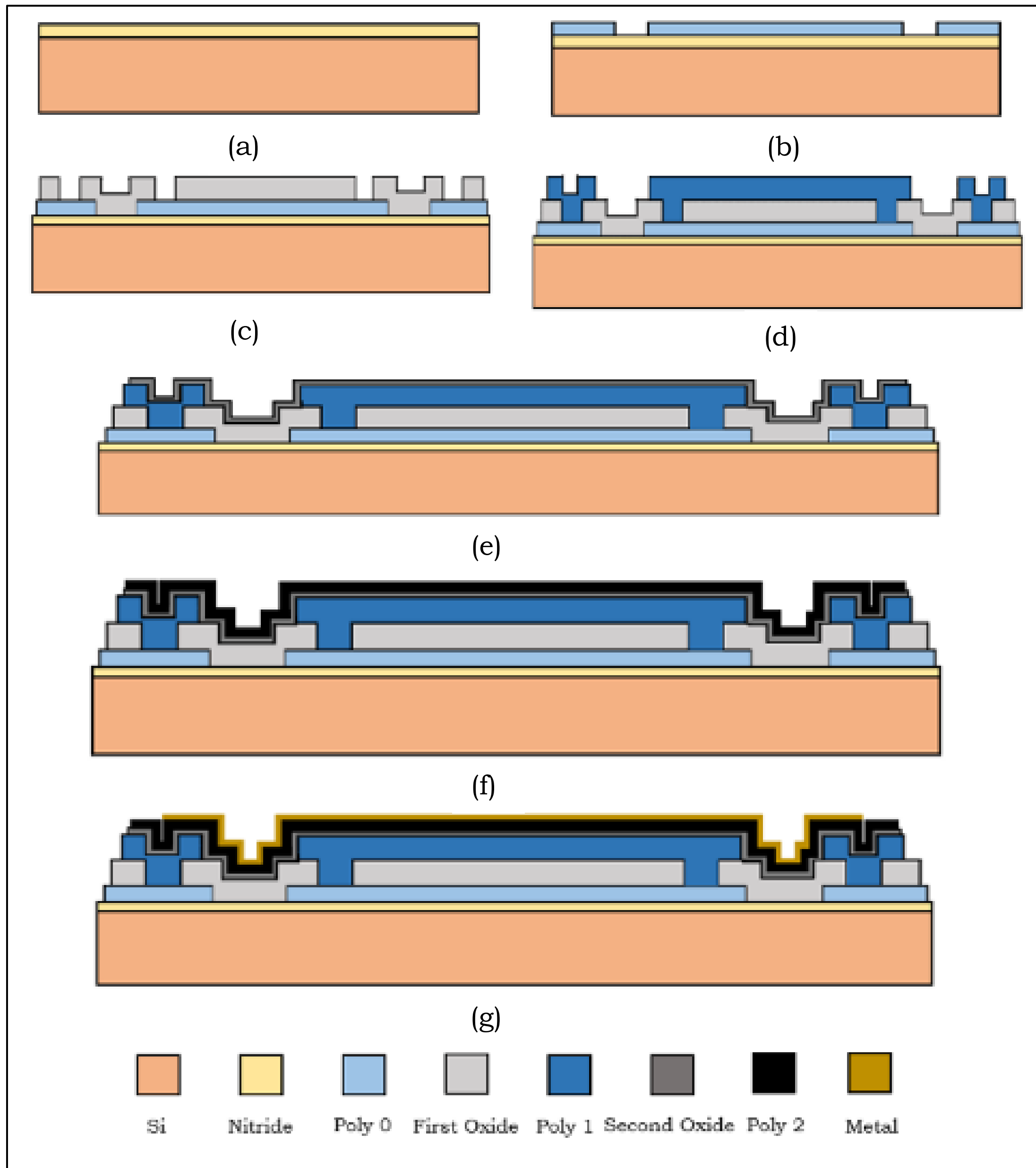

Figure 5.5. Cross-sectional view of the fabrication process of M3-CMUT; deposition and structuring of (a) Nitride, (b) Poly 0, (c) First Oxide, (d) Poly 1, (e) Second Oxide, (f) Poly 2, and (g) Metal layers. Layer heights and radii are not to scale.

5.5 (d), respectively. The patterning of Poly 1 layer was followed by the deposition of another 200 nm PSG layer, which was also annealed at 1050 ℃ for 1 hour. This PSG layer supplied the phosphorus doping and reduced stress in the Poly 1 layer. The PSG and Poly1 layers were also patterned lithographically. The PSG layer was then RIE etched to produce a protective hard mask for Poly 1. It was removed after patterning. A 0.75 μm thick PSG, named 'Second Oxide', was formed by LPCVD, as shown in Figures 5.4 (e) and 5.5 (e) for the CMUT and M^3-CMUT devices, respectively. The second sacrificial layer was patterned. It was then RIE etched to form the Poly1_Poly2_Via holes for the openings of the third polysilicon layer (i.e., Poly 2) to the Poly 1 layer.

The 1.5 μm Poly 2 layer was then deposited for the CMUT and M^3-CMUT devices, as shown in Figures 5.4 (f) and 5.5 (f), respectively. The Poly 2 layer was patterned similarly to that of the Poly 1 layer by using another 200 nm PSG layer as the protective mask. The final film to be deposited in this process was a 0.5 μm metal, as shown in Figures 5.4 (g) and 5.5 (g) for the CMUTs and M^3-CMUTs, respectively. This layer was used to provide electrical contact. The metal layer was patterned using a lift-off process, as described in Section 2.2.3. Finally, the wafer was diced and sorted into individual chips.

The release of sacrificial layers was done by immersing the diced chips in a 49% HF bath at room temperature for 1.5~2 minutes. The bath was followed by rinsing the chips in DI (deionized) water and then alcohol. The rinsing was done to reduce the stiction associated with HF etchant. The chips were then dried at 110 ℃ in an oven for 10 minutes. A photograph of a non-bonded released chip is shown in Figure 5.6 (a). The chips were bonded in the 68 pin ceramic chip carriers (Figure 5.6 (b)). Twenty-five micron (25 μm) Au wires were used to make the connections between the contact pads

of the chip and the pins of the ceramic carrier. The complete wire-bonded chip is illustrated in Figure 5.6 (b).

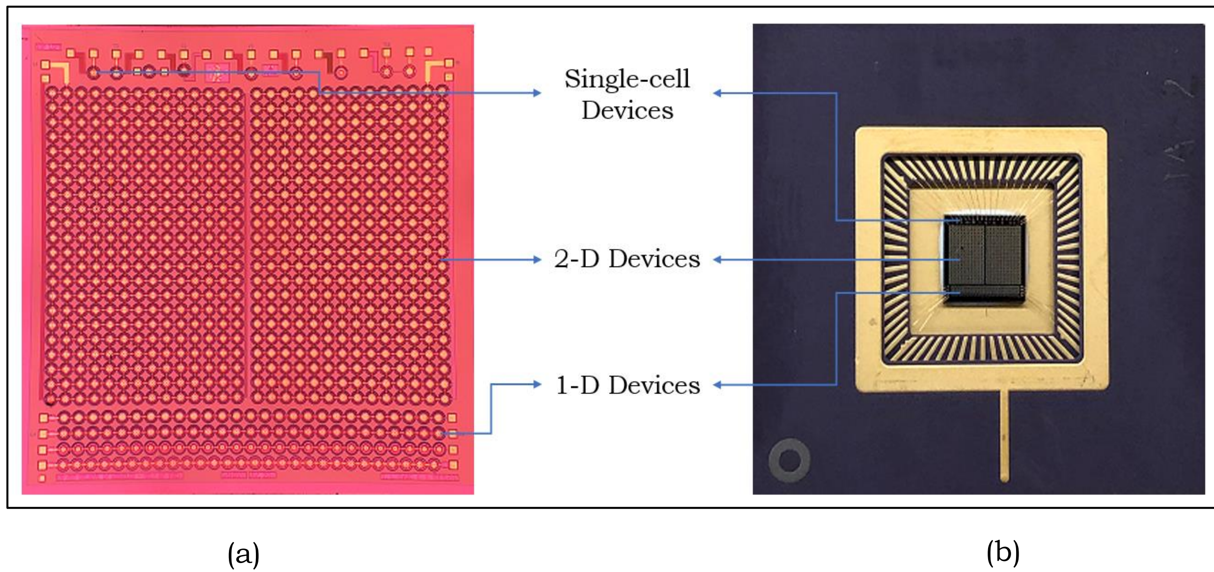

Figure 5.6. Top view of a (a) non-bonded and a (b) bonded chip. The non-bonded chip was enlarged using a scope.

Chapter 6 Electrical Characterization of the CMUT & M^3-CMUT

In this chapter, the electrical characterization of the CMUT and M^3-CMUT ultrasonic transducers is discussed. To understand the basic operating parameters of the transducers, the electrical characterization was used to assess the collapse voltage, the resonant frequency, and the spring softening effect that are different in different device structures.

The electrical impedance is a fundamental property of the fabricated devices and as such, was measured using an Agilent 4294A precision impedance analyzer. This analyzer provided the device impedance as a function of the applied DC bias and bias frequency. The impedance was investigated to determine the resonant frequency of these devices. The applied bias was kept below the “collapse voltage” to ensure the membrane was not shorted to the lower contact rendering the device useless. The “spring softening effect” was assessed from the change in the resonant frequency as a function of the applied bias.

6.1 Electrical Characterization Apparatus

Both the non-bonded chips as well as those chips bonded onto the 68-pin chip carriers were tested electrically. The non-bonded chips were measured in a probe station where electrical contact to the chip was made using tungsten probes. The position of these probes was controlled by micromanipulators. The interior of the probe station, the tungsten probes with a microscope objective and the probes contacting an individual device on the chip are shown in Figure 6.1 (a), (b) and (c), respectively.

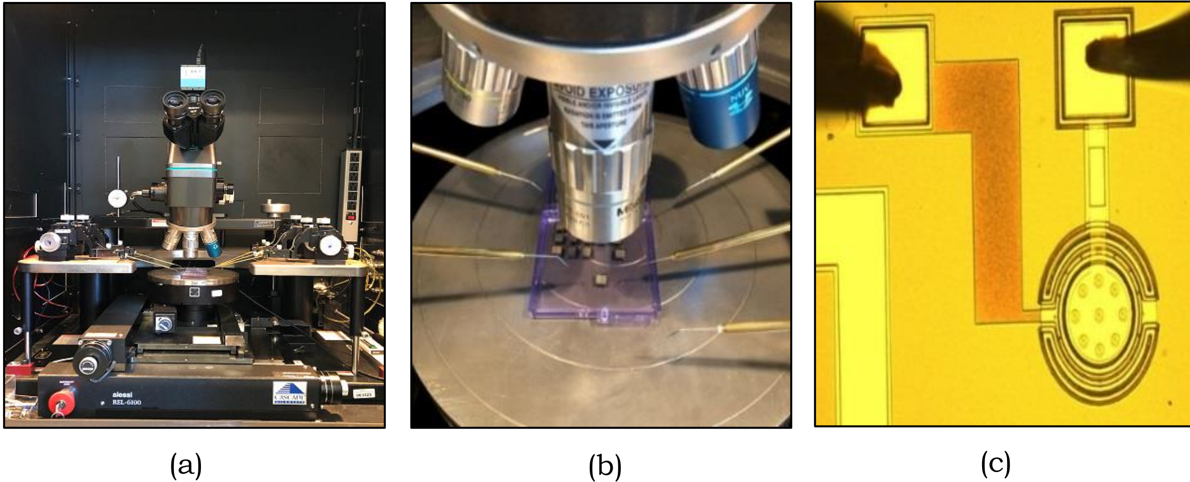

Figure 6.1. The interior of the probe station, (b) the non-bonded chips and the tungsten probes, and (c) two probes contact the membrane and bottom plate connections.

A custom made test fixture (a printed circuit board designed by Daryl Hamelin and Zoran Trajkoski of the University of Manitoba) was used to facilitate the electrical connections of the bonded chips. As the chips were bonded onto 68 pin ceramic carriers, the board was designed in such a way that it could employ separate connections to these pins. A photograph of a bonded chip placed in the test fixture is shown in Figure 6.2. The BNC connectors (top and bottom of the photo) were used to connect the devices to the external measuring equipment.

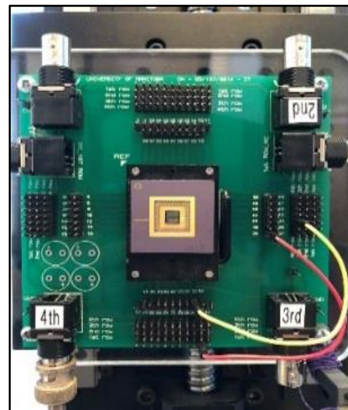

Figure 6.2. Bonded chip in a 68 pin ceramic carrier placed in the test fixture.

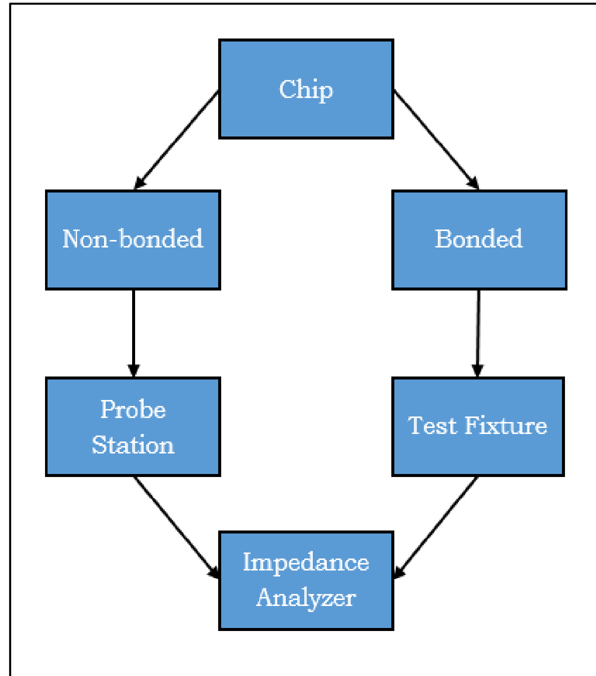

Figure 6.3. Schematic diagram of the electrical measurement apparatus.

Electrical connections from the probes or the test fixture to the external measuring equipment (i.e., the impedance analyzer) were made using BNC cables. In Figure 6.3, a general schematic diagram of the overall measurement system, including the probe station, the test fixture and the electronic measurement equipment is shown.

6.2 Collapse Voltage Measurement

As discussed in Section 3.2.1, when a device is operated at the “collapse voltage” (or greater), the electrostatic force becomes higher than the membrane restoring force. As derived in Equation 3.14, the optimum membrane deflection is less than one-third of the gap height. If the deflection reaches this limit, the membrane becomes unstable and will collapse onto the fixed bottom electrode. Therefore, the collapse voltage of the fabricated device needs to be determined to prevent any such mechanical or electrical damage to the transducer.

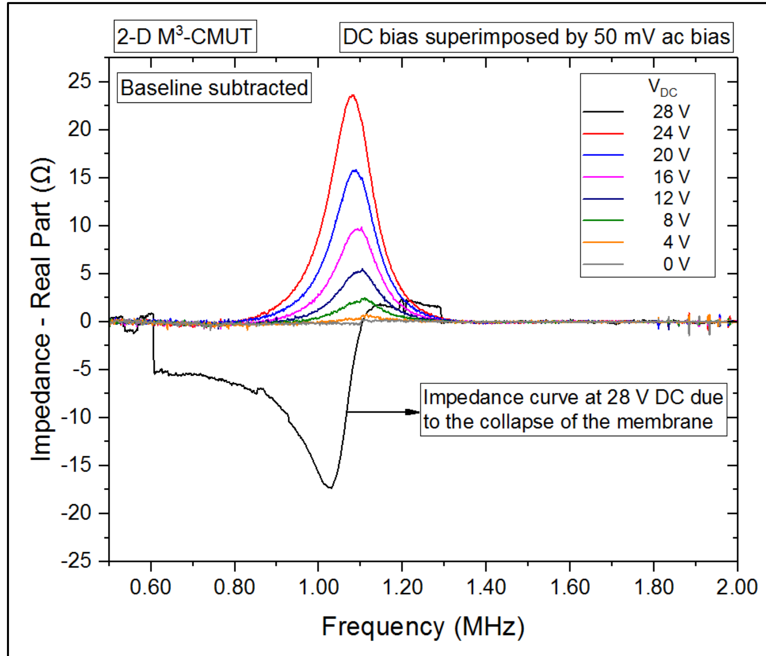

Figure 6.4. Collapse voltage measurement using a 2-D M3-CMUT device.

In Figure 6.4, the impedance curves of a non-bonded 2-D M3-CMUT over a range of different biases are shown. The resonance peak shifted to lower frequencies as the DC bias was increased as a result of the spring softening effect discussed in Section 3.2.2. To measure the collapse voltage, the voltage between the membrane and the bottom electrode was increased until there was an unexpected change in the shape of the impedance curve. As shown in the figure, the curve observed at 28 V shows the impedance when the M3-CMUT membrane reaches to its collapse point. Several other M3-CMUT devices (single cell, 1-D, and 2-D) were measured, and the collapse voltage for all the devices were found to be 28 ± 1 V [58]. Similarly, the collapse voltage of CMUT devices was found to be 33 ± 1 V [58].

It was observed in Section 4.2.1.1 (FEM simulation) that the M3-CMUT had a lower collapse voltage than the CMUT, which echoes with the result of measured collapse voltage in this section. This suggests that the M3-CMUT had a greater

membrane deflection (i.e., a lower effective cavity) and therefore reached to its collapse point at a lower voltage than the CMUT. To ensure proper transducer performance, the operating voltage of the transducers was always chosen to be less than their respective collapse voltage.

6.3 Electrical Impedance Measurement

With the measurement of the electrical impedance, the functionality under different biasing conditions may be determined. This mathematically complex quantity yields the real part and the imaginary part of the device impedance. A DC bias (lower than the collapse voltage of CMUT and M3-CMUT devices) was superimposed onto an ac bias to facilitate the impedance measurement. The impedance analyzer itself supplied both the ac and DC voltages. A typical example of the real and imaginary part of the

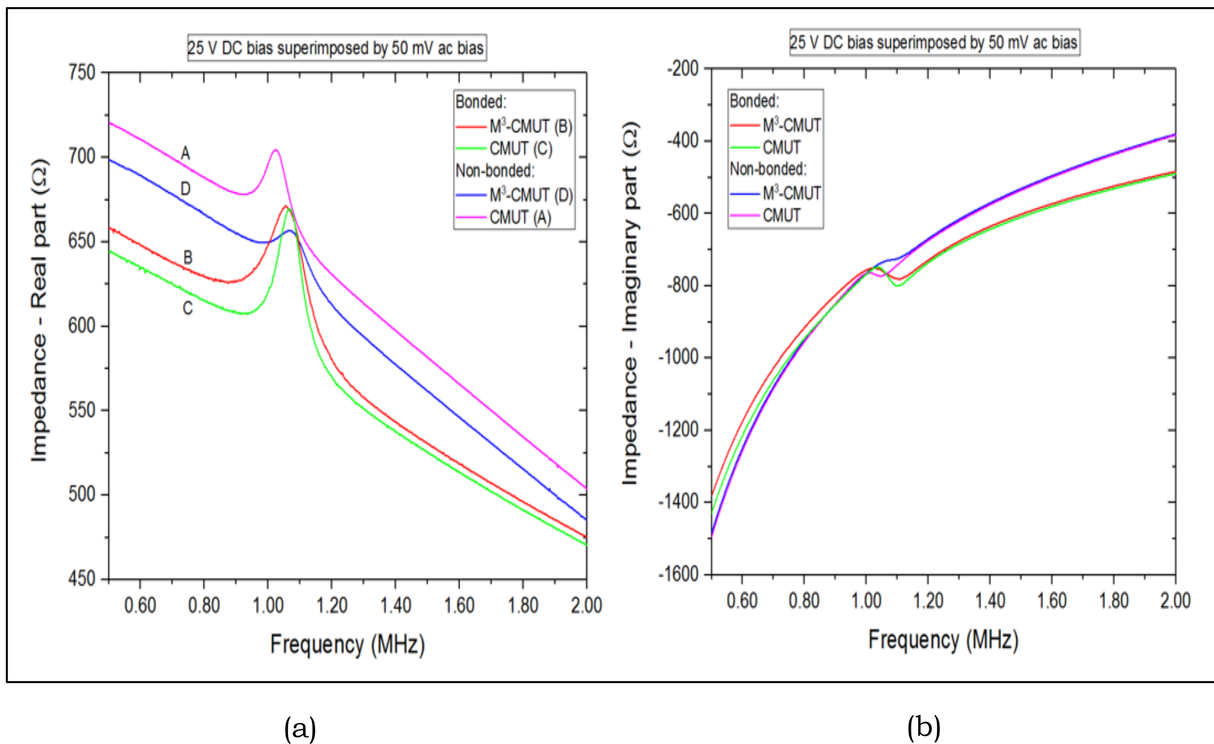

(a) (b)

Figure 6.5. (a) Real and (b) imaginary part impedance curve of the 65 μm radius 2-D CMUT and M3-CMUT device at 25 V DC bias superimposed by a 50 mV ac bias.

measured impedance of a 2-D CMUT and M^3-CMUT device (both non-bonded and bonded) is shown in Figure 6.5.

As seen from the above impedance curves, the non-bonded and bonded device, whether it's real or imaginary, have differences in their impedance and frequency values. The variation is likely due to the fact that the non-bonded device has added impedances from the tungsten probes, whereas the bonded device from the test fixture and the bonding wires. To avoid such differences in the bonded and non-bonded measurements, the final characterization comparisons were done using the bonded devices only. It is also much easier to characterize the bonded transducers when placed in a test fixture.

The transducer behavior of the real and imaginary parts of the impedance can be described by using a simplified circuit model [61] of the electrical measurement setup, as shown in Figure 6.6. Along with the capacitance of these devices, the total impedance includes parasitic elements. Aside from the transducer capacitance (C), the total impedance includes the series resistance (R_s), series inductance (L), and parallel resistance (R_p). The series resistance (R_s) and the series inductance (L) usually occur from the wire and electrode connections, whereas the parallel resistance (R_P) denotes the loss of the dielectric material.

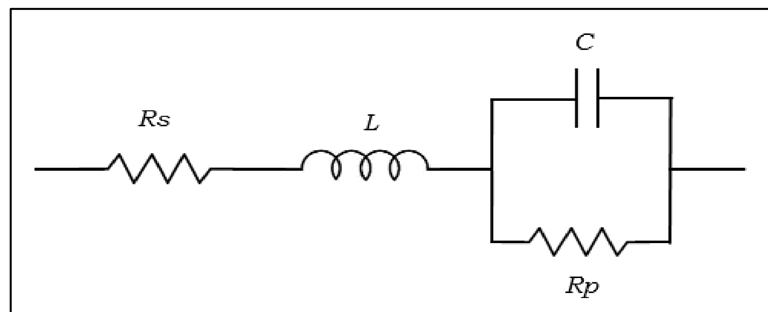

Figure 6.6. Equivalent (RLC) circuit model of the electrical measurement setup of the transducer.

The electrical impedance (Z) of the RLC circuit is given by [61],

$$Z = R_s + \frac{R_p}{1 + \omega^2 {R_p}^2 C^2} + j\frac{\omega L - \omega {R_p}^2 C + \omega^3 {R_p}^2 L C^2}{1 + \omega^2 {R_p}^2 C^2} \qquad 6.1$$

where $R_s + \frac{R_p}{1+\omega^2 {R_p}^2 C^2}$ is the real part and $\frac{\omega L - \omega {R_p}^2 C + \omega^3 {R_p}^2 L C^2}{1+\omega^2 {R_p}^2 C^2}$ is the imaginary part of the impedance. The capacitance (C) and the angular frequency (ω) are also included.

To compare the relative change of the CMUT and M3-CMUT impedance curves as a function of the applied bias, the baseline was subtracted. An illustration of the "baseline subtracted" ($\Delta R = R_{V=\mathrm{DC}} - R_{V=0}$) curve of the same bonded 2-D arrays (used in Figure 6.5) is shown in Figure 6.7. The DC bias was adjusted from 0 V to 25 V using an increment of 2 V.

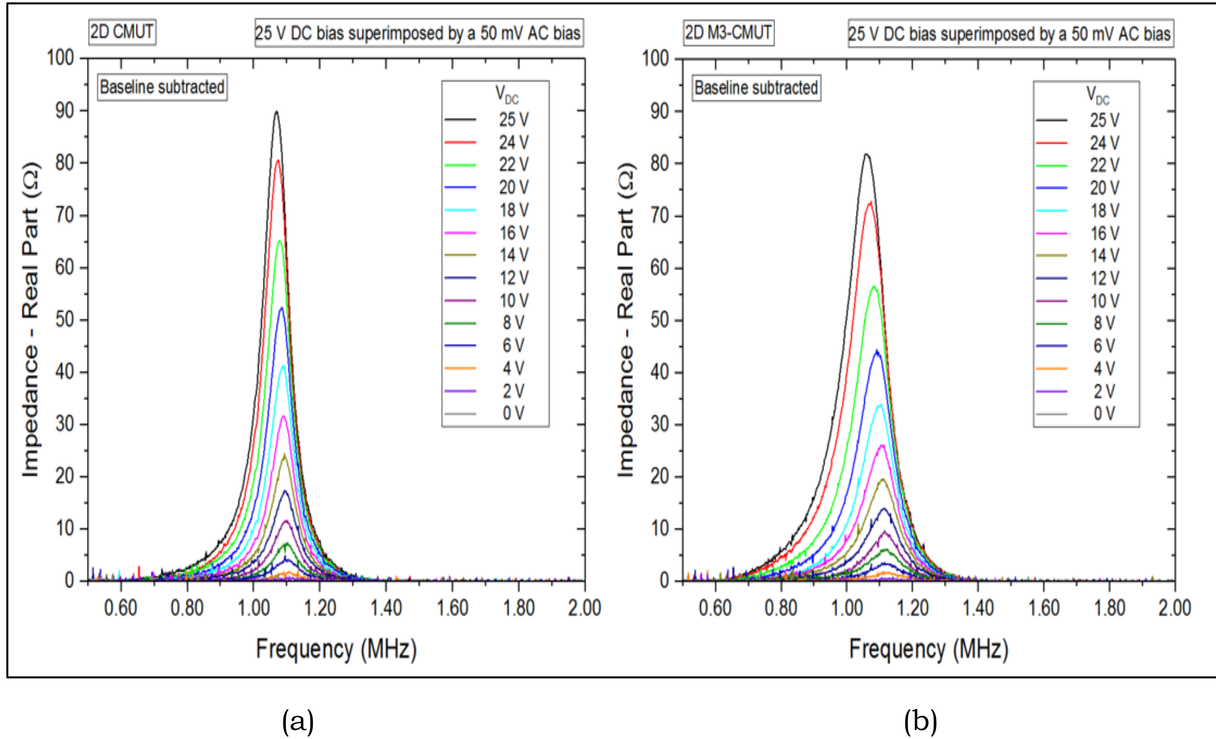

Figure 6.7. Baseline subtracted real part impedance curve of 65 µm radius 2-D (a) CMUT and (b) M3-CMUT device ranging from 0 V to 25 V DC bias superimposed by a 50 mV ac bias.

The analysis of these baseline subtracted curves is presented in the following sections from which the resonant frequency, the spring softening effect, and the peak impedance are determined. They are done for the single-cell, the 1-D and the 2-D arrays of both the bonded CMUT and M^3-CMUT devices.

6.3.1 Resonant Frequency Comparison

The resonant frequency of a given transducer occurs when there is a maximum change in the impedance. After the subtraction of the baseline, as shown in Figure 6.7, the resonant frequency was determined from the change in the real part impedance curve of the single-cell device. The peak impedance of CMUT and M^3-CMUT devices were found at 1.036 MHz and 0.970 MHz, respectively, ($\pm$0.007 MHz) at 25 V DC. The accuracy was determined using the standard deviation of five sets of experimental data of the same device.

The resonant frequency of the 1-D and 2-D arrays at 25 V DC was found to be in good agreement with the single-cell resonant frequency. The measured resonant frequencies of the different device types are presented in Table 6.1. The calculated and the simulated resonant frequency of the single-cell device are also shown.

Table 6.1. Calculated, simulated, and measured resonant frequency comparison of the single-cell, 1-D and 2-D CMUT and M^3-CMUT devices at 25 V DC bias.

Device		**CMUT (MHz)**	**M^3-CMUT (MHz)**
Calculated	Single-cell	1.130	NA
Simulated	Single-cell	0.968	0.964
Measured	Single-cell	1.036 $\pm$ 0.003	0.970 $\pm$ 0.007
	1-D	1.054 $\pm$ 0.002	1.042 $\pm$ 0.005
	2-D	1.068 $\pm$ 0.006	1.055 $\pm$ 0.005

From the FEM simulation discussed in Section 4.2.2.1, it was found that the simulated resonant frequency of M^3-CMUT was less than that of a similarly sized CMUT device. This was confirmed by the measured frequency value of the single-cell devices shown in Table 6.1. The 1-D and 2-D arrays also followed the same trend as the single-cell devices, showing the M^3-CMUT having a lower resonant frequency than the CMUT.

The low resonant frequency of M^3-CMUT in different devices is due to the higher value of the spring softening, which reduces the overall spring constant of the membrane (as in Equation 3.20). This indicates that the M^3-CMUT has higher membrane displacement than the CMUT.

6.3.2 Spring Softening Effect Comparison

As described previously in Section 3.2.2, in the presence of a DC bias, the electrostatic force pulls the top membrane closer to the bottom electrode. The membrane continues to get closer to the bottom electrode with increasing bias. With both ac and DC bias applied, the electrostatic force increases with increasing DC bias. For a given ac bias, a further increase in the DC bias causes the membrane to vibrate even more. Due to this increase in the electrostatic force, the spring constant of the membrane decreases, which in turns shifts the resonant frequency to a lower value. This phenomenon is known as the "spring softening effect".

A DC bias ranging from 0 V to 25 V was applied to measure the spring softening effect in the CMUT and M^3-CMUT devices. In the single-cell devices, the spring softening effect was only measurable above 16 V. As such the frequency response was measured as DC bias was varied from 16 V to 25 V with a step size of 2 V, as shown in Figure 6.8. The error bars in the graph were calculated from the standard deviation of five individual measurements on a single device.

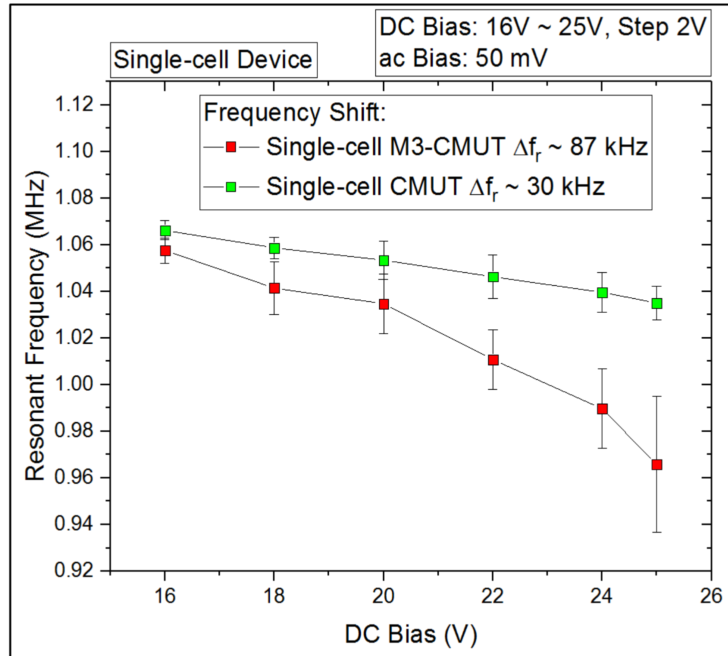

Figure 6.8. Frequency shift due to the spring softening effect of the single-cell CMUT and M3-CMUT (65 µm radius) at a DC bias range of 16 V to 25 V. The DC bias was superimposed by a 50 mV ac bias.

As seen from the figure, the resonant frequency of both single-cell CMUT and M3-CMUT devices show a shift (Δf) to lower frequencies with the increasing DC; as a result of the softening effect. The frequency shift ($\Delta f = f_{V=25\,\mathrm{V}} - f_{V=16\,\mathrm{V}}$) of CMUT and M3-CMUT were measured to be around 30 kHz and 87 kHz, respectively.

The spring softening effects were also observed in the 1-D and 2-D arrays. Due to the large number of devices, and therefore a larger measurement signal, the arrays were measurable at DC biases down to 5 V. Therefore, the applied bias was increased from 6 V to 25 V with an increment of 2 V. The comparison of 1-D and 2-D arrays are given in Figures 6.9 (a) and 6.9 (b), respectively. The results were found to be similar to that of the single-cell device. The M3-CMUT arrays exhibited a more substantial frequency shift ($\Delta f = f_{V=25\,\mathrm{V}} - f_{V=6\,\mathrm{V}}$) relative to the CMUT arrays.

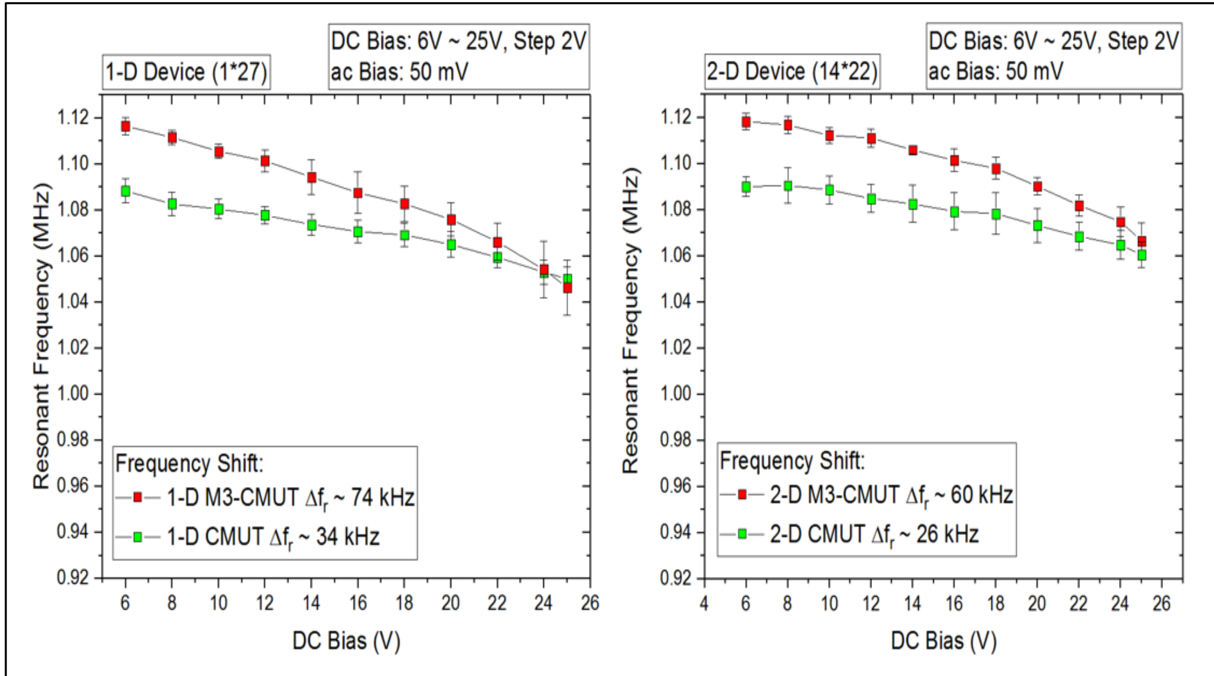

Figure 6.9. Spring softening effect in (a) 1-D and (b) 2-D array devices of CMUT and M^3-CMUT (65 μm radius) ranging from 6 V to 25 V DC bias superimposed by a 50 mV ac bias.

The calculated analytical results and the measured values of the resonant frequency shift as a function of the DC bias are summarized in Table 6.2 for various devices (single-cell, 1-D, and 2-D).

Table 6.2. Calculated and measured resonant frequency shift comparison for single-cell, 1-D, and 2-D devices.

Device		DC Bias Range (V)	CMUT (kHz)	M^3-CMUT (kHz)
Calculated	Single-cell	16~25	28	NA
Measured	Single-cell	16~25	30 ± 7	87 ± 12
Measured	1-D	6~25	34 ± 7	74 ± 5
Measured	2-D	6~25	26 ± 10	60 ± 8

As discussed in Sections 3.2.2 and 4.2.2.2, a greater resonant frequency shift indicates a greater membrane deflection. From Table 6.2, in each type of devices, the M3-CMUT transducer was found to have a greater membrane deflection, compared to a similar CMUT device.

6.3.3 Real Part Impedance Comparison

The real part of the impedance indicates the acoustic power generation capability of a transducer. While measuring the resonant frequency of various devices in the previous section, the peak value of the real part of the impedance was measured. The change in the real part peak impedance (ΔR) of the single-cell CMUT and M3-CMUT as a function of the DC bias is presented in Figure 6.10. The error bars were calculated by the standard deviation of five sets of experimental data on a single device.

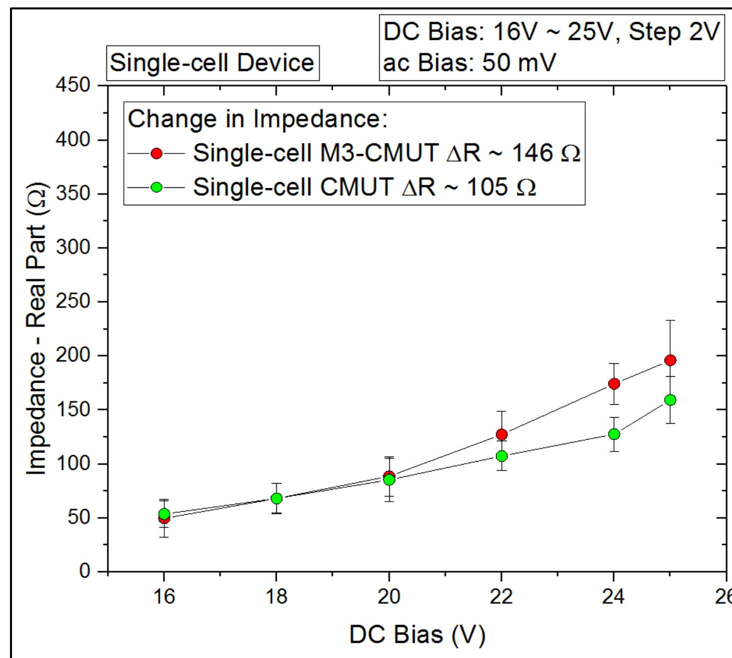

Figure 6.10. Relative change in the real part impedance of 65 μm radius CMUT and M3-CMUT at a DC bias range of 16 V to 25 V. The DC bias was superimposed by a 50 mV ac bias.

As shown in this figure, the change in the impedance increased with the increasing DC bias for both designs. However, the M3-CMUT produced a greater impedance than the CMUT when the applied bias was greater than 20 V. This suggests for a given bias, a greater membrane deflection is obtained in the single-cell M3-CMUT device as opposed to the CMUT device.

From Equation 6.1 in Section 6.3, the real part of the impedance was shown to be a function of capacitance (C). When the DC bias is increased, the membrane deflection increases, and therefore, the capacitance increases. This, in turn, increases the real part of the impedance. Therefore, the higher membrane deflection results in a higher real part of the impedance, which is seen in the single-cell M3-CMUT.

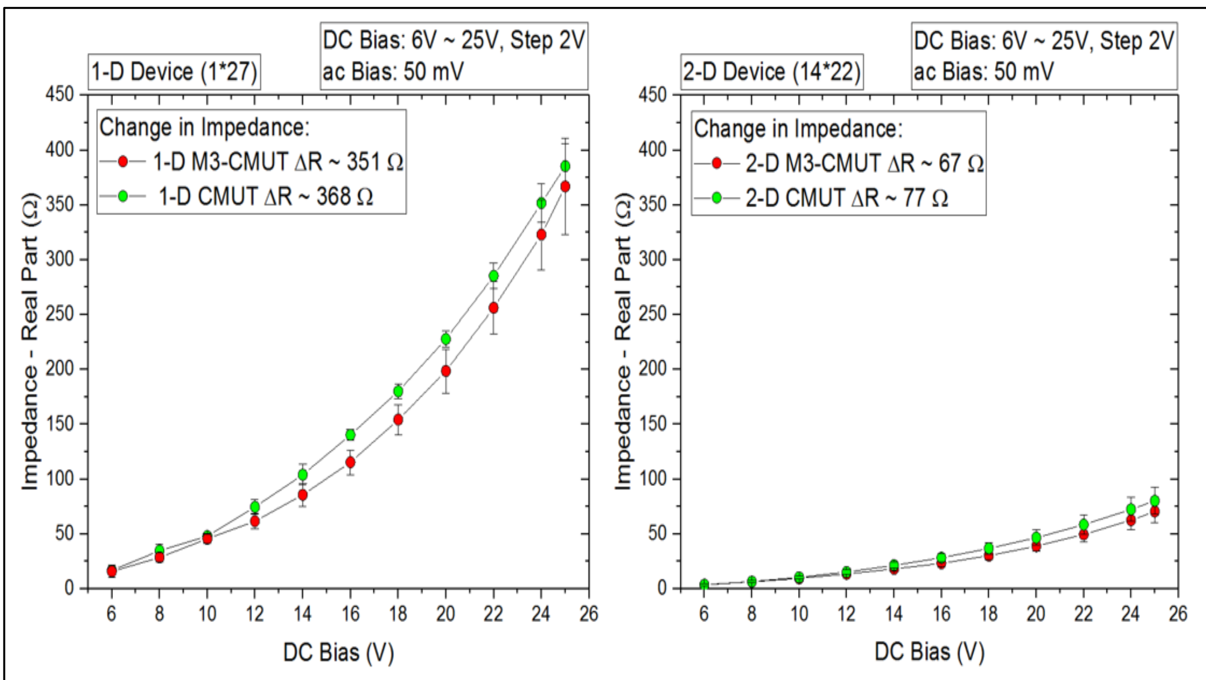

(a) (b)

Figure 6.11. Relative change in the real part impedance of (a) 1-D and (b) 2-D array device of CMUT and M3-CMUT (65 μm radius) from 6 V to 25 V DC bias superimposed by a 50 mV ac bias.

The resonant frequency shifts of the 1-D (Figure 6.11 (a)) and 2-D (Figure 6.11 (b)) arrays of CMUT and M^3-CMUT were compared as well. However, the results were different from single-cell devices. It was observed that the CMUT arrays exhibited a bigger change in the real part of the impedance than the M^3-CMUT.

The differences between single-cell and arrays might be due to the different parasitic elements, particularly since the wiring paths are different (see Figure 5.2). Moreover, in the test fixture, the wiring is also different for the different pin connections, which may add parasitic elements to the overall capacitance of the system.

Chapter 7 Acoustic Characterization of the CMUT & M^3-CMUT

The transducer transmission and reception properties of the acoustic pressure waves either produced (transmitted) or received were determined through acoustic characterization. These properties include the attenuation and the velocity of the transmitted acoustic waves. In this chapter, the acoustic characterization of the fabricated CMUT and M^3-CMUT transducers is presented.

Pitch-catch experiment was performed to enable a comparison of the acoustic properties of the transducers in the air medium. The 2-D arrays of CMUT and M^3-CMUT were used for different analysis since a relatively high acoustic power is required in the air-coupled experimental setup. The setup was built in the Microelectronics and Nanotechnology Research Lab at the University of Manitoba. As the name suggests, one transducer was used to 'pitch' (transmit) an acoustic signal while a second one was used to 'catch' (receive) it. A commercially available transducer was used as a reference to determine the transmission and reception capability of the fabricated transducers. The transducers were investigated in both the transmitter and the receiver modes with the appropriately applied bias and acoustic frequency.

7.1 Pitch-Catch Apparatus

The acoustic characterization used in this work contained many different pieces of equipment, including a commercial CAP5 transducer which was used as the reference transducer as mentioned above. The CAP5 is an air-coupled capacitive transducer from VN Instruments with an operating frequency from 150 kHz to 1.3 MHz. The same test fixture used in the electrical characterization was used to mount the bonded chips containing the 2-D CMUT and M^3-CMUT transducers. An XYZ positioner was used to support the test fixture holding the chip. The movements of the positioner along its X,

Y, and Z axes were regulated by an external controller. The CAP5 transducer was held by an Opti-Claw mount (a self-centering variable size lens mount from Newport) and placed in front of the XYZ positioner. The overall setup was placed on an air table to reduce the physical vibration during the measurements. The experimental setup, shown in Figure 7.1, illustrates a side view of the CAP5 transducer mounted on the opti-claws, and the XYZ positioner containing a bonded chip in the test fixture.

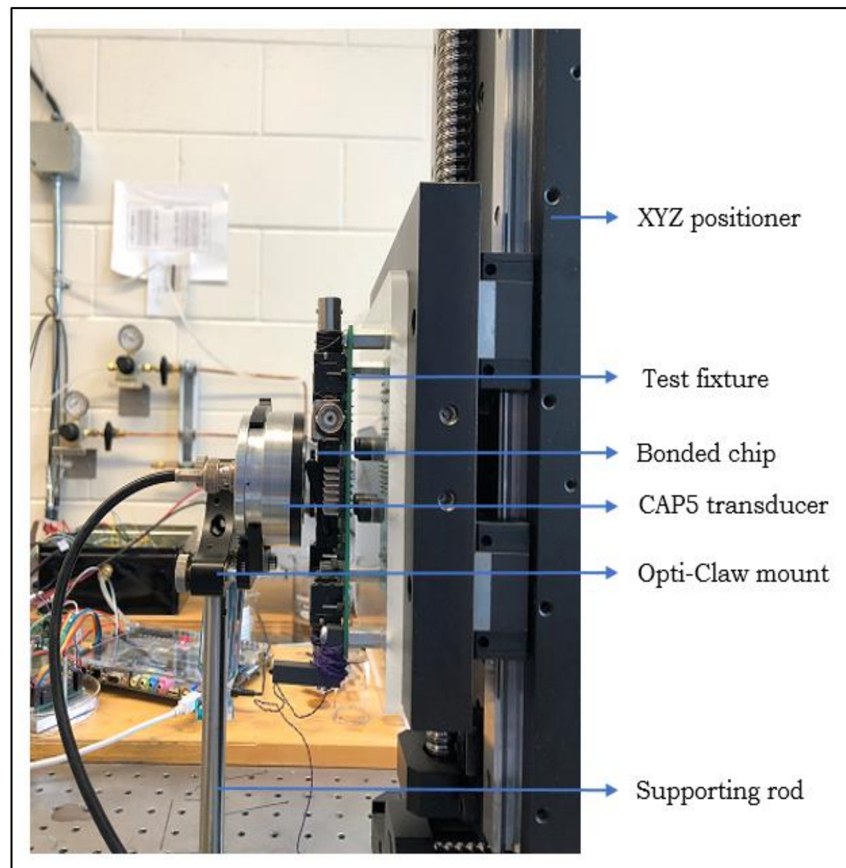

Figure 7.1. Experimental setup of the pitch-catch apparatus.

The following transducer configurations were investigated using this experimental setup.

1. Setup-1: CAP5 as a transmitter and CMUT/M^3-CMUT as a receiver

2. Setup-2: CAP5 as a receiver and CMUT/M^3-CMUT as a transmitter

3. Setup-3: CMUT/M3-CMUT as a transmitter and CMUT/M3-CMUT as a receiver

In "Setup-3", a second test fixture was used in the place of the Opti-Claw mount (i.e., the transmitter side) to hold the bonded chips.

To facilitate the CAP5 transducer as a transmitter or a receiver in the above-mentioned setups, several pieces of equipment from VN Instruments were used. As explained in detail below, these included a remote module, an SIA-7 unit, and a control hub, as shown in Figure 7.2. The remote module was used to alter the mode (i.e., transmission or reception) of the CAP5. When CAP5 was used as a transmitter, the SIA-7 unit provided the pre-amplified signal to generate the acoustic waves. The maximum

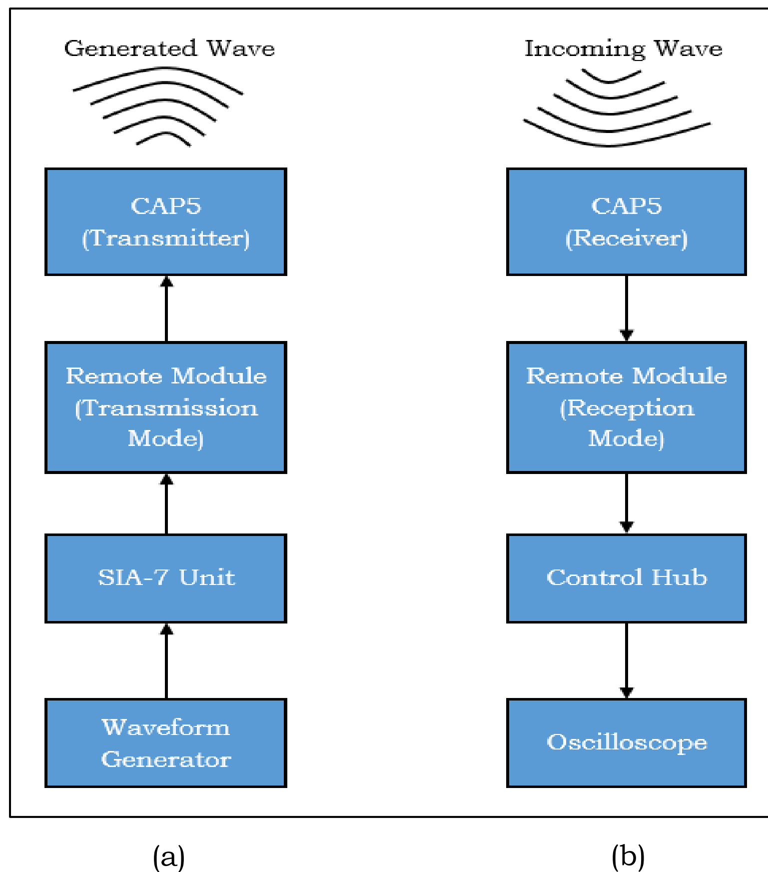

(a) (b)

Figure 7.2. Schematic connection diagram of the CAP5 transducer in the (a) transmitting and the (b) receiving mode.

input voltage to the unit was limited to ±3 V which was provided by a waveform generator (i.e., Agilent 3320A arbitrary waveform generator). In the receiving mode, the control hub was used to regulate the power and gain (dB) of the remote module. The amplified received signals from hub were recorded by an oscilloscope (i.e., DSO-X 3014A). In Figure 7.2, a schematic diagram of the connections between the aforementioned measurement equipment is shown.

The CMUT and M³-CMUT transducers were also provided with a separate bias for their connection as the transmitter and the receiver. As discussed in Sections 2.4 and

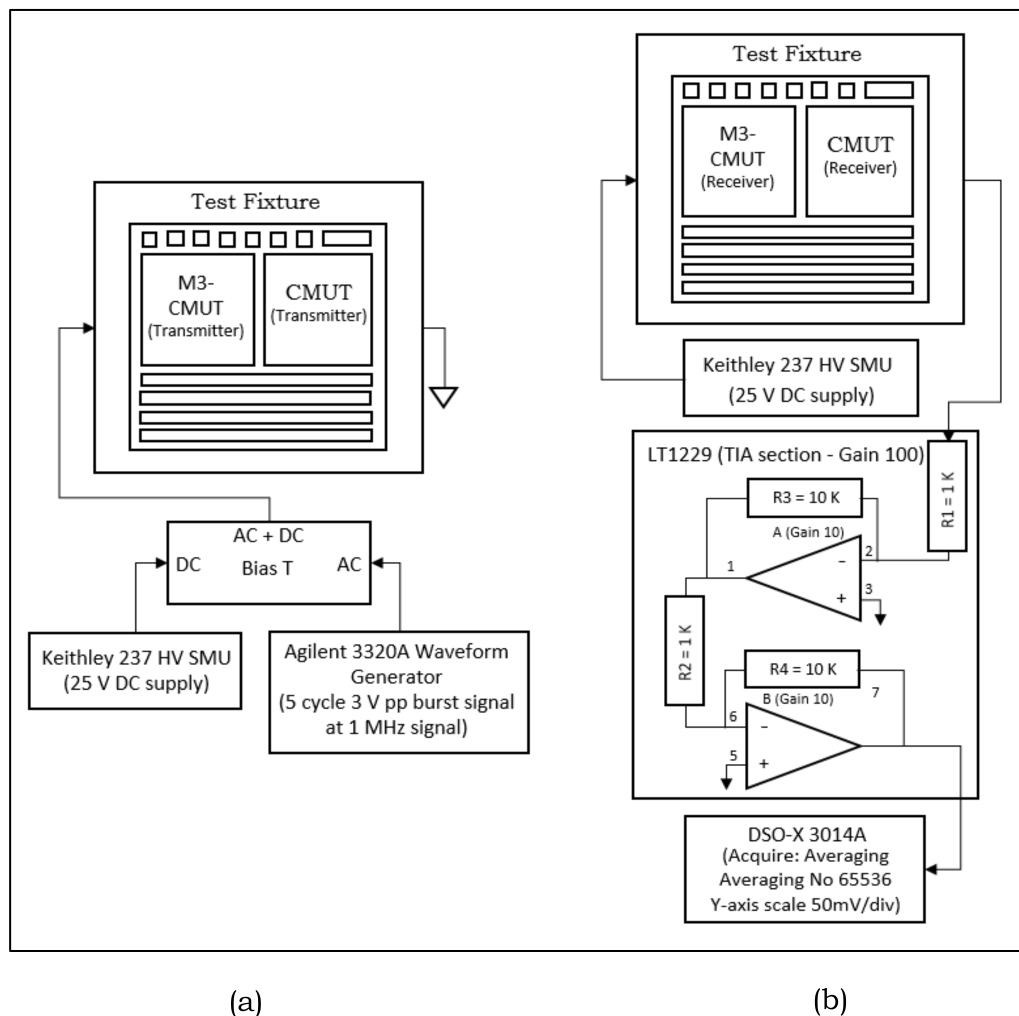

Figure 7.3. Schematic connection diagram of the CMUT and M³-CMUT transducer in the (a) transmitting and the (b) receiving mode.

2.4.1, in transmitting mode, the transducers require both the DC and ac bias to operate. Hence, the transmitters were given input bias of 25 V DC which was superimposed with a 5 cycle 3 V_{pp} sinusoidal burst signal at 1 MHz frequency. The ac signal frequency was chosen to be as close as possible to the transducers resonant frequency (i.e., 1.055 MHz for M^3-CMUT and 1.068 MHz for CMUT). A custom made “Bias-T” was used to mix the ac and DC signals.

When in receive mode, only a DC bias was required to measure the incoming acoustic waves. A 25 V DC bias was applied to the transducers. The output of the receiver was connected to a PCB integrated transimpedance amplifier (TIA) circuit (designed by Daryl Hamelin and Zoran Trajkoski). The amplifier (LT1229) [62] was a 100 MHz dual current feedback amplifier and was used for the amplification of received signals. The amplified output was recorded by an oscilloscope and then transferred to a PC for further analysis. A schematic diagram of the transducers biasing configuration in transmitting and receiving mode is shown in Figure 7.3.

7.2 Acoustic Measurement

7.2.1 Wave Attenuation

Attenuation is the reduction of signal amplitudes over the distance an acoustic wave travels. Using “Setup-1”, the attenuation of transmitted signals was demonstrated. The distance between the transmitter (in this case a CAP5) and the CMUT or M^3-CMUT receiver was increased from ~1 cm to ~1.6 cm, while the amplitude of the received signals was measured. The transient response of a detected signal is shown in Figure 7.4.

The signal amplitude decreased due to the attenuation in a specific distance. For example, the signal received by a 2-D CMUT at a distance of ~1 cm was found to be

around 442 mV, which was reduced to around 378 mV at ~1.6 cm, as illustrated in Figure 7.4 (a). Similarly, in Figure 7.4 (b), a 2-D M^3-CMUT was able to detect an attenuated signal of ~283 mV (~1.6 cm) compared to its initial amplitude of ~324 mV (~1 cm). The rate of decay of the signal is described more in the following attenuation coefficient section.

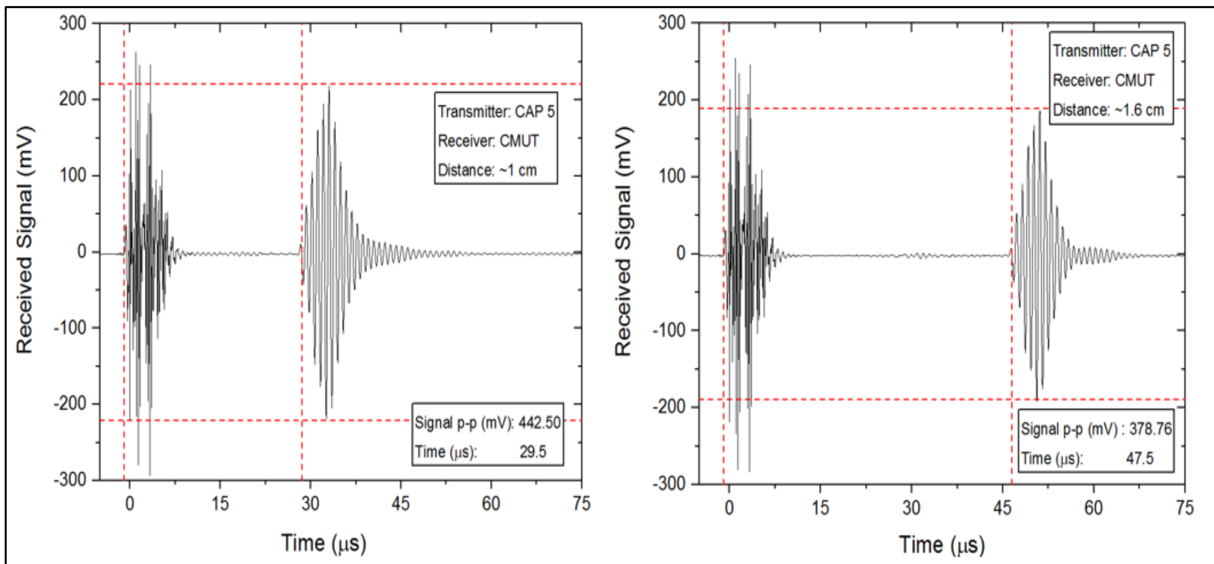

(a)

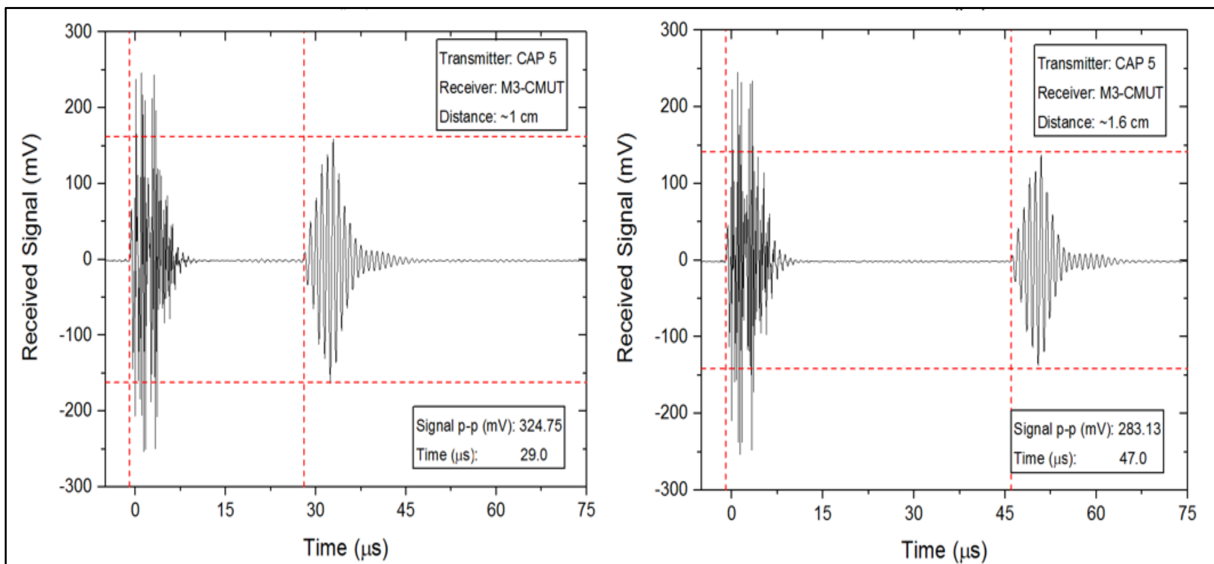

(b)

Figure 7.4. Attenuation of the transmitted signals from the CAP5 transducer in air medium; received by the (a) CMUT and (b) M^3-CMUT transducer at distances of ~1 cm and ~1.6 cm.

7.2.1.1 Attenuation Coefficient

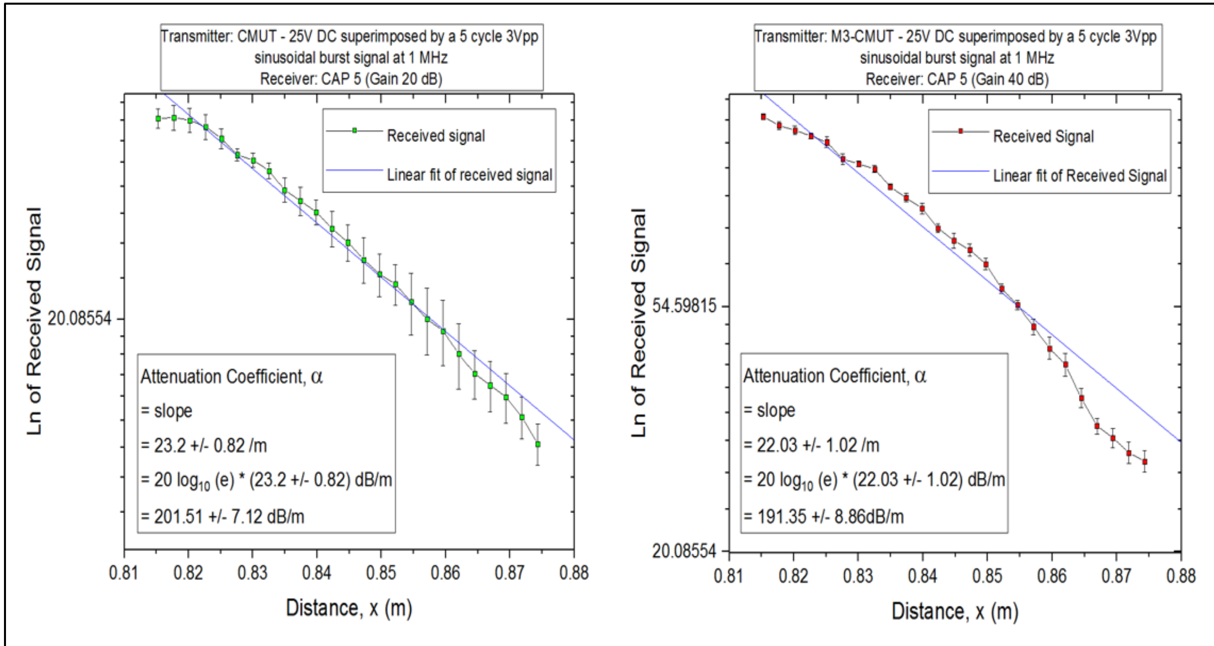

(a)

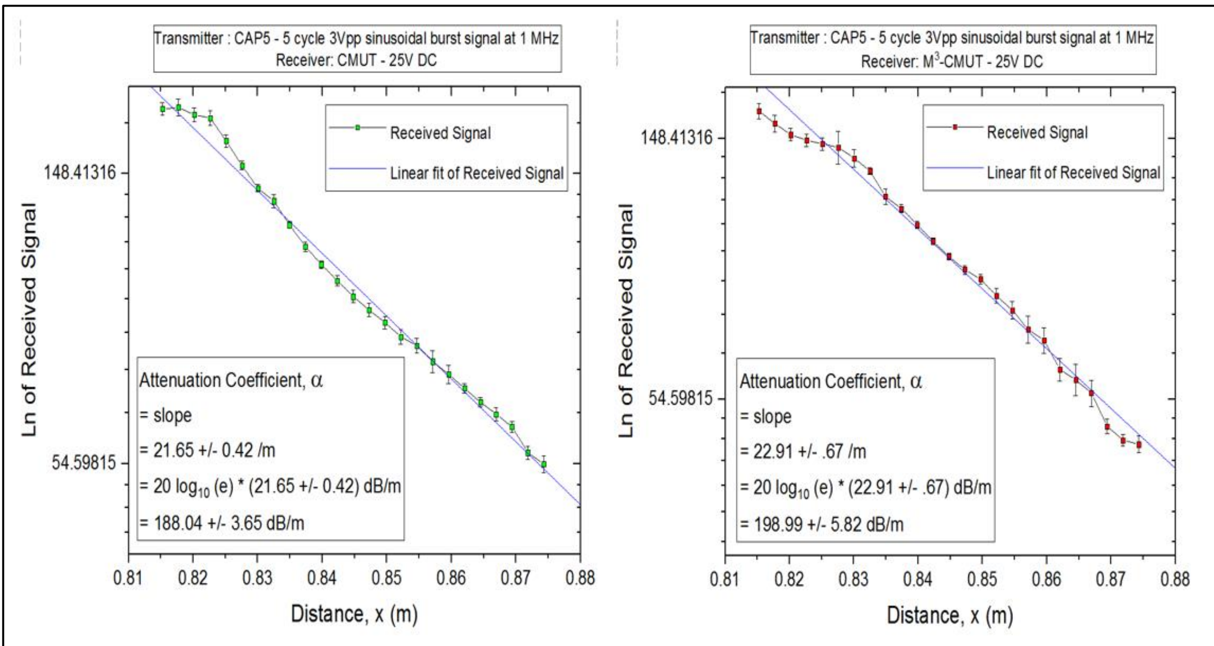

(b)

Figure 7.5. Attenuation coefficient measurement in air medium when the CMUT/M^3-CMUT was used as the (a) transmitter and the (b) receiver at a distance of ~1 cm from the CAP5 transducer.

The attenuation coefficient (α) gives the rate of decrease of the amplitude of an acoustic pressure wave. To measure the attenuation coefficient, "Setup-1" (a CAP5 as the transmitter and either a CMUT or an M^3-CMUT as the receiver) or "Setup-2" (a CAP5 as the receiver and either a CMUT or an M^3-CMUT as the transmitter) was used. The amplified signals were measured from the receiver over a range of distances using the XYZ controller. The data from these measurements are presented in this section.

As shown in Figure 7.5, the natural logarithm of the signal amplitude is plotted as a function of the distance between transmitter and receiver. The error bars were the standard deviation of five sets of the measured data. A "linear fit" curve was plotted to find the slope from which the coefficient was calculated for each case. All of the measured attenuation coefficients were found to be in the range between $\sim 190\ \mathrm{dB.m^{-1}}$ to $\sim 200\ \mathrm{dB.m^{-1}}$.

Using Stoke's law, Equation 2.8 from Section 2.1.3, the attenuation coefficient was calculated to be $9.89\ \mathrm{Np.m^{-1}}$ or $85.7\ \mathrm{dB.m^{-1}}$. The parameters used for the calculation are presented in Table 7.1 [63].

Table 7.1. Parameters used for the theoretical value of attenuation coefficient [63].

Parameter	**Symbol**	**Value**	**Unit**
Frequency	f	1.0	MHz
Dynamic Viscosity of air at room temperature	η	1.825×10^{-5}	$\mathrm{kg.m^{-1}.s^{-1}}$
Density of air	ρ	1.204	$\mathrm{kg.m^{-3}}$
Sound velocity at room temperature	v	343	$\mathrm{m.s^{-1}}$
Room temperature	T	20	℃

There may be several reasons that could account for the discrepancy between the theoretical and the measured values of the attenuation coefficient. Stoke's law considers

the medium to be an isotropic and homogeneous Newtonian medium for the sound propagation [25], which may not be applicable for the air medium. Moreover, the dynamic viscosity of air can be changed with humidity and room temperature [63].

A standard solution (ISO 9613) offers a method to calculate the absorption of sound in a given atmosphere [64]. According to ISO 9613, for a 1 MHz frequency, at 20 ℃, a pressure of 101.325 kPa, and 60% relative humidity, the attenuation coefficient in air is $\sim 200\ dB.m^{-1}$. As shown in the respective graph's inset in Figure 7.5, the attenuation coefficients were found to be in good agreement ($< \pm 5\%$) with the ISO standard value.

7.2.2 The Velocity of Acoustic Waves

The typical velocity of sound waves in air is $343 \pm 12\ \mathrm{m.s^{-1}}$ at room temperature (20 ℃) and 60% relative humidity [65]. The value of the wave velocity can be measured

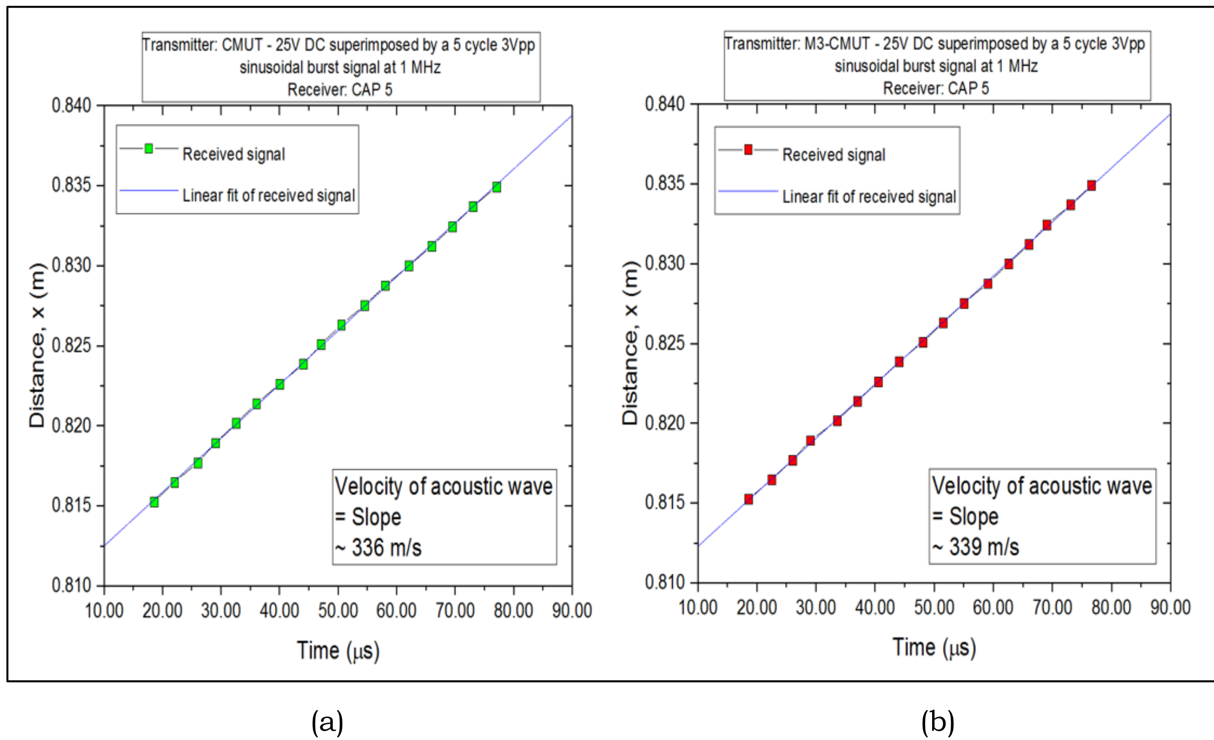

(a) (b)

Figure 7.6. Acoustic wave velocity measurement of the transmitted signals from the (a) CMUT and (b) M^3-CMUT; received by the CAP5 transducer at a distance of ~1 cm.

using a transducer to generate (transmitter) a signal and another to receive it (receiver) over a range of separation. The slope from a time-distance curve can be used to extract the sound velocity. The measurements were found to be consistent with theoretical values with less than 3% variation with the typical value of the acoustic wave velocity ($343\ \mathrm{m.s^{-1}}$). For example, the velocity measurement using "Setup-2" where the fabricated transducers (CMUT or M^3-CMUT) were used as the transmitter and CAP5 was the receiver, is shown in Figure 7.8. The velocity of the transmitted sound waves from CMUT (Figure 7.6 (a)) and M^3-CMUT (Figure 7.6 (b)) was measured to be $337 \pm 4\ \mathrm{m.s^{-1}}$. The error was calculated from the standard deviation of five sets of the measured data of both designs.

7.3 DC Bias and Frequency Dependence of the Acoustic Waves

To analyze the DC bias and frequency dependence of the acoustic waves of fabricated transducers, "Setup-3" was used, where the CMUT and M^3-CMUT transducers were used as both the transmitter and the receiver. The transmitter was around $1\ \mathrm{cm}$ from the receiver for the measurements in this section.

7.3.1 DC Bias Dependence of the Acoustic Waves

Increasing the DC bias increases the output signal intensity. To investigate this, two biasing conditions of the transducers were used. In the first biasing condition, the applied DC bias to the transmitter was varied from $1\ \mathrm{V}$ to $25\ \mathrm{V}$ with an increment of $2\ \mathrm{V}$ while the receiver was kept at a constant bias of $25\ \mathrm{V}$. The received signal as a function of DC bias is shown in Figure 7.7 (a). In the second measurement condition, the transmitter bias was kept constant, and the receiver bias was changed. This measured response is plotted in Figure 7.7 (b). In both cases, the duo of CMUT array has generated

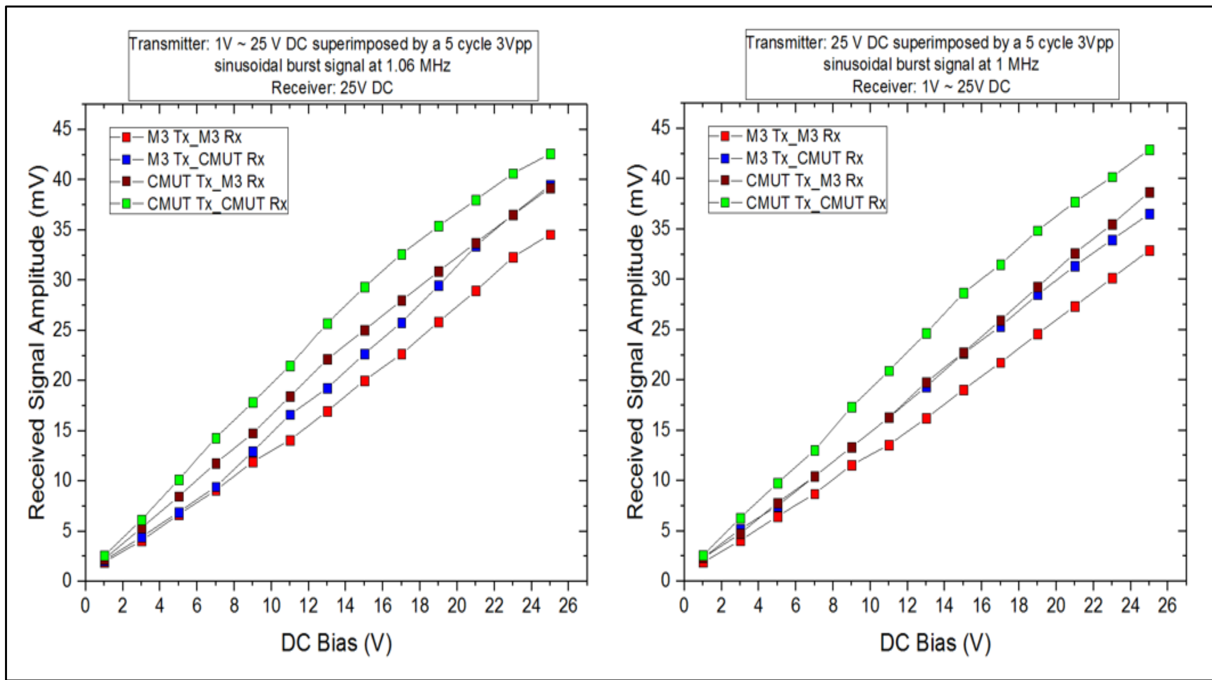

(a) (b)

Figure 7.7. DC bias dependence of CMUTs and M3-CMUTs at the (a) transmitter and the (b) receiver side at a distance of ~1 cm.

the highest acoustic signal than the rest. The probable reason is due to the variance of added parasitic elements in the array devices (see Section 6.3.3).

As discussed in Section 3.3.1, there is a trade-off between the sensitivity and the output power of a transducer. High power transducers require larger cavity heights, allowing for a larger membrane deflection. However, (see Equation 3.43), more sensitive transducers can be made with a smaller cavity height. This allows a larger change in the resonant frequency as well as the capacitance for even a small deflection of the membrane. In Section 6.2, it was reported that the collapse voltage was higher for the CMUT compared to the M^3-CMUT. This higher breakdown voltage allowed the CMUT to be operated at a larger bias voltage, improved its output power than the M^3-CMUT, which is seen in the above figure (7.7).

7.3.2 Frequency Dependence of the Acoustic Waves

In this section, the acoustic signal response of the transducers is reported as a function of the frequency of the transmitted signal. The frequency range was chosen to be centered on the resonant frequency (~1.06 MHz) for the 2-D arrays as discussed in Section 6.3.1. A 3 V_{pp} ac bias with a frequency between 0.6 MHz and 1.5 MHz was superimposed onto the 25 V DC bias and applied to the transmitter. The DC bias was kept constant at 25 V at the receiver.

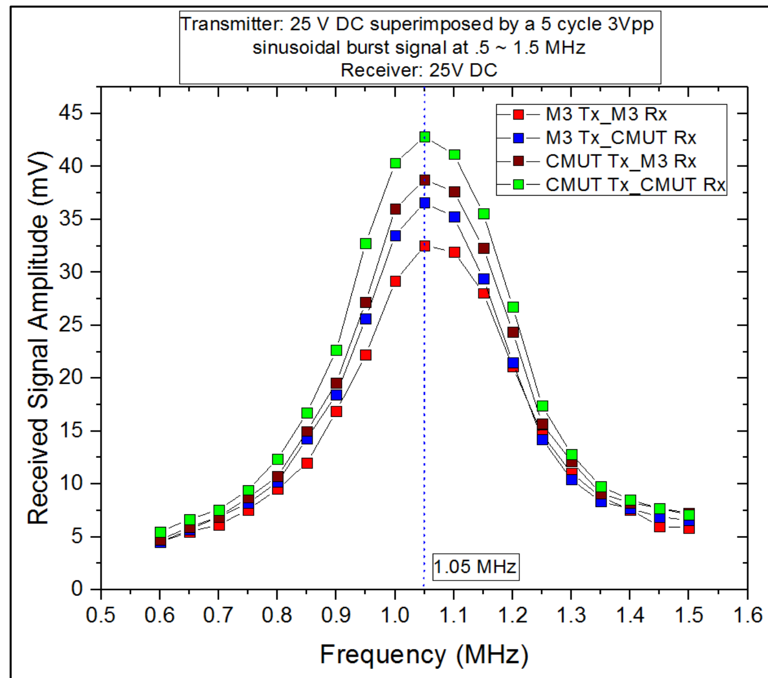

Figure 7.8. Frequency dependence of CMUTs and M^3-CMUTs at a distance of ~1 cm.

The measured signal as a function of frequency is shown in Figure 7.8. The highest signal amplitude is found at 1.05 MHz frequency for each of the settings. This agrees well with the resonant frequency obtained from the impedance measurement of the very 2-D devices.

Chapter 8 Conclusion

8.1 Summary

An analytical model of CMUT was used to describe the static and dynamic properties of several ultrasonic transducers. The newly developed M^3-CMUT was compared to the conventional CMUT using the FEM models of similar dimensions which were modeled using the COMSOL Multiphysics software. Several single-cell, 1-D and 2-D array devices of the M^3-CMUT and CMUT transducers were fabricated using the PolyMUMPs fabrication technology. Electrical and acoustic characterizations were performed to measure the properties of these transducers.

In the case of the single-cell devices, the collapse voltage was found to be lower in M^3-CMUT, which means a greater membrane displacement was achieved at a lower bias. The shift in the resonant frequency as a function of DC bias was detected to be smaller in the M^3-CMUT. This also suggests that its membrane vibrated more at the reduced bias. Even though CMUT and M^3-CMUT have the same top membrane radius, they have different geometry that contributes to the frequency shift. The relative resonant frequency shift was higher in M^3-CMUT, which is due to the spring softening effect. The higher spring softening makes a membrane more flexible, and thus for a given bias condition increases the displacement of the membrane. Also, the change in the real part of the impedance with bias was observed to be greater in the M^3-CMUT, which suggests a higher membrane deflection. Apart from the device impedance, the added parasitic elements resulting from the wiring of the device and the measuring equipment may very well affect this overall measured impedance of the transducers.

By analyzing these fundamental impedance properties of the single-cell devices, it was demonstrated that the membrane displacement was higher in the M^3-CMUT design. This means that the transducer's effective gap height was found to be less than that of the conventional CMUT. The reduction in the cavity of M^3-CMUT enhanced the sensitivity of the transducer, which results in better electrical performances.

The data from the 1-D and 2-D arrays was found to be similar to that of the single-cell device. In these array structures, like their single-cell counterparts, the collapse voltage and the resonant frequency were measured to be lower, whereas the resonant frequency shift was observed to be higher in M^3-CMUT. Thus for these arrays, M^3-CMUT was found to be more sensitive than the CMUT. However, there was a difference in terms of the change in the impedance of the transducers in the arrays. It was found that the measured real part impedance of the CMUT array was larger than that of the M^3-CMUT. This suggests the opposite as what was observed for the single-cell devices. The greater presence of parasitic impedance elements in the arrays might be a contributing factor to this discrepancy.

The novel M^3-CMUT, as both the acoustic transmitter and the receiver, was investigated using its 2-D arrays of the single devices. It was found that the multiple moving membrane transducers (M^3-CMUT) were capable of producing sufficient signals for both transmission and reception. The acoustic transmit and receive properties, i.e., attenuation coefficient, sound velocity, etc. from the pitch-catch experiment were found to be in good agreement with the theoretical values. However, the acoustic power was observed to be lower in M^3-CMUT compared to CMUT. This is due to the trade-off between the sensitivity and the output power of these similarly sized transducers. From the impedance measurement, it was found that the M^3-CMUT arrays have a lower

impedance value than that of the CMUTs, which might very well affect the acoustic power generated from these transducers.

8.2 Future Work

Though the experimental results of the single-cell device are conclusive enough to say that the M^3-CMUT transducer has demonstrated better electrical properties than the conventional CMUT, its array device needs to be investigated further. The acoustic power of a transducer is mostly dependent upon the number of elements in the device. Larger arrays are required for a better-quality power generation in the ultrasound applications. Hence, the improvement in the output power of M^3-CMUT arrays would be a great project to work on in the future.

The presence of release holes (to form the gaps between the membranes and the electrode) on the M^3-CMUT membrane has made the fabricated devices possible to characterize only in the air. However, in many applications, such as ultrasound imaging, the transducer is operated in contact with tissue or in immersion. Therefore, the experiments are required to be done in immersion as well. By covering the release holes while keeping the cavity height intact, the M^3-CMUT devices can be tested in the immersion medium. Thus the immersion-type M^3-CMUT is another significant direction of future work.

References

[1] F. A. Firestone, “Flaw detecting device and measuring instrument,” U.S. Patent 2280226A, 1942.

[2] D. M. Mills, “Medical imaging with capacitive micromachined ultrasound transducer (cMUT) arrays,” in *Proceedings - IEEE Ultrasonics Symposium*, 2004.

[3] I. J. Oppenheim, A. Jain, and D. W. Greve, “MEMS ultrasonic transducers for the testing of solids,” *IEEE Trans. Ultrason. Ferroelectr. Freq. Control*, 2003.

[4] J. Curie and P. Curie, “Développement par compression de l’électricité polaire dans les cristaux hémièdres à faces inclinées,” *Bull. la Société minéralogique Fr.*, vol. 3–4, pp. 90–93, 1880.

[5] W. G. Nelson, Ed., “Piezoelectric Ceramics Materials: Processing, Properties, Characterization, and Applications,” in *Piezoelectric Materials : Structure, Properties, and Applications*, New York, NY: Nova Science Publishers, Inc., 2010, pp. 1–36.

[6] H. Jaffe and D. A. Berlincourt, “Piezoelectric Transducer Materials,” *Proc. IEEE*, 1965.

[7] P. Muralt *et al.*, “Piezoelectric micromachined ultrasonic transducers based on PZT thin films,” *IEEE Trans. Ultrason. Ferroelectr. Freq. Control*, 2005.

[8] M. I. Haller and B. T. Khuri-Yakub, “A surface micromachined electrostatic ultrasonic air transducer,” *IEEE Ultrason. Symp.*, pp. 1241–1244, 1994.

[9] I. Ladabaum, X. Jin, H. T. Soh, A. Atalar, and B. T. Khuri-Yakub, “Surface micromachined capacitive ultrasonic transducers,” *IEEE Trans. Ultrason. Ferroelectr. Freq. Control*, vol. 45, no. 3, pp. 678–690, 1998.

[10] “UT Material Properties Tables.” [Online]. Available: https://www.nde-ed.org/GeneralResources/MaterialProperties/UT/ut_matlprop_liquids.htm. [Accessed: 12-Mar-2019].

[11] W. Kuhl, G. R. Schodder, and F. K. Schodder, “Condenser transmitters and microphones with solid dielectric for airborne ultrasonics,” *Acoustica*, vol. 4, pp. 520–532, 1954.

[12] J. H. Cantrell, J. S. Heyman, W. T. Yost, M. A. Torbett, and M. A. Breazeale, “Broadband electrostatic acoustic transducer for ultrasonic measurements in

liquids," *Rev. Sci. Instrum.*, 1979.

[13] K. Suzuki, K. Higuchi, and H. Tanigawa, "A Silicon Electrostatic Ultrasonic Transducer," *IEEE Trans. Ultrason. Ferroelectr. Freq. Control*, 1989.

[14] D. Hohm and G. Hess, "A subminiature condenser microphone with silicon nitride membrane and silicon back plate," *Cit. J. Acoust. Soc. Am.*, vol. 85, p. 476, 1989.

[15] K. Lindstrom, M. Torndahl, M. Almqvist, H. W. Persson, and L. Wallman, "Characterisation and comparison of a cMUT versus a piezoelectric transducer for air applications," vol. 00, no. c, pp. 1023–1026, 2003.

[16] Ö. Oralkan *et al.*, "Capacitive micromachined ultrasonic transducers: Next-generation arrays for acoustic imaging?," *IEEE Trans. Ultrason. Ferroelectr. Freq. Control*, 2002.

[17] A. Caronti *et al.*, "Capacitive micromachined ultrasonic transducer (CMUT) arrays for medical imaging," *Microelectronics J.*, 2006.

[18] A. Sanh Ergun, B. Temelkuran, E. Ozbay, and A. Atalar, "A new detection method for capacitive micromachine ultrasonic transducers," *IEEE Trans. Ultrason. Ferroelectr. Freq. Control*, 2001.

[19] P. Zhang, G. Fitzpatrick, W. Moussa, and R. J. Zemp, "CMUTs with improved electrical safety & minimal dielectric surface charging," in *Proceedings - IEEE Ultrasonics Symposium*, 2010.

[20] C. H. Cheng, C. Chao, X. Shi, and W. W. F. Leung, "A flexible capacitive micromachined ultrasonic transducer (CMUT) array with increased effective capacitance from concave bottom electrodes for ultrasonic imaging applications," in *Proceedings - IEEE Ultrasonics Symposium*, 2009.

[21] T. A. Emadi and D. A. Buchanan, "Capacitive micromachined ultrasonic transducer with multiple deflectable membranes," U.S. Patent 9925561B2, 2018.

[22] H. Azhari, "Waves-A General Description," in *Basics of Biomedical Ultrasound for Engineers*, 2010, pp. 9–33.

[23] H. Azhari, "Reflection and Transmission," in *Basics of Biomedical Ultrasound for Engineers*, John Wiley & Sons, Inc., 2010, pp. 107–131.

[24] H. Azhari, "Attenuation and Dispersion," in *Basics of Biomedical Ultrasound for Engineers*, John Wiley & Sons, Inc., 2010, pp. 93–105.

[25] J. David and N. Cheeke, “Fundamentals and applications of ultrasonic waves,” CRC Press, 2002, pp. 55, 103.

[26] T. Hsu, “Microactuation,” in *MEMS and microsystems : design, manufacture, and nanoscale engineering*, Second Ed., John Wiley & Sons, Inc., 2008, pp. 53–58.

[27] H. Azhari, “Transducers and Acoustic fields,” in *Basics of Biomedical Ultrasound for Engineers*, John Wiley & Sons, Inc., 2010, pp. 153–190.

[28] T. A. Emadi and D. A. Buchanan, “Design and fabrication of a novel MEMS capacitive transducer with multiple moving membrane, M3-CMUT,” *IEEE Trans. Electron Devices*, vol. 61, no. 3, pp. 890–896, 2014.

[29] J. M. Cannata, T. A. Ritter, W. H. Chen, R. H. Silverman, and K. K. Shung, “Design of efficient, broadband single-element (20-80 MHz) ultrasonic transducers for medical imaging applications,” *IEEE Trans. Ultrason. Ferroelectr. Freq. Control*, 2003.

[30] L. Medina, E. Moreno, G. González, and L. Leija, “Circular ultrasonic transducer characterization: theoretical and experimental results,” 2003.

[31] D. D. Zakharov and L. J. Fradkin, “Asymptotic evaluation of the pulse train radiated by an angled beam and fluid coupled rectangular ultrasonic transducer.,” *J. Acoust. Soc. Am.*, 2010.

[32] C. Blignault, D. G. Hattingh, G. H. Kruger, T. I. van Niekerk, and M. N. James, “Friction stir weld process evaluation by multi-axial transducer,” *Meas. J. Int. Meas. Confed.*, 2008.

[33] S. Zhang, Z. Z. Li, and E. Z. Fang, “Research on the parametric array sound characteristic of the annular transducer,” in *Proceedings of the 2015 Symposium on Piezoelectricity, Acoustic Waves and Device Applications, SPAWDA 2015*, 2015.

[34] X. Qu *et al.*, “Synthetic aperture ultrasound imaging with a ring transducer array: preliminary ex vivo results,” *J. Med. Ultrason.*, 2016.

[35] S. Na, “Air-coupled Capacitive Micromachined Ultrasonic Transducers based on Annular Cell Geometry,” 2017.

[36] T. Hsu, “Static Bending of Thin Plates,” in *MEMS and microsystems : design, manufacture, and nanoscale engineering*, Second Ed., John Wiley & Sons, Inc., 2008, pp. 110–118.

[37] D. T. Yeh, Ö. Oralkan, I. O. Wygant, M. O'Donnell, and B. T. Khuri-Yakub, "3-D Ultrasound imaging using a forward-looking CMUT ring array for intravascular/intracardiac applications," *IEEE Trans. Ultrason. Ferroelectr. Freq. Control*, 2006.

[38] J. M. Thijssen and M. Mischi, "Ultrasound Imaging Arrays," in *Comprehensive Biomedical Physics*, 2014.

[39] Y. Zeng, D. Xing, Y. Wang, B. Yin, and Q. Chen, "Photoacoustic and ultrasonic coimage with a linear transducer array," *Opt. Lett.*, 2004.

[40] O. T. Von Ramm and F. L. Thurstone, "Cardiac Imaging Using a Phased Array Ultrasound System I. System Design," 1976.

[41] J. A. Hides, C. A. Richardson, and G. A. Jull, "Use of real-time ultrasound imaging for feedback in rehabilitation," *Man. Ther.*, 1998.

[42] O. Martinez-Graullera, D. Romero-Laorden, A. Ibañez, and L. G. Ullate, "A new beamformer based on phase dispersion to improve 2D sparse array response," in *Proceedings of the IEEE Sensor Array and Multichannel Signal Processing Workshop*, 2012.

[43] J. Woo and Y. Roh, "Ultrasonic 2D matrix array transducer for volumetric imaging in real time," in *IEEE International Ultrasonics Symposium, IUS*, 2012.

[44] L. L. P. Wong, A. I. H. Chen, Z. Li, A. S. Logan, and J. T. W. Yeow, "A row-column addressed micromachined ultrasonic transducer array for surface scanning applications," *Ultrasonics*, 2014.

[45] X. Jin, I. Ladabaum, F. Levent Degertekin, S. Calmes, and B. T. Khuri-Yakub, "Fabrication and characterization of surface micromachined capacitive ultrasonic immersion transducers," *J. Microelectromechanical Syst.*, 1999.

[46] Y. Huang, A. S. Ergun, E. Haeggström, M. H. Badi, and B. T. Khuri-Yakub, "Fabricating Capacitive Micromachined Ultrasonic Transducers With Wafer-Bonding Technology," *J. MICROELECTROMECHANICAL Syst.*, vol. 12, no. 2, 2003.

[47] S. M. Kim and D. Y. Khang, "Bulk micromachining of Si by metal-assisted chemical etching," *Small*, 2014.

[48] G. Vanko *et al.*, "Bulk micromachining of SiC substrate for MEMS sensor applications," 2013.

[49] T. Hsu, “Overview of Micromanufacturing,” in *MEMS and microsystems : design, manufacture, and nanoscale engineering*, Second Ed., John Wiley & Sons, Inc., 2008, pp. 323–347.

[50] N. Tas, T. Sonnenberg, H. Jansen, R. Legtenberg, and M. Elwenspoek, “Stiction in surface micromachining,” *J. Micromechanics Microengineering*, 1996.

[51] A. E. H. Love, “On the Small Free Vibrations and Deformations of Thin Elastic Shells,” *Phil. Trans. Roy. Soc.*, 1888.

[52] M.-H. Bao, “Electrostatic driving and capacitive sensing,” *Micro Mech. Transducers Press. Sensors, Accelerometers Gyroscopes*, no. c, pp. 139–198, 2000.

[53] R. Hooke, *De Potentia Restitutiva, or of Spring. Explaining the Power of Springing Bodies*. London, 1678.

[54] F. V. Hunt, *Electroacoustics: The analysis of transduction, and its historical background*, 2nd ed. Cambridge, Massachusetts: Harvard University Press, 1982.

[55] S. Timoshenko and S. Woinowsky-Krieger, *Theory of plates and shells*, 2nd ed. Macgraw-Hill Book Company, 1959.

[56] W. Soedel and M. S. Qatu, “Vibrations of Shells and Plates, Third Edition,” *J. Acoust. Soc. Am.*, 2005.

[57] “COMSOL Multiphysics® Modeling Software.” [Online]. Available: https://www.comsol.com/. [Accessed: 01-Nov-2018].

[58] T. A. Emadi and D. A. Buchanan, “Multiple Moving Membrane CMUT With Enlarged Membrane Displacement and Low Pull-Down Voltage,” *IEEE Electron Device Lett.*, vol. 34, no. 12, pp. 1578–1580, 2013.

[59] “CAD: softMEMS MEMS Pro.” [Online]. Available: https://www.cmc.ca/en/WhatWeOffer/Products/CMC-00025-77933.aspx. [Accessed: 11-Dec-2018].

[60] A. Cowen, B. Hardy, R. Mahadevan, and S. Wilcenski, “PolyMUMPs Design Handbook a MUMPs® process,” 1992.

[61] Keysight Technologies, “Impedance Measurement Handbook, A guide to measurement technology and techniques, 6th Edition - Application Note.”

[62] L. Technology Corporation, “LT1229/LT1230 - Dual and Quad 100MHz Current

Feedback Amplifiers."

[63] "Viscosity of Air, Dynamic and Kinematic | Engineers Edge | www.engineersedge.com." [Online]. Available: https://www.engineersedge.com/physics/viscosity_of_air_dynamic_and_kinematic_14483.htm. [Accessed: 12-Feb-2019].

[64] "Calculation of absorption of sound by the atmosphere." [Online]. Available: http://resource.npl.co.uk/acoustics/techguides/absorption/. [Accessed: 12-Feb-2019].

[65] D. A. Bohn, "Environmental Effects on the Speed of Sound," *J. Audio Eng. Soc.*, vol. 36, no. 4, 1988.